Over-bounding Integrated INS/GNSS Output Errors

A DISSERTATION
SUBMITTED TO THE FACULTY OF THE GRADUATE SCHOOL
OF THE UNIVERSITY OF MINNESOTA
BY

Zhiqiang Xing

IN PARTIAL FULFILLMENT OF THE REQUIREMENTS
FOR THE DEGREE OF
DOCTOR OF PHILOSOPHY

Advisor: Demoz Gebre-Egziabher

October 2010

Acknowledgements

It is a pleasure to thank those who made this dissertation possible. I owe my deepest gratitude to my adviser, Professor Demoz Gebre-Egziabher, for his guidance, patience, and constant support during my research and study at the University of Minnesota. His inspiring enthusiasm on navigation systems and estimation theory has motivated me throughout my dissertation writing.

I am heartily thankful to Professor Yiyuan Zhao, who shared with me valuable insights on optimal control and stochastic process. I always enjoy having discussions with him. My sincere thanks also go to Professor William Garrard and Professor Rajesh Rajamani, for their insightful comments as members of my doctoral committee.

Many friends and colleagues have helped me through intelligent discussions on navigation, control, computation and mathematics – Ying Qi, Iris Hong Yang, Yunfeng Shao, Guijin Zheng, Jie Chen, Wei Liu, Jiaqi Yang, Zhefeng Li and Jason Zhu. I greatly value their friendship and encouragement.

Most importantly, none of this would have been possible without the love and patience of my family. My parents, Lin Xing and Xiuying Wu, to whom this dissertation is dedicated to, have been a constant source of love, concern, support and strength all these years.

Abstract

This thesis examines issues associated with the integrity risk over-bounding in INS/GNSS integration. The integrity risk over-bounding requires three issues to be considered: Modeling and over-bounding of inertial sensor output errors; modeling and over-bounding of GNSS signal errors; and the over-bounding of the output of nonlinear transformations of random variables. While considerable amaount of work has been done in modeling and over-bounding GNSS errors, this thesis explored the other two relatively new issues. This thesis develops a methodology for doing this whereby the varying and higher order process in the actual navigation solution are over-bounded using a lower-order, stationary time-domain model that is a conservative approximation of the actual noise process. This requires developing and validating unified mathematical models for over-bounding the behavior of the post calibration residual errors of inertial sensors. The mathematical models of the INS are a set of nonlinear stochastic differential equations. The nonlinearities of the system come from two parts which need to be handled in the over-bounding: the nonlinear transformation of the sensor errors, and the nonlinear transformation of the previous navigation states. A methodology for analyzing and over-bounding nonlinear transformations of random variables which occur in INS systems is developed. It is shown that the INS system output errors can be over-bounded by Gaussian distributions with an inflated variance. How this approach can be used to over-bound errors in simple vehicle navigation and guidance applications is shown by examples.

Contents

List of Tables

List of Figures

Chapter 1

Introduction

1.1 Integrated Navigation Systems

A navigation system is a device that determines a vehicle, a person, or an object's position and velocity relative to a known reference [3, 4]. Sometimes it also provides attitude. The output of the navigation system is called the navigation solution and can be used by other systems, such as a vehicle control system or a guidance system. There are two fundamental methods for navigation: position fixing and dead reckoning. Position fixes may be obtained by measuring the ranges, bearings (angles) or a combination of both to objects whose positions are known. Ranging and bearing measurements can be made using radio signals, lasers, acoustic signals or a combination of all of the above. In addition magnetic compasses can be used to determine bearing. In dead reckoning, position is deduced from a series of velocity, heading, acceleration and/or rotation measurements relative to an initial position. To determine the current position a user must know the history of past positions and velocities. Depending on the application velocity may come from an odometer, air speed sensor, Doppler radar, sonar or integrating accelerometer measurements. Rotation measurements may come from magnetometers or from integrating angular rate measurements made by gyroscopes.

Integrated navigation systems blend the information from various sensors or systems (position fixing or dead reckoning) in real time to generate an optimal estimate of a vehicle's navigation state vector. Integrated navigation systems are used widely because it is rare when a single navigation sensor or system can provide a robust and ubiquitous navigation solution. Thus, in integrated navi-

gation systems, the blending allows leveraging the strengths of the various systems and mitigating their weakness.

Since the component sensors and systems have errors and noises, the output of the integrated navigation systems will have errors as well. While a lot of work have been done in the design and analysis of the integrated navigation systems, there has been little work examining the integrity risk over-bounding in the integrated navigation systems, especially the integrated INS/GNSS systems. This over-bounding is the focus of this thesis.

1.2 Integrated INS/GNSS Systems

An integration that has and continues to be used widely is that of the Global Navigation Satellite Systems (GNSS) and Inertial Navigation Systems (INS). An inertial navigation system is a self-contained dead-reckoning navigator equipped with sensors that continuously measure acceleration and rotation, from which velocity and position vectors are computed. Rotation is required because the frame relative to which we want to know position is not always the same frame in which the sensing of acceleration occurs. The sensors used are collectively called inertial sensors and normally consist of three mutually orthogonal accelerometers and three gyros aligned with the accelerometers. The inertial navigation system integrates the inertial sensor output to provide the position, velocity and attitude.

Based on the difference in quality, inertial sensors can be categorized into 'consumer' ('automotive') grade, 'tactical' grade and 'navigation' grade. In this thesis, the term low-cost inertial sensors refers to inexpensive solid-state rate gyros and accelorometers in a class that is normally referred to as 'automotive' or 'consumer' grade. These are being increasingly used in real-time vehicle navigation and guidance systems. A more precise definition of these monikers is provided in chapter 3. Global Navigation Satellite Systems (GNSS) are satellite-based position-fixing navigation systems [3]. A GNSS receiver may derive a three-dimensional position fix and its clock offset from range measurements to at least four satellites. GNSS and INS have complementary characteristics. GNSS have bounded errors and a high long-term position and velocity accuracy, while INS have unbounded errors and a short-term accuracy. GNSS have a low data rate ($\leq$10 Hz) while INS have a high data rate ($\geq$50 Hz). GNSS does not provide an attitude solution unless multiple antennas are used, while INS provide attitude, angular rate and acceleration measurements, as

well as position and velocity. GNSS are susceptible to external jamming and interference. INS are self-contained and, thus, not susceptible to jamming and interference. GNSS, for example, cannot provide a continuous signal in an environment where blockage of the signal is likely. This includes urban canyons, indoors, and in jamming and interference environments. On the other hand, in these environments, INS can provide a continuous navigation solution. INS/GNSS integration takes advantage of both GNSS and INS strengths to overcome their respective drawbacks. For the INS/GNSS application, an integration algorithm that has been used extensively is the Extended Kalman Filter (EKF) [5, 6].

1.3 Integrity and Over-bounding

One of the metrics used to assess the performance of integrated navigation systems is called integrity risk. Integrity risk (or simply integrity for short) is the likelihood of an undetected navigation error or failure that results in hazardously misleading information (HMI). Integrity information is very important for safety critical applications such as civil aviation [7–12] as well as liability critical applications such as electronic toll collection system [13]. In practice, users define a confidence bound for the navigation solution which bracket all but the rarest navigation output errors with a confidence of 1-α where α is usually a very small number, such as 10^{-7}. There is a possibility that the navigation system position errors can exceed the confidence bound but the user is unaware of that. This is a case of loss of integrity, and the integrity risk is α. It is also called the probability of hazardously misleading information (HMI).

It is clear that the operational test for integrity relies on conservatism in the user confidence bounds. The navigation system should guarantee a user error bound equal to or larger than the actual value to protect the integrity risk requirement. Because the actual error distributions can be complex or time varying, it is common to replace actual error distributions with conservative approximations called overbounds [10]. In what follows we describe some INS/GNSS applications which require a high level of integrity but may use low-cost sensor such as the ones we focus on in this thesis.

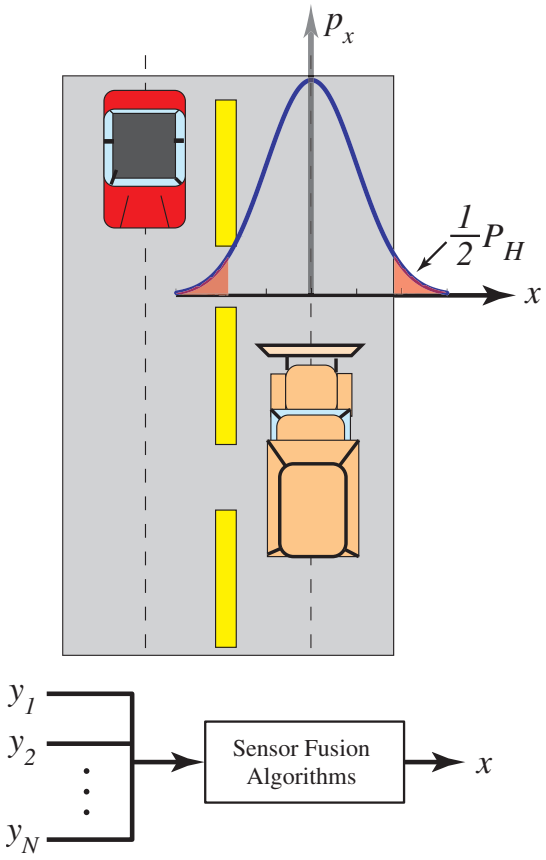

Figure 1.1: An Unmanned Ground Vehicle (Left) In Operation.

1.3.1 Automotive Applications

Consider the automotive guidance and control problem discussed in [14–16] and depicted in Figure 1.1. The snow plow is equipped with a low-cost INS/GNSS system for navigation and guidance in low visibility conditions. The vehicle operates in a lane of width d and the state variable x is its deviation from the centerline of the lane. As shown in the block diagram in Figure 1.1, x is estimated in real time by fusing the outputs y_i (where $i = 1, 2, \ldots, N$) of many sensors including inertial sensors and GNSS receivers. Since this is a problem where INS/GNSS navigation errors have safety-of-life implications, we are interested in bounding these risks. For example, we may want to quantify the risk that an undetected sensor error will cause a hazardous condition, such as the case where the snowplow is in the wrong lane but the sensor fusion algorithms generate an estimate of x indicating otherwise. The probability of such an occurrence is denoted P_H (subscript

"H" for "Hazard") and is equal to:

$$\begin{aligned} P_H &= P\{x > d \cup x < -d\} \\ &= \int_{-\infty}^{-d} p_x dx + \int_{d}^{+\infty} p_x dx. \end{aligned} \tag{1.1}$$

This risk is equal to the shaded area under the probability density function for x shown in Figure 1.1. Precisely or conservatively quantifying P_H requires error models for the sensors used in the navigation system which can be used to overbound the navigation system output errors.

1.3.2 UAV Application

Unmanned Aerial Vehicles (UAVs) are envisioned for use in a broad range of applications such as ground, air and sea surveillance, target acquisition, and target designation. Due to cost and payload constraints, most small UAVs are equipped with a low-cost INS/GNSS system for navigation purposes. Several individual UAVs are undergoing review for experimental certification by the FAA. Safety is a fundamental requirement for UAVs' operation in the National Airspace System (NAS), and is a key concern in evaluating potential NAS operations [17]. In some situations, (for example, urban traffic monitoring), we have a high integrity requirement for position and/or velocity to avoid hazardous situation which can arise by collision when flying close to buildings and other structures.

1.4 Prior Work in Integrity

1.4.1 SBAS and GBAS Over-bounding

Integrity is a critical requirement used in the certification of commercial navigation systems. In those applications, we are interested in ensuring that the occurrence of rare events (e.q. accidents) with unacceptably high consequences are minimized. In mathematical terms this implies that we accurately characterize the tails of output error distributions or want to conservatively and tightly overbound the true distribution. A significant amount of work has been done in this area mostly related to the Ground Based Augmentation System (GBAS) or the Satellite Based Augmentation System (SBAS). The idea is to bound the output errors in some sense in the range domain (sensor output domain), and to guarantee the overbound in the user or position domain. Currently the certification of GPS augmentation systems relies on Cumulative Distribution Function (CDF) over-bounding,

which is proposed in [7]. It has been shown in [7] that the linear combination of independent random variables with zero-mean, symmetric and uni-modal distributions can be over-bounded if an individual input random variable is over-bounded. The constraints of being zero-mean, symmetric and uni-modal can be relaxed to be arbitrary distributions in Paired-CDF over-bounding [8] and excess-mass over-bounding [9]. The Paired-CDF over-bounding construct a CDF to bound both sides of the range-domain error distribution, while the excess-mass over-bounding construct a pdf the integration of which may be greater than 1. One over-bounding example application in SBAS integrity validation is given in [12].

Previously mentioned over-bounding methods apply to linear combinations (sums) of independent random variables. This situation occurs in the GPS positioning problem where estimating position can be viewed as a weighted sum of the GPS range measurements. In practice, however, the input (differential GPS corrections etc.) may be correlated. In this instance the inputs are random signals rather than independent random variable sequences. Further, the processing applied to those input signals is by an estimator (Extended Kalman Filter, Unscented Kalman Filter, etc.) is more than a simple linear combinations (or sum). Symmetric over-bounding is proposed in [10] as a method for over-bounding outputs of linear systems with time correlated inputs as long as those inputs have a probability distribution which a linear mapping can make spherically symmetric. An example application of symmetric over-bounding to differential GPS corrections in GBAS or SBAS is given in [10].

1.4.2 Integrated Navigation System Over-bounding

While a considerable amount of over-bounding work has been done in GNSS augmentation system applications, integrated INS/GNSS over-bounding is still a open area. In an integrated INS/GNSS navigation system, as will be shown later in this thesis, the input inertial sensor measurements have a correlated structure which may result from high-order and time-varying processes, and the estimator through which the sensor measurements are processed can be nonlinear in nature. There are no existing solutions to the over-bounding of the output of an INS (Integrated Navigation System).

1.5 Thesis Contributions

Integrated INS/GNSS system overbounding is a much more complex problem than over-bounding linear combination of independent random inputs. The inertial sensor errors which exhibit a higher-order correlation and may be non-stationary have to be replaced by a lower-order, stationary model that is conservative and easy to use for over-bounding purposes. The INS system mechanization equations are nonlinear and the estimators used for INS/GNSS fusion are nonlinear. This means that they have a structure much more complex than simple linear combinations or linear filters. Since there is no general solution to a general nonlinear over-bounding problem, the structure of the nonlinear estimators need to be investigated for the specific INS/GNSS system and the nonlinearity inside the estimator needs to be addressed specifically. The original contributions of the work in this thesis are related to this problem and are described next.

1.5.1 IMU Error Models

This thesis develops and validates unified mathematical models for the behavior of the post calibration residual errors of a class of low cost inertial sensors. The model developed is unified in that it is a single model which can be used to capture or bound the behavior of various output errors normally seen in this class of inertial sensors. This thesis also shows how these models can be tuned to bound the output errors of inertial navigation systems that use these sensors. These error models are amenable for use in risk or integrity analysis of vehicle navigation and guidance systems. Unlike previous error modeling procedures using the Allan variance method, the procedure in this thesis focuses on *over-bounding* the sensor output errors using a simple time-domain model rather than measuring the quality of those sensors using frequency-domain models [18].

1.5.2 Over-bounding INS/GNSS Output Errors

This thesis presents a method for over-bounding the nonlinear transformations of random variables which occur in INS systems. It is shown that the INS system output errors can be over-bounded by Gaussian distributions by inflating the variance from the ones predicted by covariance propagation. This is an extension of previous over-bounding methods which apply only to linear systems.

1.6 Thesis Organization

Accordingly, the remainder of this thesis is organized as follows: In Chapter 2, an overview of over-bounding is given. In Chapter 3, a methodology for constructing a unified time-domain error model of inertial sensor errors is proposed. The use of this model for over-bounding the output errors in navigation systems is shown. In Chapter 4, the over-bounding of nonlinear INS system output errors is investigated. It is shown the process noise in INS equations can be over-bounded by Gaussian distributions. This is followed by a proof that the coordinate transformation of random variables (one source of non-linearity in INS/GNSS integration) can be over-bounded by a Gaussian distribution. In Chapter 5, the applications of previous chapter results are shown using two examples. Conclusions and suggestions for future research are presented in Chapter 6.

Chapter 2

An Overview of Over-bounding

2.1 Introduction

This chapter provides an overview of the concept of over-bounding and algorithms that are currently used to compute over-bounds. We start by providing a mathematical description of the over-bounding problem. Then we will describe three approaches that have been used in over-bounding problems. The first approach is what we will call *independent distribution over-bounding* and it is based on Decleene's seminal work on this subject [7]. The second approach is what is known as *paired over-bounding* and it relaxes some of the restrictions associated with independent distribution over-bounding [8, 9, 19]. The third approach is what is known as *symmetric overbounding* and allows extending independent distribution and paired over-bounding techniques to problems where input errors are correlated [10]. These ideas will be used later in Chapter 4 when the ideas behind INS overbounding are discussed.

2.2 Definition of Over-bounding

To better understand over-bounding consider the example of the ground vehicle operation depicted in Figure 1.1. This is an application discussed in [14, 16] which is that of a navigation system for a snow plow in low-visibility conditions. The vehicle operates in a lane of width d and the state variable x_j is its deviation from the centerline of the lane (x_j is the j^{th} component of $\mathbf{x} \in \mathbb{R}^{n\times 1}$). As shown in the block diagram in Figure 1.1, x_j is estimated in real time by fusing the outputs y_i

(where $i = 1, 2, \ldots, N$) of many sensors.

Generalizing the situation depicted in Figure 1.1, the relationship between the navigation state, $\mathbf{x}$, and the *error-free* sensor measurements, $\mathbf{y} \in \mathbb{R}^{m\times 1}$ can be written as follows:

$$\mathbf{y} = \mathbf{H}\mathbf{x}, \tag{2.1}$$

where $\mathbf{H} \in \mathbb{R}^{m\times n}$ is the measurement or observation matrix. Sensor outputs are always corrupted by noise and we will let $\mathbf{v}$ denote the vector of errors corrupting the measurements. Thus, in practice the model we deal with is given by:

$$\begin{aligned} \tilde{\mathbf{y}} &= \mathbf{y} + \mathbf{v} \\ &= \mathbf{H}\mathbf{x} + \mathbf{v}, \end{aligned} \tag{2.2}$$

where $\tilde{\mathbf{y}}$ is the observed sensor output. The quality of the estimate for x_j is characterized by the marginal probability density function (pdf), p_{x_j}, computed from the following:

$$p_{x_j} = \int_{-\infty}^{+\infty}\int_{-\infty}^{+\infty}\int_{-\infty}^{+\infty}\cdots\int_{-\infty}^{+\infty} p_{x_j|\mathbf{y}}\, p_{\mathbf{y}}\, dy_1\, dy_2\, dy_3 \cdots dy_N, \tag{2.3}$$

where $p_{\mathbf{y}}$ is the joint PDF of the measurements. Note that for ease of notation and because there is no ambiguity, we denote this PDF as $p_{\mathbf{y}}$ and not $p_{\tilde{\mathbf{y}}}$. This PDF is a function of $p_{\mathbf{v}}$–the sensor noise PDF. The marginal pdf of x_j conditioned on $\mathbf{y}$ is given by PDF $p_{x_j|\mathbf{y}}$ and is a function of the $\mathbf{H}$ or in the more general sense the sensor fusion algorithms.

Now suppose the risk that an undetected sensor error will cause a hazardous condition is P_R. For example, P_R might be the probability that the snow plow is in the wrong lane while the sensor fusion algorithms generate an estimate of x_j indicating otherwise. For the case shown in Figure 1.1, P_R would be equal to the shaded area under p_{x_j}. That is:

$$P_R = P\{x_j \leq -d \cup x_j \geq +d\}. \tag{2.4}$$

This operation is considered safe if it can be shown that P_R is less than some pre-defined threshold value of acceptable risk. In navigation applications this threshold is called the *integrity risk* and is denoted by I_H. Since the two events ($x_j \leq -d$ and $x_j \geq +d$) are mutually exclusive, determining whether a given operation has acceptable integrity reduces to showing that:

$$\phi_{x_j}(-d) + (1 - \phi_{x_j}(+d)) \leq I_H, \tag{2.5}$$

where $\phi_{x_j}(\eta)$ is the Cumulative Distribution Function (CDF) of x_j defined as:

$$\phi_{x_j}(\eta) = \int_{-\infty}^{\eta} p_{x_j}(\xi)\, d\xi. \tag{2.6}$$

In actual applications precisely quantifying P_H is difficult because our knowledge of $p_{\mathbf{v}}$ (or alternately $p_{\tilde{\mathbf{y}}}$) is never perfect. Our uncertainty in $p_{\mathbf{v}}$ may take on the following forms:

1. One or more of the marginal distributions p_{v_i} may have an unknown but non-zero mean. This can be the result of, for example, a failed sensor whose failure has not yet been identified by fault detection and isolation algorithms.

2. The tails of the marginal distribution p_{v_i} may be poorly modeled because of insufficient data.

The uncertainty in the first item above can be thought of as a case where some of the marginal distributions p_{v_i} may be non-stationary. Thus, the problem of over-bounding is to determine how to capture or bound these uncertainties in $p_{\mathbf{v}}$ while ensuring that our requirement that $P \leq I_H$ at all times. This requires that we know how the uncertainties in $p_{\mathbf{v}}$ map into uncertainties of $p_{\mathbf{x}}$ or p_{x_j}.

2.3 Independent Distribution Over-bounding

The basic notion of most over-bounding techniques is to define an approximation that conservatively represents the PDF for the output of an operation on one or more inputs (or measurements) that are random variables. In the case where the operation is linear, we can write the linear estimator for $\mathbf{x}$ as a function of measurements $\tilde{\mathbf{y}}$ in the following manner:

$$\hat{\mathbf{x}} = \mathbf{G}\tilde{\mathbf{y}} \tag{2.7}$$

where $\mathbf{G} \in \mathbb{R}^{n \times m}$ and $\hat{\mathbf{x}}$ is the estimate of $\mathbf{x}$. That is, the relationship between the j^{th} component of $\hat{\mathbf{x}}$ and $\tilde{\mathbf{y}}$ is given by:

$$\hat{x}_j = g_{j1}y_1 + g_{j2}y_2 + \cdots + g_{jm}y_m, \tag{2.8}$$

where g_{ji} is the element in the j^{th} row and i^{th} column of $\mathbf{G}$. In this case the PDF for $\hat{x}_j$ denoted p_{x_j} will be given by [20]:

$$p_{x_j} = \frac{1}{\|g_{j1}\|} p_{y_1}\left(\frac{y_1}{g_{j1}}\right) \bullet \frac{1}{\|g_{j2}\|} p_{y_2}\left(\frac{y_2}{g_{j2}}\right) \bullet \cdots \bullet \frac{1}{\|g_{jm}\|} p_{y_m}\left(\frac{y_m}{g_{jm}}\right) \tag{2.9}$$

where $\bullet$ is used to denote the convolution operation defined as:

$$p_1 \bullet p_2 = \int_{-\infty}^{+\infty} p_1(x-\xi)\, p_2(\xi)\, d\xi. \tag{2.10}$$

Our objective is to find an approximation for p_{x_j} that is conservative. The approximation is conservative if its integrated tail probability everywhere exceeds the integrated tail probability of the actual output distribution. This definition can be quantitatively expressed as follows:

$$\begin{aligned} \textstyle\int_{-\infty}^{x} \bar{p}_{x_j}(\xi)\, d\xi \geq \int_{-\infty}^{x} p_{x_j}(\xi)\, d\xi \quad x_j < x_{m_j} \\ \textstyle\int_{x}^{+\infty} \bar{p}_{x_j}(\xi)\, d\xi \geq \int_{x}^{+\infty} p_{x_j}(\xi)\, d\xi \quad x_j > x_{m_j} \end{aligned} \tag{2.11}$$

where the overbar indicates an approximation and x_{m_j} is the median of x_j. These relationships apply to the right and left distribution tails on either side of the distribution median. This is the definition of CDF over-bounding and can alternatively be written as:

$$\begin{aligned} \bar{\phi}_{x_j}(x) \geq \phi_{x_j}(x) \quad x_j < x_{m_j} \\ \bar{\phi}_{x_j}(x) \leq \phi_{x_j}(x) \quad x_j > x_{m_j} \end{aligned} \tag{2.12}$$

The two sets of equations state that $\bar{p}_{x_j}$ over-bounds p_{x_j}. We will use the following short-hand notation to represent over-bounding as defined in Equation 2.11 and Equation 2.12:

$$\bar{p}_{x_j} \succ p_{x_j}. \tag{2.13}$$

The earliest form of CDF over-bounding was introduced in [7]. This form of CDF over-bounding applies only to independent random variables (i.e., each v_i is independent) and, thus, it is sometimes called independent-distribution over-bounding. In [7] it is shown that with the convolution operation defined by Equation 2.9, $\bar{p}_{x_j}$ over-bounds p_{x_j} as long as $\bar{p}_{y_i}$ (or alternatively, $\bar{p}_{v_i}$) over-bounds p_{y_i} (or alternatively p_{v_i}) and the actual distributions and over-bounds are independent, symmetric, unimodel and have zero-means. This requirement is summarized graphically in Figure 2.1. Several extensions and variants of this independent-distribution have been presented to accommodate certain types of uncertainties in p_{v_i} [8]. The symmetry, unimodel, and zero-mean conditions are not generally significant when the input noise is approximately zero-mean Gaussian. However, the requirement that the input random variables be independent places a significant constraint on many applications. To deal with this latter constraint, the work in [10] develops a method known as symmetric over-bounding which is discussed in section 2.5.

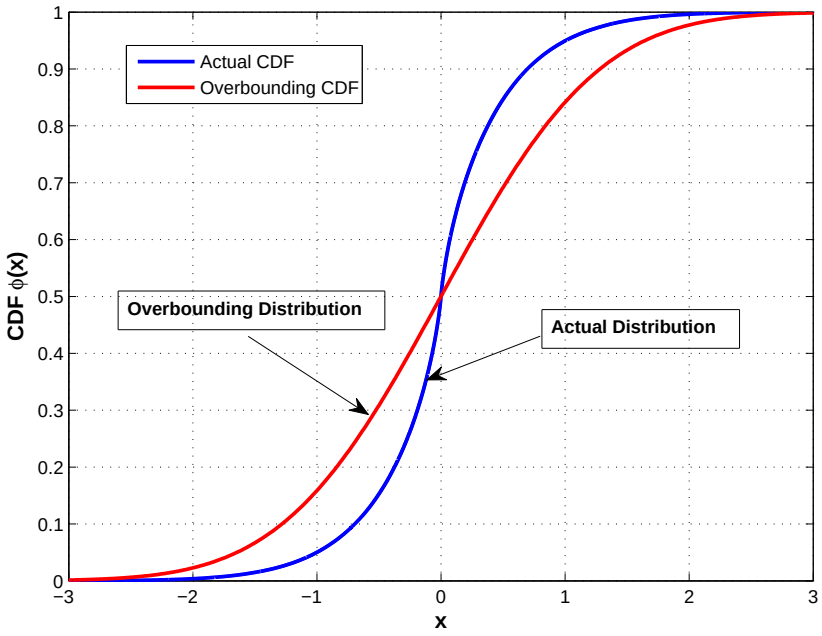

Figure 2.1: CDF Over-bounding Concept.

Even though any distribution satisfying the over-bounding requirements shown in Figure 2.1 can be used, normally in practice Gaussian distribution is used. This is because they make the problem easier to deal with mathematically. Specifically, they simplify the evaluation of Equation 2.9 because each marginal over-bounding distribution (p_{y_i} or p_{v_i}) is defined by only two parameters– a mean and a variance. This, however, is also the drawback of using Gaussian over-bounds–they do not provide enough degrees of freedom to generate ”tight” over-bounds. By tight over-bounds we mean over-bounds that are very close to the underlying distributions we are interested in over-bounding. The best example to illustrate this drawback is to consider heavy-tailed distribution. Bounding this distributions using a Gaussian CDF leads to large conservatism at the core of the distribution. Thus, conservatism (*i.e.* $P \leq I_H$) comes at the price of reported system accuracy.

2.4 Paired Over-bounding

When $p_{\mathbf{v}}$ is a non-zero mean distribution, then independent distribution over-bounding does not work. The approach to over-bounding known as paired over-bounding removes the restriction that

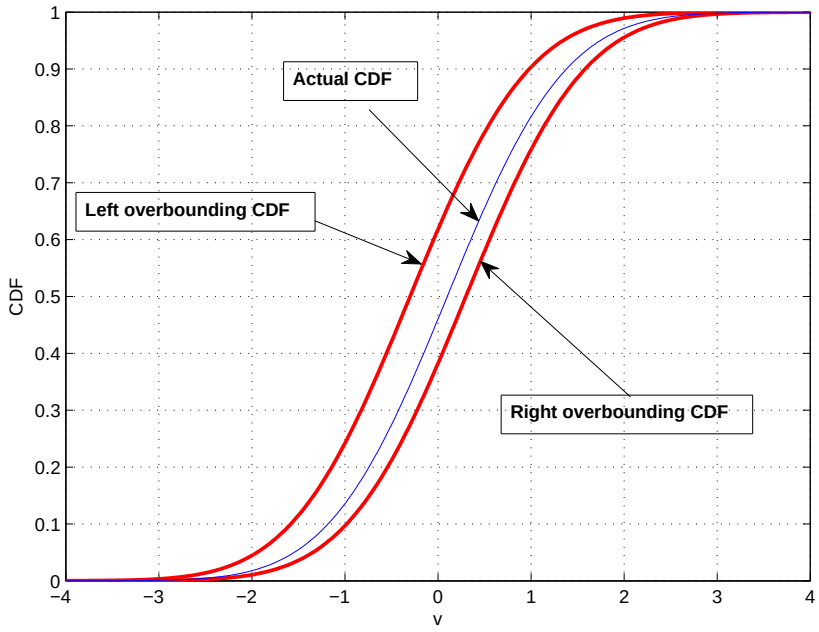

Figure 2.2: Paired CDF Overbounding Concept.

$p_{\mathbf{v}}$ be zero-mean. In simple terms, the paired over-bound approach uses a pair of overbounds for each non-zero mean input v_i. This pair of over-bounds consists of a left bound p_L and a right bound p_R which are defined to over-bound the true PDF for v_i, p_{v_i}, as follows [8]:

$$\begin{aligned} \int_{-\infty}^{v_i} p_L(\xi)\,d\xi &\geq \int_{-\infty}^{v_i} p_{v_i}(\xi)\,d\xi \quad \forall v_i \\ \int_{-\infty}^{v_i} p_R(\xi)\,d\xi &\leq \int_{-\infty}^{v_i} p_{v_i}(\xi)\,d\xi \quad \forall v_i \end{aligned} \tag{2.14}$$

Using the CDF over-bounding definition this can be written as:

$$\begin{aligned} \phi_L(v) &\geq \phi_{v_i}(v) \quad \forall v_i \\ \phi_R(v) &\leq \phi_{v_i}(v) \quad \forall v_i \end{aligned} \tag{2.15}$$

This definition is summarized graphically in Figure 2.2.

It has been proved in [8] that the paired over-bounding properties are preserved through convolution. Suppose we want to find the paired over-bounds for $x = v_1 + v_2$ where v_1 and v_2 are two random variables with true CDFs ϕ_{v_1} and ϕ_{v_2}. If ϕ_{L_1} and ϕ_{R_1} are paired over-bounds for ϕ_{v_1}, and ϕ_{L_2}

and ϕ_{R_2} are paired over-bounds for ϕ_{v_2} according to the definition 2.15, then

$$\begin{aligned} \phi_{L_1+L_2}(z) &\geq \phi_x(z) \quad \forall z \\ \phi_{R_1+R_2}(z) &\leq \phi_x(z) \quad \forall z \end{aligned} \tag{2.16}$$

where $\phi_{L_1+L_2}$ is the convolution of ϕ_{L_1} and ϕ_{L_2} and ϕ_x is the true CDF for $x = v_1 + v_2$.

This result implies that the paired over-bounding of individual random variables is preserved through linear combination, even for those distributions that are not zero-mean, symmetric, and uni-modal. This an extension of independent distribution over-bounding.

2.5 Symmetric Over-bounding

In previous methods to over-bound linear combination of the vector of random inputs, denoted as $x = \mathbf{a}^T\mathbf{v}$, the elements of input random vector $\mathbf{v}$ have to be independent. Symmetric over-bounding method [10] relaxes this constraint to account for correlated inputs $\mathbf{v}$, as long as $\mathbf{v}$ is an invertible linear transformation of a spherically symmetric random vector $\mathbf{w}$, denoted as $\mathbf{v} = \mathbf{G}\mathbf{w}$. $\mathbf{w}$ is a spherically symmetric random vector if the PDF of $\mathbf{w}$ is of the form $g(\mathbf{w}^T\mathbf{w})$ for some function g of a scalar variable.

It has been proved in [10] that the PDF of $x = \mathbf{a}^T\mathbf{v}$ is a scaled version of the PDF of any one of its inputs v_i:

$$p_x(x) = \frac{\|e_i^T G\|}{\|\mathbf{a}^T G\|} p_{v_i}\left(\frac{\|e_i^T G\|}{\|\mathbf{a}^T G\|}x\right) \tag{2.17}$$

where e_i is the ith standard basis vector in $\mathbb{R}^m$, $\|\mathbf{y}\|$ is the 2-norm of a real vector $\mathbf{y}$.

If any of the elements of $\mathbf{v}$ can be over-bounded in CDF sense, say

$$\bar{p}_{v_i} \succ p_{v_i} \tag{2.18}$$

then $\mathbf{x} = \mathbf{a}^T\mathbf{v}$ is over-bounded by a scaled version of $\bar{p}_{v_i}$.

$$\bar{p}_x(x) = \frac{\|e_i^T G\|}{\|\mathbf{a}^T G\|} \bar{p}_{v_i}\left(\frac{\|e_i^T G\|}{\|\mathbf{a}^T G\|}x\right) \succ p_x(x) \tag{2.19}$$

Symmetric over-bounding of a linear combination of correlated random vector inputs can be extended to bound the outputs of linear systems. More details on symmetric over-bounding can be found in [10].

2.6 Summary

Independent distribution over-bounding defines the basic notion of CDF over-bounding, and paired over-bounding provides a powerful tool to account for non-zero-mean or non-symmetric distributions. Both of these two methods don't require the individual variables to share the same type of distribution. Symmetric over-bounding extends the over-bounding technique to be applied to correlated input random signals rather than independent input random vectors. While these approaches have laid some of the foundations for the over-bounding problems, there are cases where these approaches are of limited utility. also have their limits. All of those methods apply only to the output of linear systems. So to over-bound the output of a nonlinear state space dynamic system like INS, while the insight from previous work will be useful, new methodology has to be developed.

Chapter 3

Inertial Sensor Errors Over-bounding

In general, inertial sensor output errors are the sum of two components: Deterministic errors and Random errors. To this end, this chapter presents four modeling methods for random errors [21]. Such method are reviewed and applied to inertial sensors. The advantages and shortcomings of these methods are discussed. Traditionally, stochastic modeling methods have been used to identify or precisely model the stochastic error components. The goal of the work in this thesis is to over-bound the errors using simple time-domain models. So, in this thesis, two over-bounding methods are proposed: Auto-correlation Function (ACF) over-bounding and Allan Variance over-bounding.

3.1 Inertial Sensors

'Inertial sensors' is a term used collectively for accelerometers and gyros. An accelerometer measures the specific force which is a combination of the sensed linear acceleration and the Earth's gravity. A gyro measures the angular rate of the coordinate frame to which it is attached relative to an inertial frame. Most types of accelerometers and gyros measure specific force and angular rates along a single sensitive axis. Typical Inertial Measurement Unit (IMU) for navigation purposes comprises of three accelerometers and three gyros to produce a three-dimensional or vector measurement of specific force and angular rate of the IMU body with respect to inertial space expressed in a coordinate frame attached to the IMU.

In an Inertial Navigation System (IMU) outputs are integrated to produce a position, velocity and attitude or a solution of the the navigation state vector. Due to inertial sensor output errors,

the navigation solution is corrupted by errors. Based on how quickly these errors grow with time, the inertial sensors used are classified into three categories normally referred to as consumer grade, tactical grade and navigation grade. The size, mass, performance and cost of inertial sensors varies by several orders of magnitude. Gyros can span six orders of magnitude in performance while accelerometers can span three orders of magnitude in performance [3].

Based on the sensing method, the gyros can be classified as spinning mass, optical, or vibratory, each of which is based on a different physical principle. Spinning-mass gyros operate on the principle of conservation of angular momentum, measuring the reaction of the spinning mass to the rotation of the gyro case. Optical gyros which includes Ring laser Gyro (RLG) and Fiber-Optic Gyro (FOG), rely on the Sagnac effect. In a given medium, light travels at a constant speed in an inertial frame. Vibratory gyros sense angular rate by measuring the Coriolis acceleration of a vibrating element inside the gyro. Low-cost and low-performance rate gyros are normally of this type and use MEMS technology for the sensing element.

Based on sensing method, the accelerometers can also be classified as either pendulous or vibrating beam type of sensors. Both of these types of accelerometers share the same basic principle. Pendulous accelerometers have a proof mass which is attached to the case via a pendulous arm and hinge. It can have either an open-loop or closed-loop (force-feedback) configuration. Vibrating beam resonant accelerometers have a vibrating beam supporting proof mass. When a force is applied to the accelerometer case, the resonant frequency of the vibrating beam is changed which can be measured to determine the specific force along the sensitive axis. Both pendulous and vibrating beam accelerometers can be built using either a conventional mechanical design or MEMS technology [3].

The IMUs normally contain a processor which detects sensor failure as well as provides compensation for the deterministic raw inertial sensor errors. As such we will not focus on deterministic errors in this chapter.

3.2 Inertial Sensor Output Errors

Even if the initial error-free conditions for position, velocity and attitude are available, the navigation solution obtained from integration of inertial sensor measurements will still be erroneous. This is due to inertial sensor errors and, thus, it is important to understand inertial sensor error

characteristics and how to overbound them.

As noted earlier inertial sensor output errors can be divided into two parts: Deterministic (systematic) errors and Stochastic (random) errors [21]. The random noises of inertial sensors come from a number of sources depending on types of sensors. Electrical noise limits the resolution of inertial sensors, especially MEMS sensors. Pendulous accelerometers and spinning-mass gyros exhibit noise due to mechanical instabilities, while the residual lock-in effects of an RLG, after dithering is applied, manifest as noise.

The deterministic errors include scale factor error, misalignment and bias. Each systematic error has four components, a fixed contribution, its variation due to change of environment factors such as temperature or acceleration, a run-to-run variation and an in-run variation. The first two components are present each time the sensor is used and can be corrected by the IMU using laboratory calibration data. The method is to identify these external factors and develop a model describing their effects on the sensor errors. If one compensates for the output errors caused by these external factors, using a look-up table for example, their contribution to the output error is removed [22]. It is impossible, however, to identify all of these external factors. Even if it were possible to identify them, it would be impossible to *completely* remove the errors caused by them, since there will be a residual error (albeit small) left after compensation. The run-to-run variation results in a contribution to the error source that is different each time the sensor is used but remains constant within any run. It cannot be compensated by the IMU processor, but can be calibrated by the INS alignment and/or integration algorithms each time the IMU is used. Finally, the in-run variation is the component slowly changing during the course of a run. It cannot be corrected by the IMU processor or by an alignment process. Theoretically it can be corrected by integration algorithm, but it is difficult to observe in practice. For modeling purposes these residuals after compensation and initial alignment and these in-run variations which are hard to observe and compensate are combined with the other random effects.

The focus of this Chapter is developing stochastic models for the combined residual and random errors which can be included in estimator (e.q. Kalman filter) states. It should be noted that, the resulting error models are stochastic in nature and, thus, cannot be used to improve the sensor output. Instead, they are used to provide a statistical bound on the expected output errors caused by these un-modeled or post-calibration residual effects.

If we use y to denote sensor outputs, then the general post calibration model proposed to describe these errors has the following form:

$$y_m = (1+k)y_t + b(t). \tag{3.1}$$

In Equation 3.1, y_m is the sensor's measured output and y_t is the true value of the quantity that the sensor is measuring. Stated differently, y_m is the sensors representation of y_t. The true value y_t is corrupted by a scale factor error, k, and a bias, $b(t)$ which, in general, is time varying. Since we are interested in modeling post calibration errors, $b(t)$ can be thought of as the residual output of the sensor when no input is applied. Thus, it can be measured or observed when the sensor is static.

For these low cost inertial sensors, we focus more effort on modeling the stochastic nature of the residual $b(t)$ instead of the scale factor error k. This is because, the effects of stochastic variations of the scale factor error is smaller in comparison to the effects of the variations in $b(t)$. As an example of this consider the experimental data shown in Figure 3.1. This shows estimates of the combined $1+k$ as a function of temperature for an automotive-grade rate gyro. The data was collected from a rate table inside a temperature-controlled environmental chamber. The different color lines represent different data sets collected at different times. The data clearly shows that k is a function of temperature. However, the variability of k from one data set to the next is very small. This implies that the change of k over a small time window when these sensors are being used in a stand-alone fashion is going to be small. Thus, a stochastic error model for the scale factor is unnecessary. This does not imply that an estimator used for blending the output from these sensors with a GNSS receiver should not include a state for scale factor error. What it implies is that the scale factor can be modeled adequately as a random constant.

The situation with the bias term, however, is different. If we divide the bias errors into time varying and time-invariant components, then without a loss of generality we can assume $b(t)$ has the following form:

$$b(t) = b_0 + b_R(t). \tag{3.2}$$

The term b_0 represents a *constant* null-shift. Its value is sometimes listed on data sheets for inertial sensors and is referred to as the "turn-on to turn-off" bias. It is relatively easy to estimate. The term $b_R(t)$ represents the random bias drift, or the residual of the bias after calibration. The term "drift" implies that it is time-varying. Since b_0 is relative easy to determine, the focus in this chapter

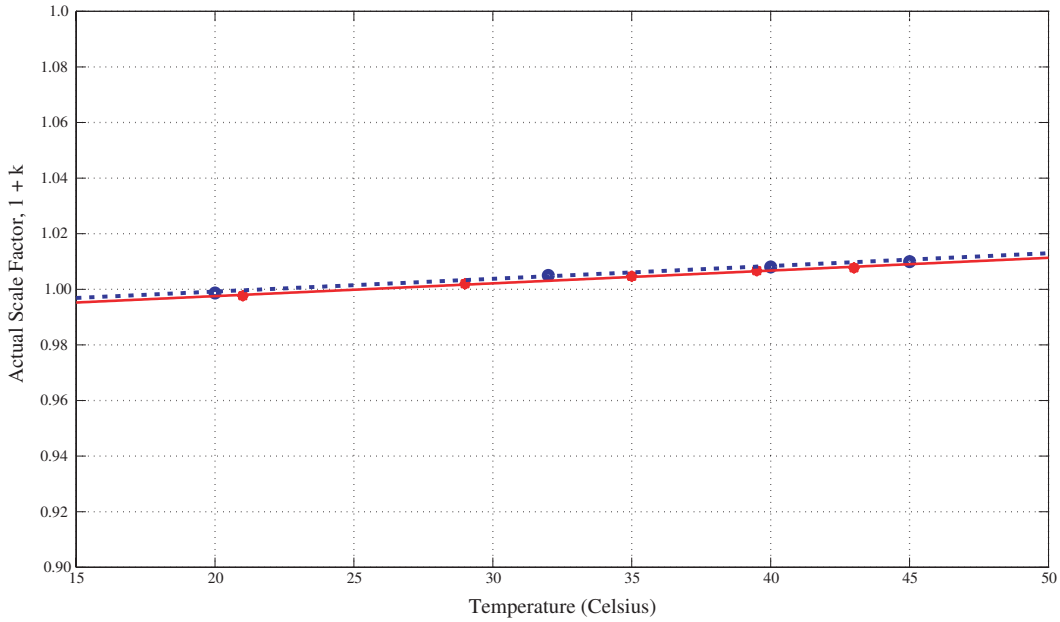

Figure 3.1: Scale Factor versus Temperature for the Automotive-Grade Rate Gyro Used in the MIDG II Inertial Navigation System [1]

is primarily associated with characterizing $b_R(t)$ for low cost inertial sensors. Characterizing b_R means developing a stochastic model to describe its behavior.

3.3 Modeling Stochastic Error

In modeling b_R the autocorrelation function, Power Spectral Density (PSD) function, time series analysis and Allan variance are four tools normally used. If we regard the original underlying random process as a black box, the models constructed have similar output characteristics (autocorrelation, PSD etc) as the original unknown process.

The data used to develop error models for the inertial sensors we are interested in here is the output data from a sensor subjected to zero input. The collected data is a discrete representation of y_m as defined in Equation 3.1. The data is sampled at a rate of f_s Hertz (sampling period is T_s) and recorded for T seconds. If the sensor (without loss of generality we can assume it is a gyro) that is being characterized is supplied with a temperature correction function or a temperature-versus-output-error-look-up table, then the data collection does not have to occur at a constant temperature.

This is because our objective is to model the stochastic *as well as* post-calibration residual errors. That is, in the case where a temperature compensation function or look-up table is provided, the data used will be sensor output samples after they have been corrected for temperature effects.

3.3.1 Autocorrelation function method

The definition of the autocorrelation function of a random process $b_R(t)$ is:

$$R_{b_R}(t_1,t_2) = E[b_R(t_1)b_R(t_2)] \tag{3.3}$$

where E is the expectation operator and t_1 and t_2 are arbitrary sampling times. If the random process $b_R(t)$ is stationary, its autocorrelation function is a function only of the time difference $\Delta t = t_2 - t_1$. That is,

$$R_{b_R}(\Delta t) = E[b_R(t)b_R(t+\Delta t)] \tag{3.4}$$

Figure 3.2 shows the autocorrelation plot for an automotive grade gyro found in the Crossbow μNav IMU [2]. A spike at zero lag (Δt=0) dominates the plot which indicates the presence of a wide band (uncorrelated) process. Thus, we can decompose $b_R(t)$ into wide band and correlated components as follows,

$$b_R(t) = b_w(t) + b_c(t) \tag{3.5}$$

where $b_w(t)$ is a wide band noise process, and $b_c(t)$ is a correlated process. The autocorrelation function of $b_R(t)$ is then of the form

$$\begin{aligned} R_{b_R}(\Delta t) &= E[b_R(t)b_R(t+\Delta t)] && (3.6)\\ &= E[(b_w(t)+b_c(t))(b_w(t+\Delta t)+b_c(t+\Delta t))] && (3.7)\\ &= E[b_w(t)b_w(t+\Delta t)] + E[b_c(t)b_c(t+\Delta t)] && (3.8)\\ &= \sigma_w^2\delta(\Delta t) + R_{b_c}(\Delta t) && (3.9) \end{aligned}$$

since $E(b_w(t)b_w(t+\Delta t)) = \sigma_w^2\delta(\Delta t)$ where $\delta(\Delta t)$ is the delta function.

From Figure 3.2 we can see that the information and structure of the correlated process is "buried" by the wide band process. To model the correlated process $b_c(t)$ will require that we filter the process $b_R(t)$ to suppress the spike of the autocorrelation plot at zero tag $\Delta t = 0$. This can be done by averaging the original data. This is in effect equivalent to low pass filtering the data.

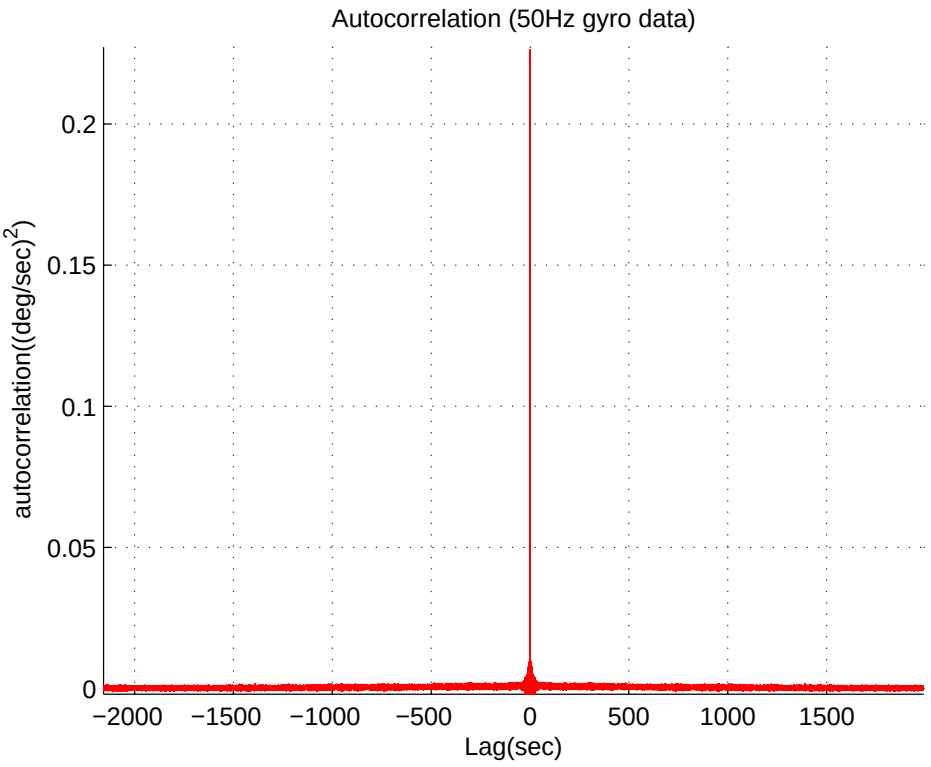

Figure 3.2: Autocorrelation plots for Typical Low Cost Rate Gyros–Crossbow μNav [2].

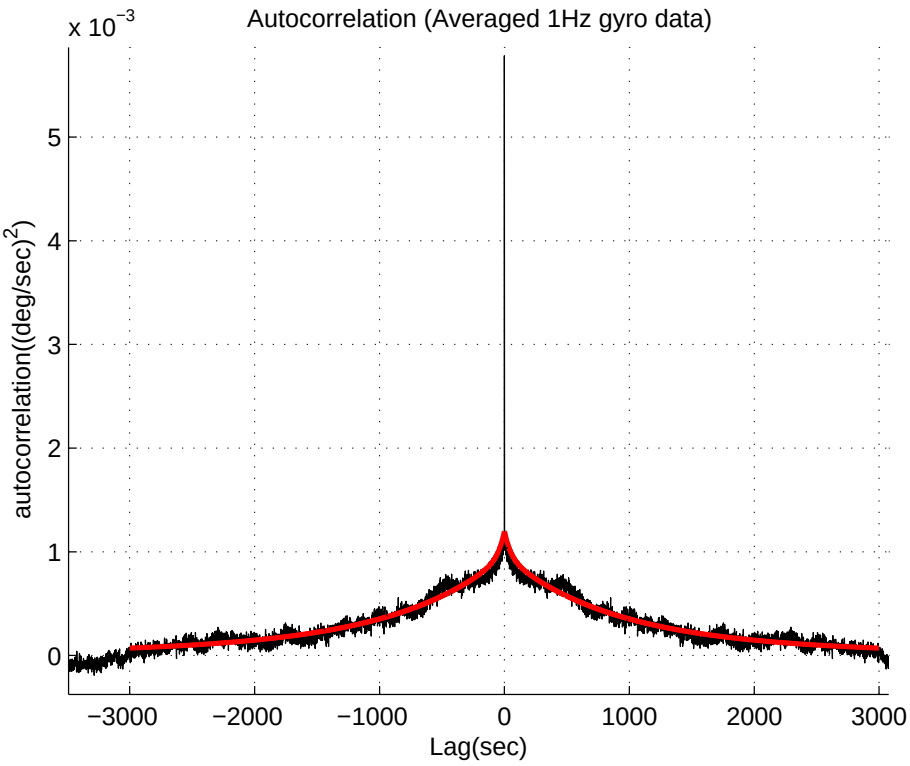

Figure 3.3: Autocorrelation Plots for Crossbow μNav IMU gyros (averaged 1hz gyro data).

During this filtering, the wide band noise will still stay uncorrelated with a variance of $\sigma_{b_w}^2 / f_s$. Furthermore, the correlated noise will remain almost unaltered if we ensure that its correlation time is much larger than the correlation time of the filter. Figure 3.3 shows the autocorrelation plot of the filtered data. The spike is still dominant but is suppressed so that the structure of the correlated process $b_c(t)$ is apparent in the plot. Figure 3.4 shows a zoomed in version of the autocorrelation plot for $b_c(t)$, where the correlated nature of $b_c(t)$ is readily apparent.

The relationship between autocorrelation function and a random process is not one-to-one. Usually certain canonical forms are chosen for the parametric models and the model parameters are then estimated to fit the autocorrelation plot obtained from real data. For example, white noise or white sequence is commonly used to model the uncorrelated process. For correlated processes one commonly used model is the first order Gauss-Markov process here denoted as $s(t)$. It is important because a lot of random processes in reality can be approximated by the first order Gauss-Markov

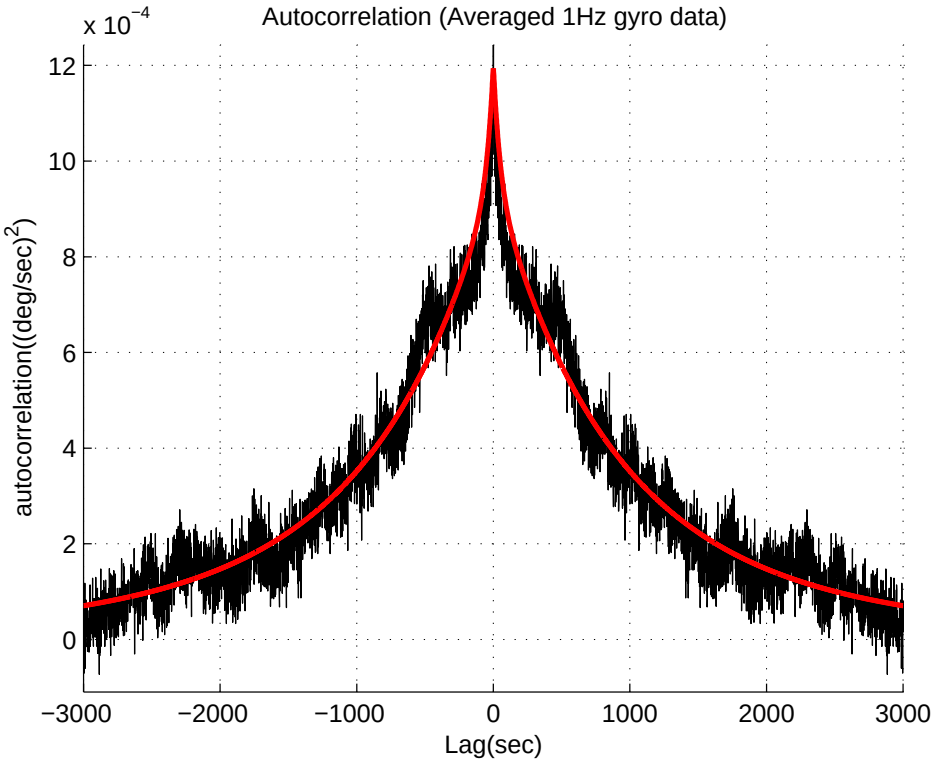

Figure 3.4: Autocorrelation Plots for Crossbow μNav IMU gyros. Averaged 1 Hz data zoomed to show the details of the correlated process.

process, and it is easy to describe mathematically. Sometimes a higher order Gauss-Markov process or a combination of multiple first order Gauss-Markov process can be used to have a better modeling of the underlying process [6, 23]. This will be demonstrated shortly.

The first order Gauss-Markov process can be thought of as the output of a first order low-pass filter with cutoff frequency f_c of $1/2\pi\tau$. The input to the filter is a white noise process $w(t)$ with a PSD of $Q_w = 2\sigma_s^2/\tau$ where σ_s^2 is the variance of $s(t)$. A time domain description of the process can be written as the following first order stochastic differential equation:

$$\dot{s}(t) = -\frac{1}{\tau}s(t) + w(t). \tag{3.10}$$

The variable τ is the time constant (or correlation time) and $w(t)$ is the driving white process noise [23]. The autocorrelation function of this process is of the form

$$R_s(\Delta t) = \sigma_s^2 e^{-\frac{|\Delta t|}{\tau}} \tag{3.11}$$

The autocorrelation function approaches zero as Δt approaches infinity.

The autocorrelation plot of the correlated process $b_c(t)$ shown in Figure 3.4 does not fit a single first order Gauss-Markov process well, since $R_c(\Delta t)$ decreases very fast initially when Δt is small and then decreases slowly when Δt is large. This is an indication of the presence of higher order Gauss-Markov process, or a combination of multiple first-order Gauss-Markov processes with different time constants. Here by trial and error a model with three first-order Gauss-Markov processes are fitted to $R_c(\Delta t)$

$$\hat{R}_c(\Delta t) = 0.2\sigma_c^2 e^{-\frac{|\Delta t|}{50}} + 0.6\sigma_c^2 e^{-\frac{|\Delta t|}{800}} + 0.2\sigma_c^2 e^{-\frac{|\Delta t|}{2000}} \tag{3.12}$$

where $\sigma_c^2 = 12 \times 10^{-4}(deg/sec)^2$ is the variance of the correlated process $b_c(t)$. The "hat" above R indicates that it is an estimate or approximation of $R(t)$.

Equation 3.12 leads us to the following observation: $b_R(t)$ is the superposition of a wide band noise process and *several* correlated stochastic processes. Thus, it is reasonable to model post-calibration residual errors as:

$$b_R(t) = b_w(t) + b_c(t) = b_w(t) + \sum_{i=1}^{N} b_i(t) \tag{3.13}$$

where $b_w(t)$ is a wide band noise process, $b_c(t)$ is a correlated process and is the sum of several $b_i(t)$ where $b_i(t)$ is the i^{th} correlated process. How to pick up N and develop an error model which is a compromise between accuracy and usability are the issues we will deal with in the reminder of this chapter.

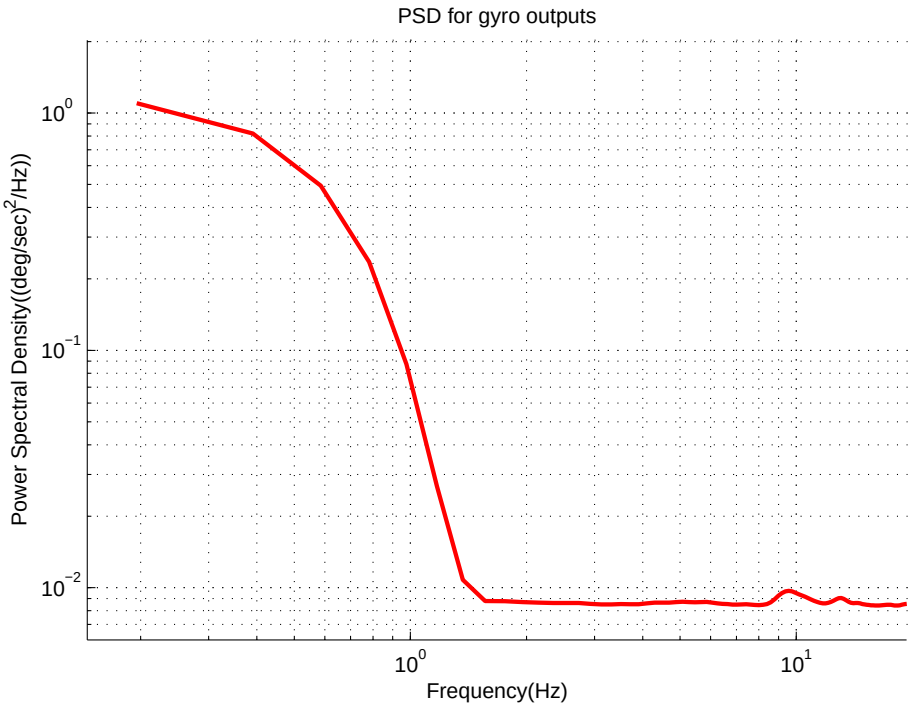

Figure 3.5: PSD plots for Crossbow μNav averaged 50hz gyro data.

3.3.2 Power Spectral Density (PSD) Method

The power spectral density (PSD) is a Fourier transformation of the autocorrelation function,

$$S(\omega) = \int_{-\infty}^{\infty} e^{-j\omega\Delta t} R(\Delta t) d\Delta t \tag{3.14}$$

Figure 3.5 shows the PSD for the μNav gyro output error plotted on a logarithm scale. The canonical candidate processes that will fit this data usually have a form of $1/f^2$, $1/f$ or $1/f^0$. They are represented on the PSD plot by straight lines with different slopes. The PSD of the first order Gauss-Markov process is given by [5, 24]:

$$S_{b_1}(f) = \frac{Q_{w_{b_1}} \tau_{b_1}^2}{1 + (2\pi\tau_{b_1} f)^2} \tag{3.15}$$

where τ_{b_1} is the time constant of the process and $Q_{w_{b_1}}$ is the constant PSD of the driving white noise w_{b_1}. This model can be used to fit the low-frequency part of the PSD plot.

Based on previous observations from the PSD plot, we can model $b_R(t)$ as the superposition of a wide band noise process, correlated stochastic processes with PSD $1/f^2$ or $1/f$ and a first order

Gauss-Markov process.

3.3.3 Time Series Analysis Method

The discipline of time series analysis provides various techniques that can be used for modeling random process. These are techniques for fitting random models (e.g., ARX, ARMA, or Box-Jenkins) to data [25]. Modern methods like OKID and subspace identification techniques discussed in [26] can also be used. These methods will simultaneously identify the mathematical form and determine the numerical values of the parameters in the mathematical models. However, these tools tend to result in mathematical models that are of a high order and are specific to a given sensor. Here we want to find a unified error model for a given class of sensors. So these tools are not efficient for our purpose.

3.3.4 Allan Variance Method

The theory and details of the Allan variance method can be found in the seminal work on the topic documented in [27] as well as applications of the method to inertial sensor error modeling given in [21], [28] and [29]. The Allan variance of a random process is a time domain analog of its Power Spectral Density (PSD).

Construction of an Allan variance chart using this data is done as follows:

1. Define a vector of averaging times, τ_a, as:

$$\tau_a = \left[\; T_s \text{ sec}, \quad 2T_s \text{ sec}, \quad \cdots, \quad \tfrac{T}{2} \text{ sec} \; \right]. \tag{3.16}$$

2. For each τ_a, divide the entire data record into $M = T/\tau_a$ clusters.

3. For each k^{th} cluster, compute the cluster time average of s_m denoted $\bar{s_k}$:

$$\bar{y_k} = \frac{1}{\tau_a} \int_{t_k}^{t_k+\tau_a} y_m(t)dt, \tag{3.17}$$

   For discrete data such as the collected sensor output samples, the above integral can be approximated by:

$$\bar{y_k} = \frac{1}{L} \sum_{i=1}^{L} y_m(t_i), \text{ where } L = f_s\tau_a \text{ and } k = 1, 2, 3, \cdots M \tag{3.18}$$

4. Use these cluster averages to form a new variable called the Allan variance (β^2) defined as follows:

$$\beta^2(\tau_a) = \frac{1}{2} E\left[\bar{y}_{k+1} - \bar{y}_k\right]^2, \tag{3.19}$$

where E is the expectation operator.

5. On a log-log scale, plot $\beta(\tau_a)$ versus τ_a.

From [28] and [29] we know that the Allan variance, $\beta^2(\tau_a)$, of a time series of data collected over a time interval T seconds long, is related to the PSD of the output noise $S(f)$ by the following integral equation (where f is frequency):

$$\beta^2(\tau_a) = \frac{4}{\pi\tau_a} \int_0^\infty S\left(\frac{u}{\pi T}\right) \frac{\sin^4 u}{u} du. \tag{3.20}$$

For example, if the rate gyro output errors or post-calibration residuals consisted only of white noise with PSD $S(f) = Q^2 =$ constant, then it can be shown that the Allan variance of this process is:

$$\beta^2(\tau_a) = \frac{Q^2}{\tau_a} \tag{3.21}$$

When plotted on a log-log plot, this will appear as a linear function with slope of $-1/2$:

$$\log(\beta(\tau_a)) = \log(Q) - \frac{1}{2}\log(\tau_a). \tag{3.22}$$

Other random processes corrupting the inertial sensor output or present in the post-calibration residuals will appear as lines with the slopes given in Table 3.1.

Figure 3.6 shows the Allan variance for two different brands of low cost gyros. The data used to construct the Allan Variance plots is the 3-hour static output data sampled at 50 Hz. While the Allan variance for all of these gyros exhibit a $-1/2$ slope for small τ_a, for larger τ_a values the slopes are seen to increase gradually to zero and are sometimes positive. From this observation it can be concluded that a stochastic model for $b_R(t)$ would be the superposition of wide band noise and correlated noises.

To see the structure of the correlated noise more clearly, the Allan variance for one μNav gyro only is shown in Figure 3.7. The correlated and uncorrelated parts of the output errors are separated using a method described later and plotted separately as shown in Figure 3.7. It can be seen that that the correlated noise exhibits a slowly changing and slightly positive slope. It does not match

Error Mechanism	Allan Variance Slope
Wide-Band Noise	$-\frac{1}{2}$
Quantization Noise	-1
Exponentially Correlated Noise (First Order Gauss-Markov Process)	$[-\frac{1}{2}, +\frac{1}{2}]$ (depends on value of τ_a)
Rate Random Walk	$+\frac{1}{2}$
Linear Rate Ramp	$+1$
Flicker Noise	0

Table 3.1: Summary of Standard Error Sources and their Respective Allan Variance Slopes

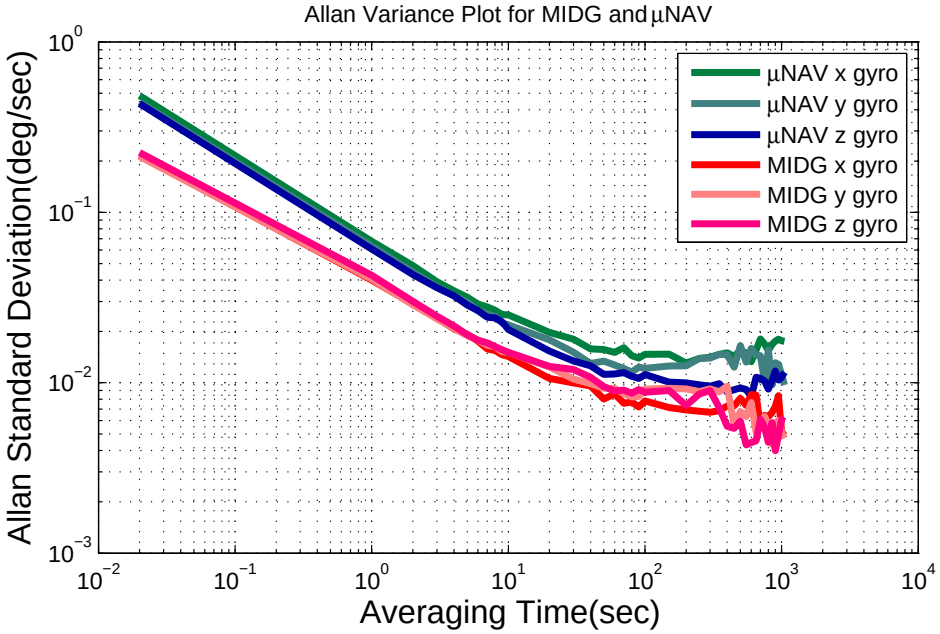

Figure 3.6: Allan Variance Plots for Low Cost Rate Gyros founded in the Crossbow μNav [2] and the MIDG II Inertial Navigation System [1].

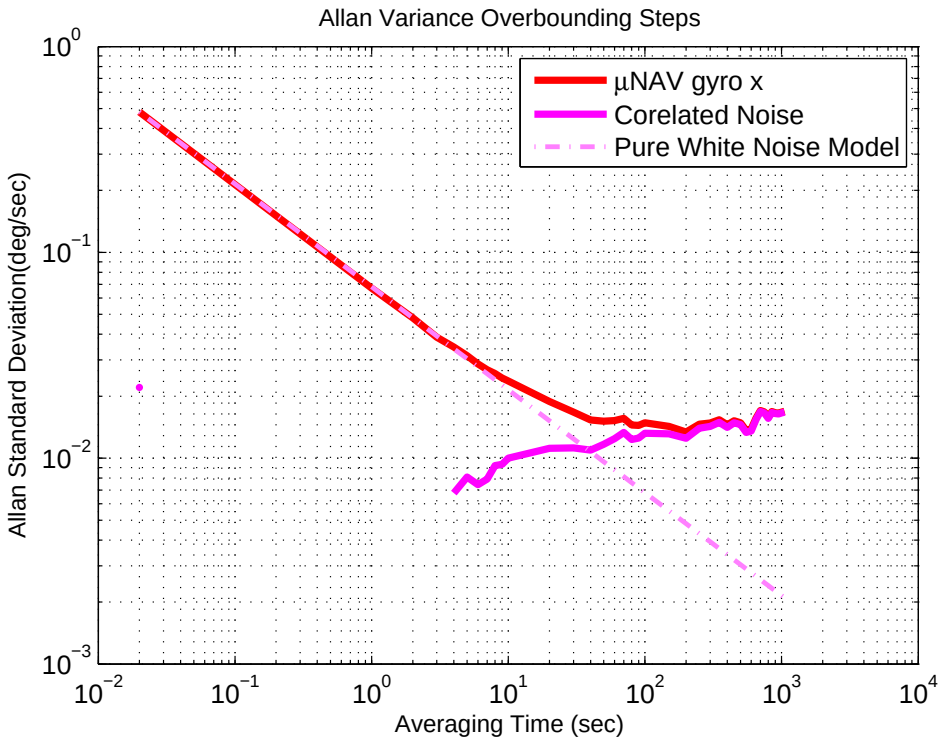

Figure 3.7: Allan Variance Plots for Crossbow μNav Gyro showing White Noise and Correlated Noise.

exactly any of the slopes identified in Table 3.1. Prior work associated with low cost inertial sensors has typically modeled the error associated with the zero-slope part of the Allan variance as a flicker noise process or bias instability [30–34].

Based on these observations, we note that $b_R(t)$ is the superposition of a wide band noise process (which is the dominant error source for small τ_a) and several correlated stochastic processes (which become dominant for larger values of τ_a). Thus, it is reasonable to assume a model for b_R or the post-calibration residual errors has the same form as that given in Equation 3.13:

$$b_R(t) = b_w(t) + b_c(t) \tag{3.23}$$

where $b_w(t)$ is a wide band noise process, $b_c(t)$ is a correlated process.

3.4 The Output Bias Over-bounding

From the previous section we know $b_R(t)$ is the super-positions of wide band noise and correlated processes. The correlated process $b_c(t)$ can be modeled as a combination of several first order Gauss-Markov processes. It can be identified in the time domain using the autocorrelation method, or a high-order ARMA model using time series analysis, or a combination of flicker noise and random walk in the frequency domain using the Allan variance method. However, a flicker noise process is difficult to model in the time-domain with a finite-order state model and is sometimes approximated as the combination of several exponentially correlated noise terms with different correlation times. If we want the model to be more accurate, the model will be more complex and have more terms and parameters. We assume the number of parameters in the model is N. The general error model of $b_R(t)$ is of form

$$b_R(t) = b_w(t) + b_c(t) = b_w(t) + \sum_{i=1}^{N} b_i(t), \tag{3.24}$$

where b_i is the i^{th} correlated process. As noted earlier, however, the objective of this chapter is to develop an error model which is a compromise between accuracy and usability. If N is large, including all N correlated error terms would negatively affect usability. Reducing the number of correlated error terms included in the model enhances usability but at the cost of accuracy. In addition, noting that these low-cost sensors are normally used in a setting where they are integrated with an aiding sensor and relied on in a stand-alone fashion only for brief moments, the detailed modeling of long term error characteristics is unnecessary.

As a compromise between usability and accuracy, we propose retaining a single correlated error term (denoted $b_1(t)$) with parameters that can be adjusted to approximate and over-bound the correlated noise whose precise meaning will be clarified in the next section. The proposed form for $b_1(t)$ will be an exponentially correlated or first order Gauss-Markov process where the variance $\sigma_{b_1}^2$ and time constant τ_{b_1} are the parameters. Before we justify the reasonableness of replacing $\sum_{i=1}^{N} b_i(t)$ in Equation 3.24 with a single Gauss-Markov process $b_1(t)$, we note that the proposed form of $b_R(t)$ is $b_R(t) = b_w(t) + b_1(t)$ and the resulting total error model for the residual $b(t)$ is:

$$b(t) = b_0 + b_w(t) + b_1(t). \tag{3.25}$$

This total error model is schematically depicted in Figure 3.8 where the physical meaning of each of the terms in Equation 3.25 is shown graphically.

A closer examination of the first order Gauss-Markov process is important to subsequent discussions. The Allan variance of this process as a function of averaging time τ_a is [21]:

$$\beta^2(\tau_a) = \frac{Q_{w_{b_1}} {\tau_{b_1}}^2}{\tau_a}[1 - \frac{\tau_{b_1}}{2\tau_a}(3 - 4e^{-\frac{\tau_a}{\tau_{b_1}}} + e^{-\frac{2\tau_a}{\tau_{b_1}}})]. \tag{3.26}$$

When τ_a is much smaller than the correlation time τ_{b_1}, the limit is a random walk process with the driving process noise of PSD $Q_{w_{b_1}}$:

$$\beta^2(\tau_a) = \frac{Q_{w_{b_1}}}{3}\tau_a. \tag{3.27}$$

When τ_a is much larger than the correlation time τ_{b_1}, the limit is a white noise process with PSD $Q_{w_{b_1}}\tau_{b_1}^2$:

$$\beta^2(\tau_a) = \frac{Q_{w_{b_1}}\tau_{b_1}^2}{\tau_a}. \tag{3.28}$$

Compared with a random walk model we have more flexibility when using a first order Gauss-Markov process because we have two parameters with which we can tune the model. We can have a tighter bound using Gauss-Markov process model other than random walk model.

3.4.1 Bias Over-Bounding using Autocorrelation

Now the definition of over-bounding of $b_c(t)$ is given as:

Definition 1: $b_c(t)$ and $b_1(t)$ are zero mean random processes. Let $x_t = \int_0^t b_c(u)du$ and $\tilde{x}_t = \int_0^t b_1(u)du$. If $Var(x_t) \leq Var(\tilde{x}_t)$ for every $t \in [0, T_{max}]$, we say $b_c(t)$ is over-bounded by $b_1(t)$ in a second order moment sense in time duration T_{max}. If random variable x_t is over-bounded by random variable $\tilde{x}_t$ in CDF sense for every fixed $t \in [0, T_{max}]$, we say $b_c(t)$ is over-bounded by $b_1(t)$ in the CDF sense in the time interval $[0, T_{max}]$.

The physical meaning of this definition can be explained as follows: If the $b_c(t)$ is the correlated noise on the rate gyro measurement, x_t will be the angle error that results when integrating rate gyro measurement from time 0 to time t. We want to model and overbound the gyro noise process $b_c(t)$ so that we can overbound the error on the integrated angle which is what we are ultimately interested in doing.

Conclusion 1: Let $R(\tau)$ and $\tilde{R}(\tau)$ be the autocorrelation functions for process $b_c(t)$ and $b_1(t)$. If $\tilde{R}(\tau) \geq R(\tau)$ for every $\tau \in [0, T_{max}]$, $b_c(t)$ is then overbounded by $b_1(t)$ in the second order moment sense in time interval $[0, T_{max}]$.

Proof:

$$\begin{aligned} Var(x_t) &= E(x_t^2) && (3.29)\\ &= \int_0^t du \int_0^t dv E(b_c(u)b_c(v)) && (3.30)\\ &= \int_0^t du \int_0^t dv R(u-v) && (3.31) \end{aligned}$$

So if $\tilde{R}(\tau) >= R(\tau)$ for every $\tau \in [0, T_{max}]$, we'll have $Var(\tilde{x}_t) >= Var(x_t)$ for every $t \in [0, T_{max}]$.

So conclusion 1 offers one method for finding the parametric model for $b_1(t)$.

Conclusion 2: If $b_c(t)$ is a spherically invariant random process [35, 36], and at any fixed time t the random variable $b_c(t)$ can be over-bounded by a Gaussian random variable in the CDF sense, then the first order Gauss-Markov process model $b_1(t)$ can over-bound $b_c(t)$ in a CDF sense in time duration T_{max}. So now we have shown that it is possible to replace $b_c(t) = \sum_{i=1}^{N} b_i(t)$ with a simple term $b_1(t)$ which can over-bound the true process in some physically meaningful sense.

In summary, a reasonable unified error model for the output errors of these inexpensive inertial sensors is one that has the form shown schematically in Figure 3.8. As shown in this figure, the bias $b(t)$ consists of time invariant and time-varying components. We will call the time invariant or constant part the null-shift and from Figure 3.8 it is clear why that is the case; it represents the shift of the output error away from zero. The time varying component consists of a wide band noise component and a correlated component. A model for the correlated part that can bound a reasonably wide variety of error mechanism is the first order Gauss-Markov process. In what follows we will show how to develop these overbounds.

3.4.2 Bias Over-Bounding using the Allan Variance method

In this thesis we propose the following simple Allan variance based procedure for getting initial estimates of τ_{b_1} and $\sigma_{b_1}^2$,which is detailed in Figure 3.9 using a μNav gyro as an example :

1. Generate an Allan variance plot from the sampled $b(t)$ data. Then plot the Allan variance of the correlated noise only by subtracting the white noise contribution from total Allan variance.

2. Compute $Q_{w_{b_1}}$, the constant PSD of the driving white noise. When τ_a is small compared with τ_{b_1} , the Allan Variance of a first order Gauss-Markov process has a limit form with a slope of

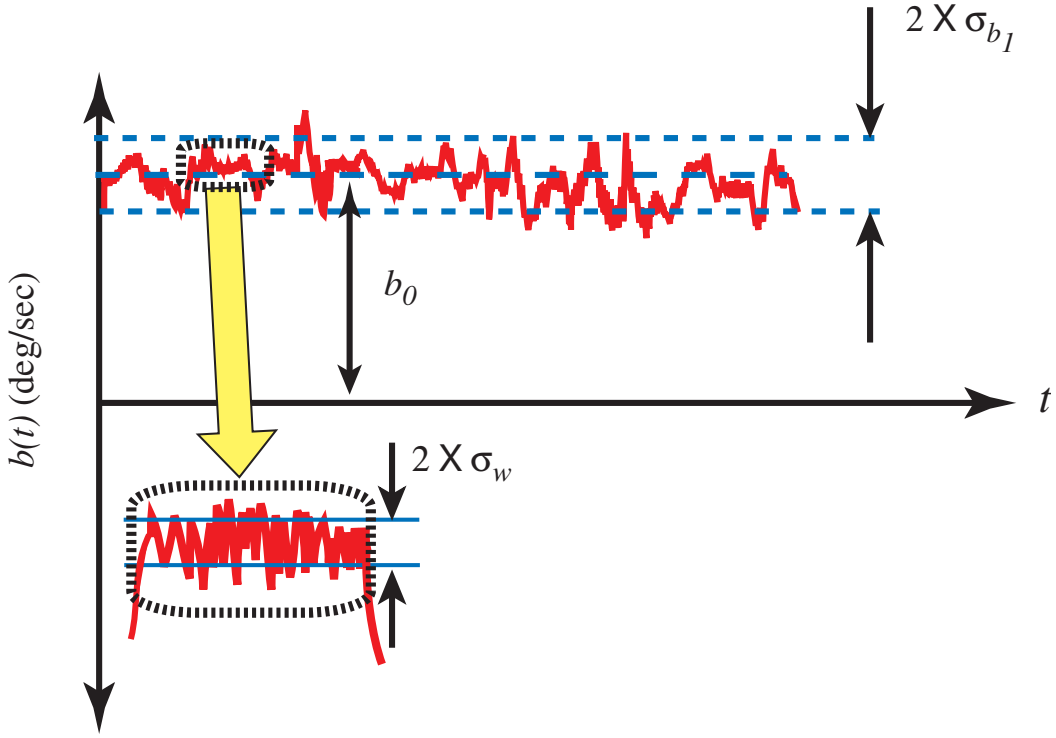

Figure 3.8: A Schematic of the General Error Model Proposed In this Paper

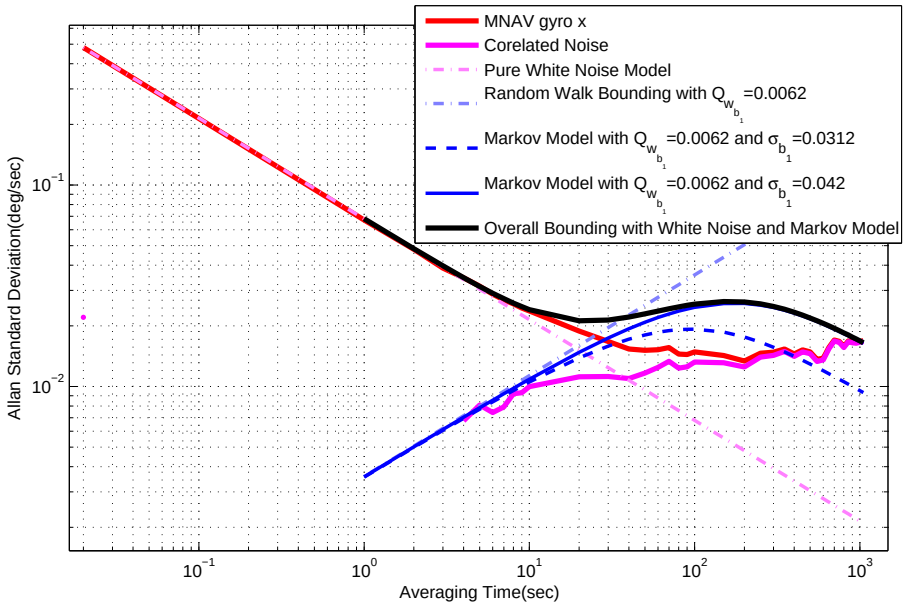

Figure 3.9: A Schematic Showing Over-bounding Procedure.

1/2 in a log-log plot. The position of this line is affected by $Q_{w_{b_1}}$ only. We want this limit line to over-bound the correlated noise from the upper-left on a log-log plot. For the data shown in Figure3.9 this over-bounding line leads to $Q_{w_{b_1}} = 0.0062^2 (deg^2/sec^3)$.

3. Generate an Initial Estimate of the Numerical Value for $\sigma_{b_1}^2$. From the original digital output data, the variance of the wide band noise is normally very large compared with the variance of the correlated noise. Thus, it is not easy to estimate the variance of the correlated noise directly from the original data. In this example, we filter the μNav gyro data first by averaging every 1 second data and obtaining a filtered 1 Hz data. During the filtering the uncorrelated noise will still stay uncorrelated with a variance of $\sigma_{b_w}^2 / f_s$. The resulting time series is shown in Figure 3.10. The Allan Variance plot of correlated noise will stay almost unaltered since it is in an averaging time range which is much larger than 1 second. The total variance of the filtered data will be a sum of the filtered wide band noise and correlated noise:

$$\sigma_{total}^2 = \sigma_{b_w}^2 / f_s + \sigma_{b_1}^2 \tag{3.32}$$

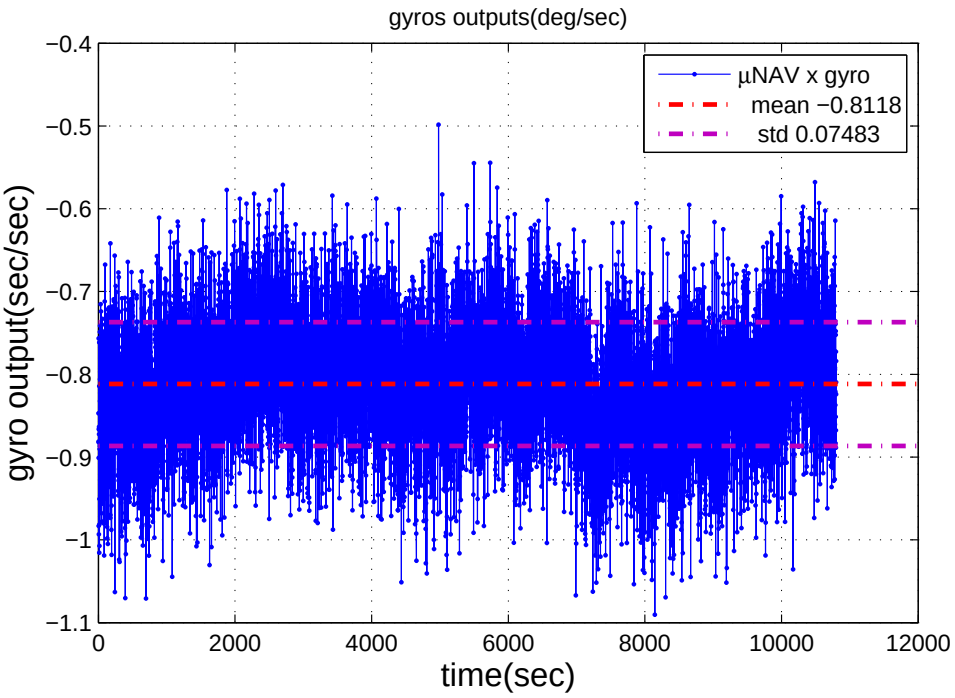

Figure 3.10: Crossbow μNav x Gyro Time Series (Averaged Every One Second).

From Figure 3.10,

$$\sigma_{b_1}^2 = \sigma_{total}^2 - \sigma_{b_w}^2 / f_s = 0.07483^2 - 0.482^2/50 = 0.000953 \tag{3.33}$$

so $\sigma_{b_1} = 0.0309(deg/sec)$

4. Determine the Numerical Value for $\sigma_{b_1}^2$. With previously estimated $Q_{w_{b_1}}$ and $\sigma_{b_1}^2$, we can plot the exponentially correlated noise in an Allan Variance plot, as shown in Figure 3.9. We can then adjust the value of σ_{b_1} to over-bound any averaging range we are interested with $Q_{w_{b_1}}$ fixed . At last, we determine $\sigma_{b_1} = 0.042(deg/sec)$.

5. Determination of Numerical Value for τ_{b_1}.
   $\tau_{b_1} = \frac{2\sigma_{b_1}^2}{Q_{w_{b_1}}} = \frac{2\times 0.042^2}{0.0062^2} = 92\ sec$

This procedure provides an initial estimate of σ_1^2 and τ_{b_1}. As we can see, we can bound the true process in the time span we are interested (here 0 sec to about 1000 sec) using a first order Gauss-Markov process by tuning τ_{b_1} and σ_{b_1}. Compared with the random walk model which has an ever

increasing variance and has a $+1/2$ slope in an Allan variance log-log plot, we can have a tighter bound using a first order Gauss-Markov process model with finite variance.

3.4.3 Relationship of Gauss-Markov Process Model to Flicker Noise Model

Since the flicker noise model is widely used in industry as an measure of the quality of inertial sensors, it is reasonable to compare the flicker noise model with a first order Gauss-Markov model. To do this, we consider the case where b_1 is passed through an 'integrator'. The output of the integrator is $x(t)$. If we model $b_1(t)$ as flicker noise with the coefficient B which can be read off from the Allan variance plot [29], the variance of $x(t)$ will be:

$$var[x(t)] = \frac{2}{\pi}B^2t^2. \tag{3.34}$$

If we model $b_1(t)$ as a first order Markov process with parameters $\sigma_{b_1}^2$ and τ_{b_1}, the variance of $x(t)$ will be:

$$var[x(t)] = 2\sigma_{b_1}^2\tau_{b_1}^2(\frac{t}{\tau_{b_1}} - 1 + e^{-\frac{t}{\tau_{b_1}}}). \tag{3.35}$$

When $t << \tau_{b_1}$, the limit case will be:

$$var[x(t)] = \sigma_{b_1}^2t^2. \tag{3.36}$$

When $t >> \tau_{b_1}$, the limit case will be:

$$var[x(t)] = 2\sigma_{b_1}^2\tau_{b_1}t. \tag{3.37}$$

So we can conclude that by choosing proper values for $\sigma_{b_1}^2$ and τ_{b_1} we can over-bound the flicker noise when t is in some chosen range but we will lose over-bounding when t goes to infinity. This is shown in Figure 3.11. In this example $B = 0.02deg/sec$, $\sigma_{b_1}^2 = 0.02deg/sec$ and $\tau_{b_1} = 200sec$. We can see we lose the over-bounding when t is greater than 310 seconds.

3.5 Over-bounding Model Parameter Values

In order to complete the mathematical description of $b(t)$, numerical values for its various components must be determined. The numerical values that must be determined include the following:

1. The null-shift b_0 and its variance $\sigma_{b_0}^2$.

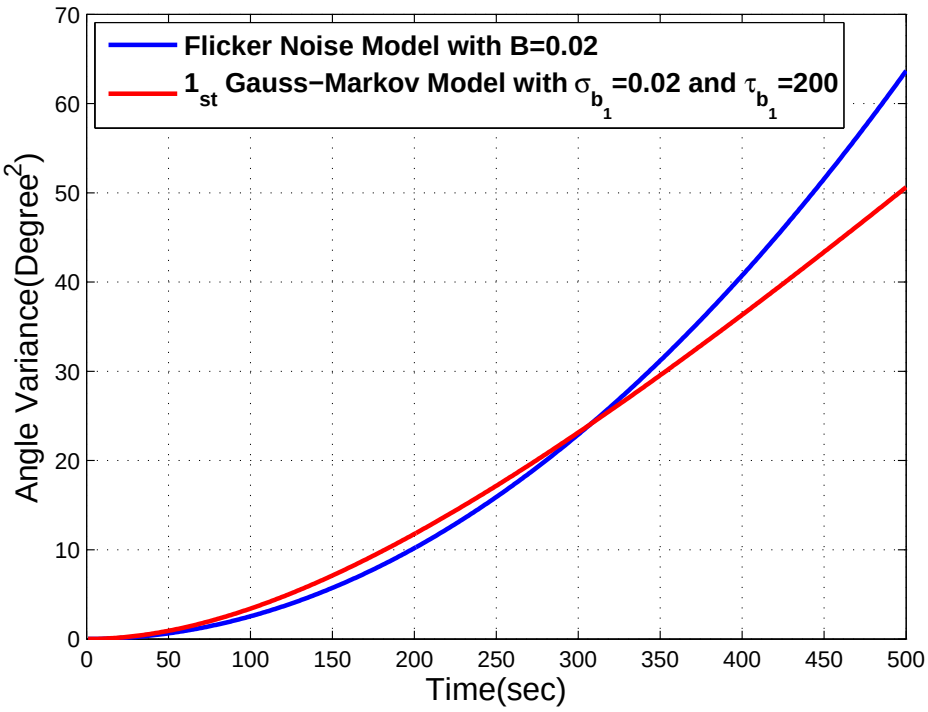

Figure 3.11: Example showing 1_{st} Order Markov Process to Over-bound the Flicker Noise.

2. The power spectral density of b_w, Q_w, or the variance of its discrete realization, $\sigma^2_{b_w}$.

3. The variance of $b_1(t)$, $\sigma^2_{b_1}$.

4. The correlation time of $b_1(t)$, τ_{b_1}.

3.5.1 Null Shift

The term b_0 is a null-shift and once a gyro is powered-on, its value remains relatively constant. Subsequently, if the gyro is powered-off then powered-on again, the new value of b_0 may be different. It will remain at this new constant as long as the gyro remains powered-on. This suggests that b_0 can be modeled as a random constant. The statistics of b_0 can be determined from an ensemble of experiments which consist of turning on the gyro, recording $b(t)$ and taking the mean of this data. Since the random constant model assumed for b_0 is non-ergodic and because both the wide band noise and first order Gauss-Markov processes are zero mean, the value of b_0 for each on/off cycle is the time average of $b(t)$. The value for b_0 computed for many such on-off cycles can be used to generate a description of the statistics for b_0.

The only question that remains is how many on/off cycles are required to accurately characterize $\sigma^2_{b_0}$? This question may be answered by noting how the knowledge of b_0 and $\sigma^2_{b_0}$ are used in integrated navigation applications. In many integrated navigation system applications such as those described in [37], [38], [39] and [40] the combination $b_0 + b_1(t)$ is continually estimated (in real time) using an observer. Thus, we do not need to know its value *a priori*. The primary use of $\sigma^2_{b_0}$ is for establishing initial conditions on state covariance matrices of sensor fusion system algorithms such as the Extended Kalman Filter. Since these algorithms refine the state covariance estimates continually, a precise knowledge of it may not be required.

3.5.2 Wide Band Noise

The wide band noise component of the error model, $b_w(t)$, is a random process which can be described in one of two ways. If we elect to use a continuous time description of the process, then it can be characterized by its PSD, Q_w. On the other hand, if we elect to use a discrete time description of the process, then the variance of discrete samples of $b_w(t)$ can be used. In the latter case, we are modeling $b_w(t)$ as a band limited white noise process or a white sequence [24]. Since most sensors

used in integrated navigation systems today have digital outputs and the sensor fusion algorithms that use them are discrete time systems, we will use the latter description of $b_w(t)$.

The variance of the discrete time description of b_w, σ_{b_w}, can be obtained by reading the Allan standard deviation value when τ_a is equal to T_s. However, considering the variation in constructing an Allan variance, it is better to draw a line with a slope of $-1/2$ in log-log plot to over-bound the Allan variance plot for small τ_a (for example, less than 5 sec), and reading the Allan standard deviation value of the over-bounding line when τ_a is equal to T_s.

Since the method of computing $\sigma^2_{b_w}$ discussed above assumes that $b_w(t)$ is a white noise sequence (band limited) and not a white noise process, it is valid to ask whether this assumption is justified. As shown in [37] this assumption is valid because the output of many low cost rate gyros is digital and has gone through significant processing that the end user cannot control. Thus, although b_w may be white noise process at the sensing element internal to the sensor, the output which follows internal sampling and filtering will have a power spectrum that is clearly band limited. In the case that the output is not digital, care must be taken and the sensor sampling rate must be taken into account before using the above method to estimate $\sigma^2_{b_w}$.

3.5.3 Correlated Noise

Since $b_1(t)$ is modeled as a first order Gauss-Markov process, we can completely describe it by using two parameters: Its correlation time, τ_{b_1}, and variance, $\sigma^2_{b_1}$. In theory, the variance and time constant of a first order Gauss-Markov process can be determined from a plot of the process' autocorrelation function, $R_{b_1}(t_1,t_2)$. In practice, however, this is difficult. This is because actual output data from low cost rate gyros is a combination of wide band noise and a correlated process. Furthermore, the magnitude of the wide band noise is much larger than the magnitude of the correlated noise. Another difficulty arises from the fact that in the modeling approach proposed here, we are replacing $\sum_{i=1}^{N} b_i(t)$ with $b_1(t)$. Since $\sum_{i=1}^{N} b_i(t)$ may be the superposition of multiple Gauss-Markov processes and potentially other random processes, it may not be possible to fit a single Gauss-Markov process to the sampled gyro data. In view of this latter point, we reiterate that in the approach proposed here, the first order Gauss-Markov process is used to over-bound the output errors and not necessarily model them *exactly*.

With these issues in view, we propose the following autocorrelation function based procedure

for getting initial estimates of τ_{b_1} and $\sigma^2_{b_1}$ since it is simpler than Allan variance-based method. We can pass this data through a low pass filter (e.g., 1 Hz averaging) to mitigate the effect of the wide band noise, and then construct the autocorrelation function of the filtered data. During this filtering, the uncorrelated noise will still stay uncorrelated with a variance of $\sigma^2_{b_w}/f_s$. Furthermore, the correlated noise will remain almost unaltered since its correlation time is in a range much larger than 1 second. The total variance of the filtered data will be the sum of the filtered wide band noise and correlated noise. Thus,

$$\sigma^2_{b_1} = \sigma^2_{total} - \sigma^2_{b_w}/f_s \tag{3.38}$$

By subtracting $\sigma^2_{b_w}/f_s$ from the autocorrelation function at time zero, we get the autocorrelation function of the correlated noise only. Using this value of σ_{b_1} and adjusting the value of τ_{b_1} we can over-bound the autocorrelation function for the correlated noise up to T_{max}, whose value depends on the particular application on hand and needs engineering judgement. For low cost inertial sensors, T_{max} should be less than several hundreds seconds.

3.6 Demonstrative Example

In order to demonstrate how one can construct rate gyro error models, we will present an illustrative example where we use a μNAV rate gyro output and apply the methodology outlined above. The output is from the gyro that is static (i.e. y_t in Equation 3.1 is zero). The output of the gyro is corrupted by a null-shift, wide band and correlated errors. A 3 hour time series of this gyro's output is collected and the data is sampled at 50 Hz to be used in the subsequent modeling exercise. Figure 3.12 shows this 3 hour time series. It is straight forward to obtain b_0 as it can be computed by averaging the long term data or using an estimator that is part of the navigation system that employs the sensor. From a simple averaging of the data used to construct Figure 3.12 yields the value of $b_0 = -0.722$ deg/sec.

To find σ_{b_w}, we construct an Allan variance plot as shown in Figure 3.6. Note that σ_{b_w} is equal to the value of the Allan variance when $\tau_a = T_s$ where T_s is the signal sampling rate. From Figure 3.6 we see that the value of the Allan variance at $\tau_a = T_s$ is 0.478 deg/sec. We filter the data by averaging every one second data to get a 1 Hz time series, which is shown in Figure 3.12. We then construct the autocorrelation function of the filtered data and subtract filtered white noise variance

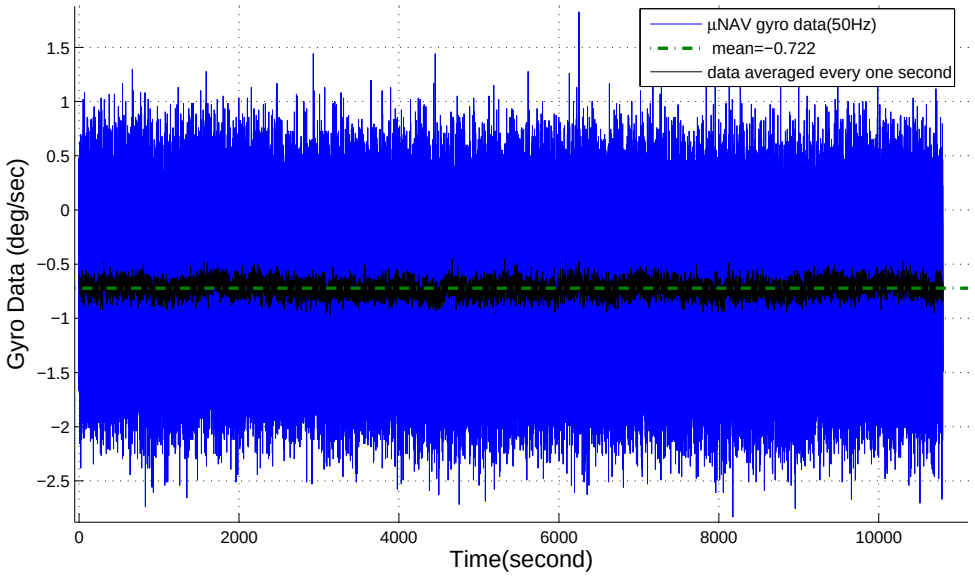

Figure 3.12: μNAV Gyro Output Data.

from this. Then we can get an over-bounding value for σ_{b_1} and τ_{b_1}. By choosing $T_{max} = 500$ sec,we get $\sigma_{b_1} = 0.03(deg/sec)$ and an associated time constant τ_{b_1} of 280 sec. The procedure is shown in Figure 5.4

From above procedures we get a model which can over-bound the second order moment of integration output. If we want to go one step further and find a model which can over-bound the output CDF, we need to look at the data CDF shown in Figure 4.4. This figure shows that the data distribution is well modeled by Gaussian distribution whose standard deviation is $\sqrt{\sigma_w^2 + \sigma_{b_1}^2} =$ 0.479 deg/sec. Thus, Gaussian over-bounding this is trivial.

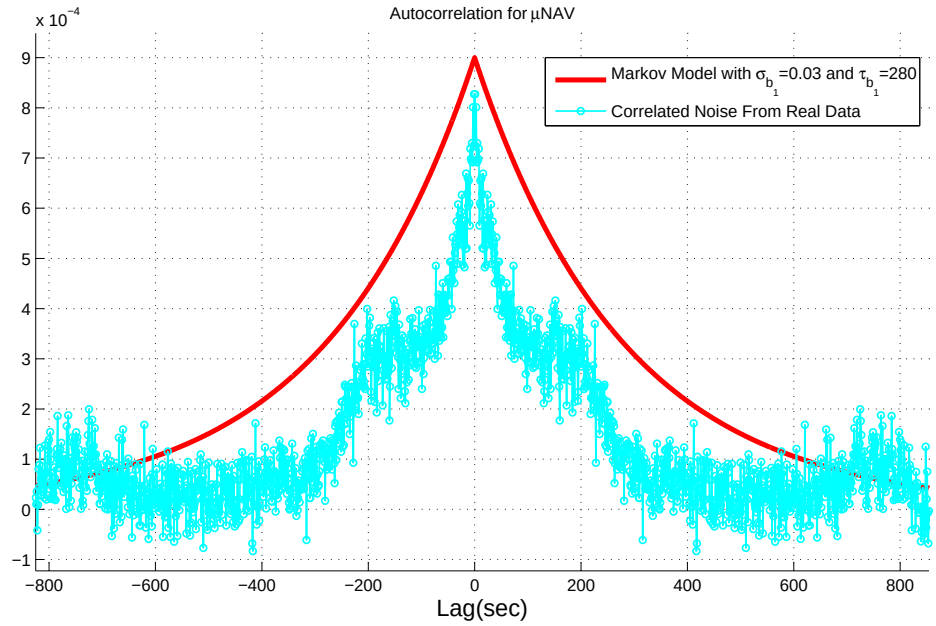

Figure 3.13: Example Showing Over-bounding of Autocorrelation Function of Correlated Noise) .

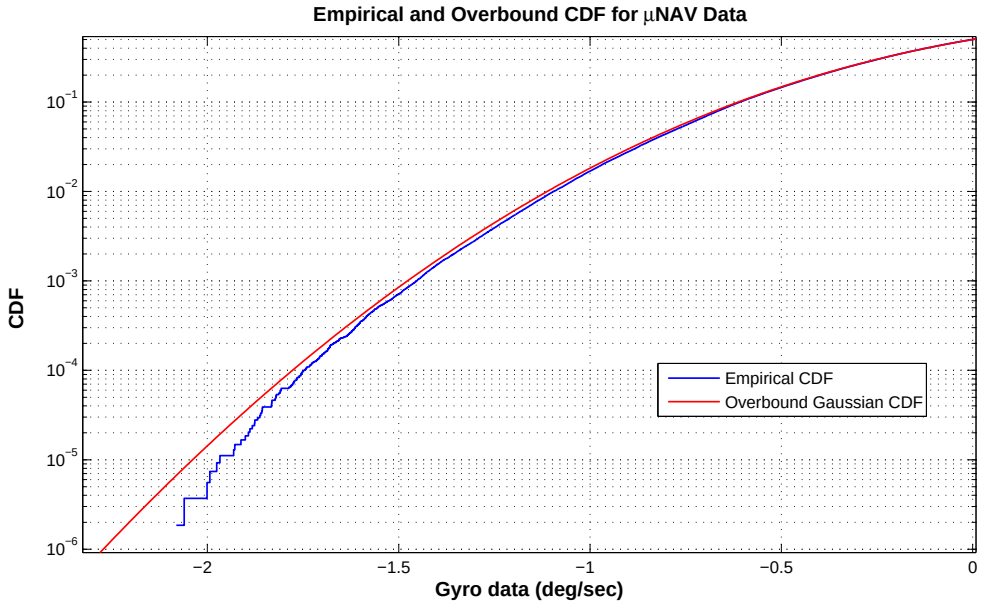

Figure 3.14: Example Showing Over-bounding of μNAV data CDF) .

Chapter 4

Over-bounding INS State Propagation

As noted earlier, integrated navigation systems blend the information from various sensors in real time to generate an optimal estimate of a vehicle's navigation state vector. In safety critical applications of integrated navigation systems, estimating the integrity risk is indispensible. As an example let us consider the automotive guidance and control problem [14–16] introduced in Chapter 1 (depicted in Figure 1.1). In this application precisely quantifying P_H is essential. This can be difficult to do in real time and thus, we must resort to an approximate but conservative approach. This can be done using an over-bounding of P_H. An over-bound provides a conservative guarantee because its accumulated tail probability always exceeds the actual value of P_H.

In this chapter we will examine the problem of over-bounding the nonlinear state propagation (time update) of integrated INS/GNSS system. Combined with GNSS over-bounding methods discussed in Chapter 2, this will build the foundation for a complete over-bounding of the INS/GNSS problem. While over-bounding methods discussed in Chapter 2 offer useful insights into the application of over-bounding in linear systems, the difficulty of over-bounding the INS problem lies in its nonlinear nature. We will first examine the over-bounding of the process noise, which is non-Gaussian and non-additive. It is shown that it can be over-bounded by Gaussian distribution. This is followed by a proof that the coordinate transformation of random variables (one of the non-linearities present in INS/GNSS problem) can be over-bounded by a Gaussian distribution. Over-bounding of the overall INS system output error distribution is then presented.

4.1 Over-bounding General Nonlinear State Propagation

Before we deal with the specific INS problem, we will examine a general non-linear system. Here we assume we have an *n*-state discrete-time nonlinear dynamic system, whose mathematical model is given as follows:

$$\mathbf{x}_k \quad = \quad \mathbf{f}_k(\mathbf{x}_{k-1}, \mathbf{u}_k) + \mathbf{g}(\mathbf{x}_{k-1}, \mathbf{u}_k)\mathbf{w}_k \tag{4.1}$$

where $\mathbf{x}_k$ is the state vector at time k, $\mathbf{u}_k$ is the control vector, and $\mathbf{w}_k$ is the process noise vector with zero-mean and covariance matrix $\mathbf{Q}_k$. Nonlinear filters which deal with such systems needs to deal with the nonlinear transformation of random variables. In Equation 4.1, for example, suppose $\mathbf{x}_{k-1} \sim (\hat{\mathbf{x}}_{k-1}, \mathbf{P}^{xx}_{k-1})$, where $\mathbf{x} \sim (\hat{\mathbf{x}}, \mathbf{P})$ means that random vector $\mathbf{x}$ has mean $\hat{\mathbf{x}}$ and covariance matrix $\mathbf{P}$ but does not have to be Gaussian distributed. We want to find the pdf, or at least the mean and variance of $\mathbf{x}$. When using an Extended Kalman Filter (EKF), the nonlinear transformation is expanded about $\hat{\mathbf{x}}_{k-1}$ in a multidimensional Taylor polynomial of the form

$$\mathbf{x}_k = \mathbf{f}(\hat{\mathbf{x}}_{k-1}, \mathbf{u}_k) + \mathbf{F}_k \cdot (\mathbf{x}_{k-1} - \hat{\mathbf{x}}_{k-1}) + \mathbf{g}(\hat{\mathbf{x}}_{k-1}, \mathbf{u}_k)\mathbf{w}_k + \ldots \tag{4.2}$$

where $\mathbf{F}_k$ is given by the Jacobian of $\mathbf{f}(x)$,

$$\mathbf{F}_k = \frac{\partial \mathbf{f}}{\partial \mathbf{x}}\Big|_{\hat{\mathbf{x}}_{k-1}}$$

If we keep just the first order term and ignore the higher order terms, we will have the approximation

$$E[\mathbf{x}_k] \approx \hat{\mathbf{x}}_k = \mathbf{f}(\hat{\mathbf{x}}_{k-1}, \mathbf{u}_k) \tag{4.3}$$

$$Var[\mathbf{x}_k] \approx \hat{\mathbf{P}}^{xx}_k = \mathbf{F}_k \mathbf{P}^{xx}_{k-1} \mathbf{F}^T_k + \mathbf{g}(\hat{\mathbf{x}}_{k-1}, \mathbf{u}_k)\mathbf{Q}_k \mathbf{g}(\hat{\mathbf{x}}_{k-1}, \mathbf{u}_k)^T \tag{4.4}$$

Thus we have approximations of the mean and covariance of $\mathbf{x}$. Generally we cannot derive the complete pdf of $\mathbf{x}$ only from its first and second order moments, but we can approximate the true pdf using a Gaussian distribution $N(\hat{\mathbf{x}}_k, \hat{\mathbf{P}}^{xx}_k)$ where $N(\hat{\mathbf{x}}_k, \hat{\mathbf{P}}^{xx}_k)$ means a Gaussian distribution with mean $\hat{\mathbf{x}}_k$ and variance $\hat{\mathbf{P}}^{xx}_k$. Note that the EKF contains only a first order polynomial expansion of the nonlinear functions, and, thus, cannot provide a guarantee for over-bounding the true distribution of $\mathbf{x}_k$ using an Gaussian approximation $N(\hat{\mathbf{x}}_k, \hat{\mathbf{P}}^{xx}_k)$. It is possible that the Gaussian approximation $N(\hat{\mathbf{x}}_k, \hat{\mathbf{P}}^{xx}_k)$ of the true distribution of $\mathbf{x}_k$ is accurate in the core but not in the far tail, which will be a problem if we are interested in defining an integrity bound.

It will be shown in detail later that Gaussian approximations $N(\mathbf{0}, \mathbf{g}(\hat{\mathbf{x}}_{k-1}, \mathbf{u}_k)\mathbf{Q}_k\mathbf{g}(\hat{\mathbf{x}}_{k-1}, \mathbf{u}_k)^T)$ cannot guarantee over-bounding of the true distribution of $\mathbf{g}(\mathbf{x}_{k-1}, \mathbf{u}_k)\mathbf{w}_k$, and $N(\mathbf{f}(\hat{\mathbf{x}}_{k-1}, \mathbf{u}_k), \mathbf{F}_k\mathbf{P}^{xx}_{k-1}\mathbf{F}^T_k)$ cannot guarantee over-bounding of the true distribution of $\mathbf{f}_k(\mathbf{x}_{k-1}, \mathbf{u}_k)$. We propose to over-bound those true distributions using Gaussian distributions with an inflated covariance matrix. While in general the over-bounding pdfs do not have to be Gaussian, we prefer to use Gaussian distributions for several reasons. First, Gaussian distributions can approximate many actual distributions encountered in practice, especially those encountered in physical systems. Second, Gaussian distributions are tractable mathematically. More precisely, the linear combination of Gaussian distribution is still Gaussian. This approach to over-bounding is, therefore, known as Gaussian over-bounding.

Due to this simplicity and our interest in real-time implementation of over-bounding in sensor fusion algorithms, this thesis focuses on the Gaussian over-bounding. An added benefit of this is that this over-bounding approach can fit smoothly into the real-time Kalman filter structure. This means that only the first and second order moments (although inflated ones) need to be saved and propagated. If a non-Gaussian over-bounding pdf is used, the requirements to maintain and propagate the whole pdf can be very difficult.

4.2 INS Problem Description

For clarity, and without a loss of generality, we will anchor our discussions to a two-dimensional (2D) aided-INS problem. It is a simple problem that allows getting an insight into the filtering problem easily while, at the same time, is of significant practical interest (e.g. automotive navigation). The simplified 2-D aided-INS problem is depicted in Figure 4.1. The vehicle is assumed to be traveling in a locally level plane with an Inertial Measurement Unit (IMU) comprised of two accelerometers and one rate gyro. If no adding is present, the INS navigation solution will drift due to initial position errors, initial velocity errors, initial heading error, and inertial sensor biases.

The navigation state vector for this problem has eight states which are two position coordinates (p_n and p_e), two velocity coordinates (v_n and v_e), heading (ψ), two accelerometer biases (b_{f_x} and b_{f_y}), and one rate gyro bias (b_ω). That is,

$$\mathbf{x} = [p_n \;\; p_e \;\; v_n \;\; v_e \;\; \psi \;\; b_{f_x} \;\; b_{f_y} \;\; b_\omega]^T. \tag{4.5}$$

The 'control' input u is as follows:

$$\mathbf{u} = [f_x \;\; f_y \;\; \omega]^T. \tag{4.6}$$

where f_x, f_y and ω are the two accelerometer and gyro measurements of specific force and rotation rate, respectively. These measurements are made in the body frame and are corrupted by sensor output noise, w, given by

$$\mathbf{w} = [w_{f_x} \;\; w_{f_y} \;\; w_\omega]^T. \tag{4.7}$$

The noises are the sources of uncertainty in the INS state propagation model.

For this 2-D INS, the mechanization equations are given by:

$$\dot{p}_n = v_n. \tag{4.8}$$

$$\dot{p}_e = v_e. \tag{4.9}$$

$$\dot{v}_n = (f_x - b_{f_x})\cos(\psi) - (f_y - b_{f_y})\sin(\psi) + \cos(\psi)w_{f_x} - \sin(\psi)w_{f_y}. \tag{4.10}$$

$$\dot{v}_e = (f_x - b_{f_x})\sin(\psi) + (f_y - b_{f_y})\cos(\psi) + \sin(\psi)w_{f_x} + \cos(\psi)w_{f_y}. \tag{4.11}$$

$$\dot{\psi} = \omega - b_\omega + w_\omega. \tag{4.12}$$

Consistent with our discussion in Chapter 3, the accelerometer and gyro biases are modeled stochastically as first-order Gauss-Markov process [18]:

$$\dot{b} = -\frac{1}{\tau_b} b + w_b. \tag{4.13}$$

In this equation b stands for b_{f_x}, b_{f_y} and b_ω where w_b stands for the driving noise of the first-order Gauss-Markov process model.

While our final goal is to over-bound the navigation solution $p(x_i)$ which is the output of an estimator (e.g. EKF) for state x_i, our first step is to over-bound the INS solution. Since usually the sampling frequency of IMU sensors is much higher than the plant dynamics bandwidth and the IMU sensor output noise can be well modeled as a white noise sequence (band limited white noise),

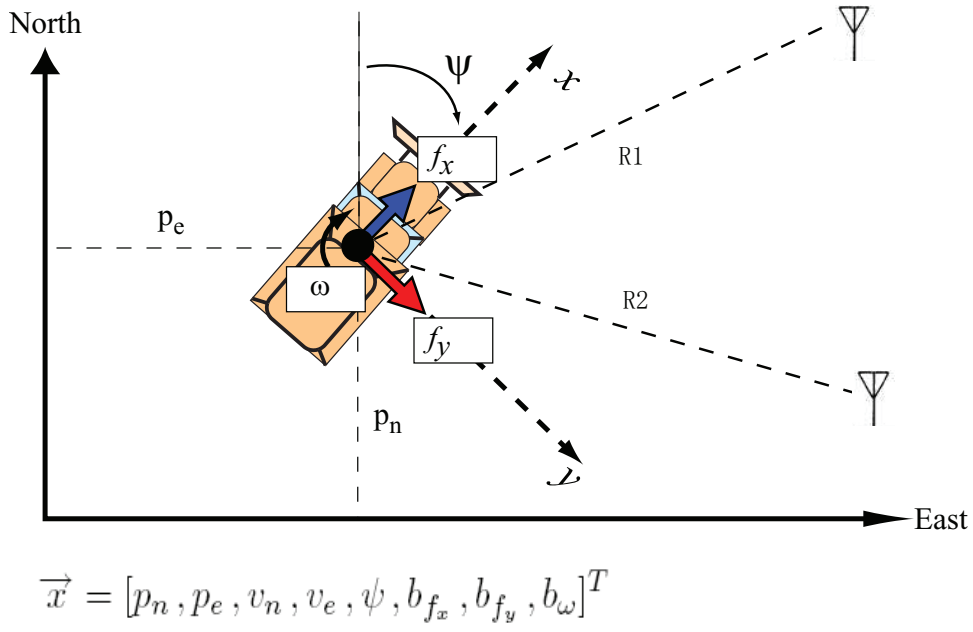

Figure 4.1: 2-D GNSS/INS Example.

we can discretize the continuous model using an Euler integration scheme as follows:

$$p_n(k) = p_n(k-1) + v_n(k-1)T_s. \tag{4.14}$$

$$p_e(k) = p_e(k-1) + v_e(k-1)T_s. \tag{4.15}$$

$$\begin{aligned} v_n(k) = {} & v_n(k-1) + (f_x(k-1) - b_{f_x}(k-1))\cos(\psi(k-1))T_s \\ & -(f_y(k-1) - b_{f_y}(k-1))\sin(\psi(k-1))T_s \\ & +\cos(\psi(k-1))T_s w_{f_x}(k-1) - \sin(\psi(k-1))T_s w_{f_y}(k-1). \end{aligned} \tag{4.16}$$

$$\begin{aligned} v_e(k) = {} & v_e(k-1) + (f_x(k-1) - b_{f_x}(k-1))\sin(\psi(k-1))T_s \\ & +(f_y(k-1) - b_{f_y}(k-1))\cos(\psi(k-1))T_s \\ & +\sin(\psi(k-1))T_s w_{f_x}(k-1) + \cos(\psi(k-1))T_s w_{f_y}(k-1). \end{aligned} \tag{4.17}$$

$$\psi(k) = \psi(k-1) + (\omega(k-1) - b_\omega(k-1))T_s + T_s w_\omega(k-1). \tag{4.18}$$

If we compare Equations 4.14 – 4.18 with Equation 4.1, we can identify $\mathbf{f}_k(\mathbf{x}_{k-1})$ and $\mathbf{g}(\mathbf{x}_{k-1})\mathbf{w}_k$ terms accordingly. In next section it will be shown that the EKF Gaussian approximations $N(\mathbf{f}(\hat{\mathbf{x}}_{k-1}), \mathbf{F}_k \mathbf{P}^{xx}_{k-1} \mathbf{F}^T_k)$ cannot guarantee over-bounding of the true distribution of $\mathbf{f}_k(\mathbf{x}_{k-1})$, and

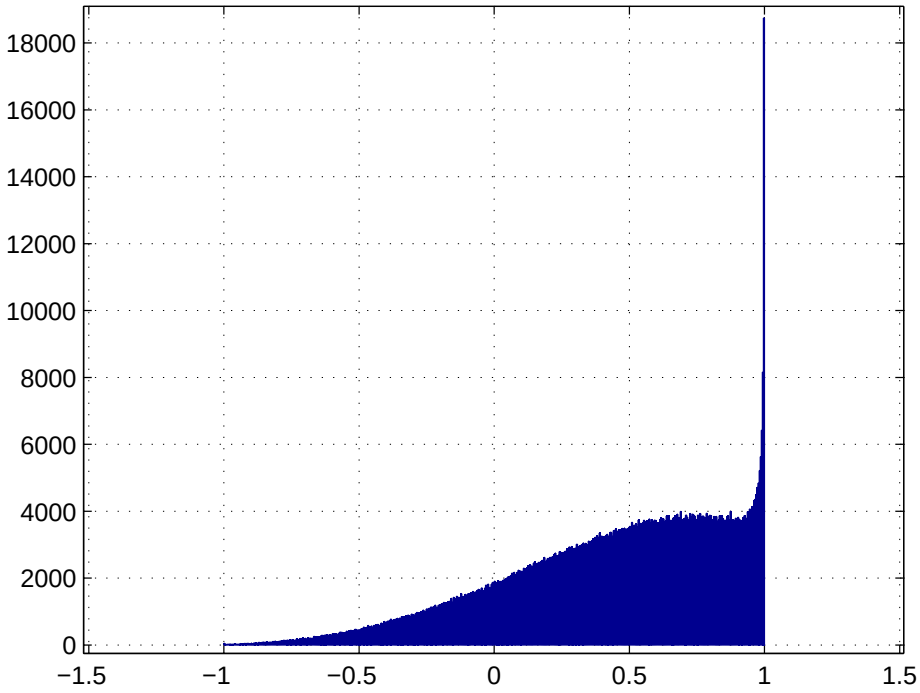

Figure 4.2: Histogram of $\cos(\psi)$ with $\psi \sim N(\pi/3, (\pi/6)^2)$.

$N(0, \mathbf{g}(\hat{\mathbf{x}}_{k-1})\mathbf{Q}_k\mathbf{g}(\hat{\mathbf{x}}_{k-1})^T)$ cannot guarantee over-bounding of the true distribution of $\mathbf{g}(\mathbf{x}_{k-1})\mathbf{w}_k$. It will also show the proof that those true distributions can be over-bounded by Gaussian distributions with inflated variance.

4.3 Over-bounding of INS Velocity Channel

To over-bound $\mathbf{x}$, we must show that errors introduced by the coordinate transformation and process noise are bounded. We will start by considering the coordinate transformation first.

4.3.1 Over-bounding Coordinate Transformation

In Equations 4.16 and 4.17, the nonlinear state propagation include nonlinear transformation terms $\cos(\psi)$ and $\sin(\psi)$ where ψ is the state variable heading. If ψ is random with mean $\hat{\psi}$ and standard deviation σ_ψ, then the EKF approximated Gaussian distribution for $\cos(\psi)$ will be

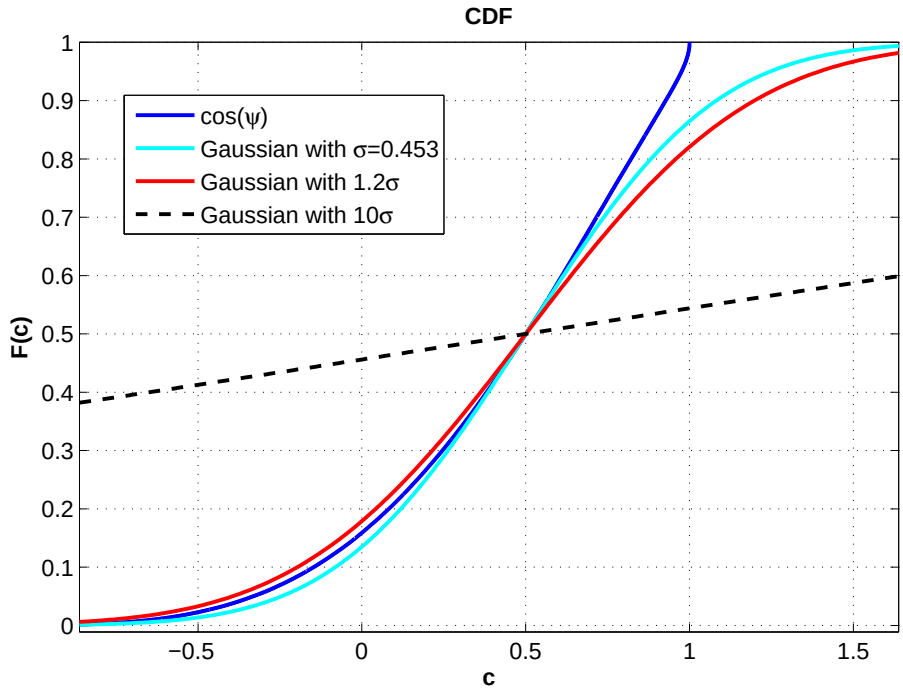

Figure 4.3: CDF Over-bounding of $\cos(\psi)$.

$N(\cos(\hat{\psi}), \sin^2(\hat{\psi})\sigma_\psi^2)$. This EKF approximated Gaussian distribution cannot guarantee over-bounding of the true distribution of $\cos(\psi)$. First let us consider an example to show this followed by a formal proof to show that the true distribution can be over-bounded by a Gaussian distribution with inflated variance.

Consider over-bounding $c = \cos(\psi)$ assuming $\psi \sim N(\pi/3, (\pi/6)^2)$. An empirical pdf of $\cos(\psi)$ obtained using the Monte Carlo method ($1,000,000$ samples) is shown in Figure 4.2. The EKF approximated Gaussian distribution has a variance $Var(\cos(\psi)) = \sin^2(\pi/3)(\pi/6)^2 = 0.453^2$. Figure 4.3 compares the true CDF $F(c)$ of $c = \cos(\psi)$ with this EKF approximated Gaussian distribution and shows that the true distribution of $\cos(\psi)$ is not over-bounded by this EKF approximated Gaussian distribution on the whole range of $\cos(\psi)$. For example, when $\cos(\psi)$ is between $[-1, 0]$, the EKF approximated Gaussian distribution loses over-bounding. Figure 4.3 also shows, however, that the true distribution of $\cos(\psi)$ can be over-bounded by a Gaussian distribution with inflated standard distribution (inflation factor $K_\psi >= 1.2$ for this example). Next a rigorous proof will be given.

We want to rigorously prove that the distribution of $\cos(\psi)$ can be over-bounded by a Gaussian distribution. We will start by proving a more general theorem.

Theorem 1:

Suppose c is a random variable (RV) with finite support in the range [-1 +1], median m_c, and $F(c)$ is the CDF of c. If $F(c)$ is an monotonically increasing function of c, then the RV c can be over-bounded in the CDF sense by inflating the variance σ^2 of a Gaussian distribution with median m_c.

Proof:

Let $\Phi(c)$ be the over-bounding CDF of a Gaussian distribution with variance σ^2 and mean m_c. We know that $F(-1) = 0, F(m_c) = 0.5, F(1) = 1$ and $\Phi(m_c) = 0.5$.

If choose an arbitrary small ε, we know $F(c) < 0.5, c \in [-1, m_c - \varepsilon]$. For any fixed $F(c) < 0.5$, we can find a σ^2 such that $\Phi(c) \geq F(c)$, since $\Phi(c)$ goes to 0.5 when σ goes to infinity. So we define

$$\sigma_1^2 = min\{\sigma^2 | \Phi(c;\sigma^2) \geq F(c), c \in [-1, m_c - \varepsilon]\} \tag{4.19}$$

σ_1^2 is the smallest σ^2 that satisfies $\Phi(c) \geq F(c)$ for all $c \in [-1, m_c - \varepsilon]$. Similarly, we can define

$$\sigma_2^2 = min\{\sigma^2 | \Phi(c;\sigma^2) \leq F(c), c \in [m_c + \varepsilon, 1]\} \tag{4.20}$$

σ_2^2 is the smallest σ^2 that satisfies $\Psi(c) \leq F(c)$ for all $c \in [m_c + \varepsilon, 1]$. So if we choose σ^2 to be $\max\{\sigma_1^2, \sigma_2^2\}$, we find the Gaussian distribution which can over-bound $F(c)$. This proof also offers a procedure to find this gaussian distribution. It needs to be noted that the over-bounding for $c \in [m_c - \varepsilon, m_c + \varepsilon]$ is undefined. However, it is not of practical concern since we can choose an arbitrary small ε.

The practical implication for this theorem is that the true distribution of $\cos(\psi)$ can be over-bounded by a Gaussian distribution with inflating the EKF approximate standard deviation with a factor K_ψ whose value can be determined by CDF over-bounding.

4.3.2 Over-bounding of Non-Gaussian Process Noise

In INS propagation Equations 4.16 and 4.17, the process noises includes terms having the format of $\cos(\psi)w$ or $\sin(\psi)w$, where ψ is the heading and w is the inertial sensor noise. It is shown that the distribution of the inertial sensor noise (w_ω, w_{f_x} etc.) is well approximated and over-bounded by Gaussian distribution in Figure 4.4. The blue line is the empirical CDF constructed from the real

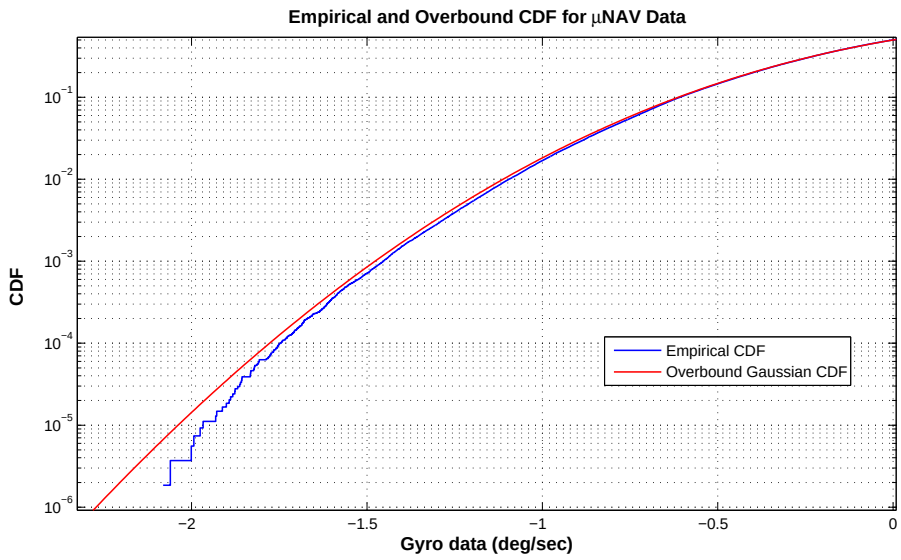

Figure 4.4: Example Showing Over-bounding of μNAV gyro data CDF .

data collected from Crossbow μNav [2], and the red line is the over-bounding CDF using Gaussian distribution.

However, the noise term $\cos(\psi)w$ is generally non-Gaussian even if w is Gaussian. Furthermore, the EKF approximate distribution $N(0, \sin^2(\hat{\psi})\sigma_w^2)$ does not over-bound the true distribution of $\cos(\psi)w$. This can be seen by considering the following example: Let $w \sim N(0,1)$, $\psi \sim N(\pi/3, (\pi/6)^2)$. The true pdf of $\cos(\psi)w$ is obtained using Monte Carlo method by drawing 1×10^6 samples and is plotted in Figure 4.5. The CDF of $\cos(\psi)w$ is shown in Figure 4.6 as the blue line.

The EKF approximated Gaussian distribution is $N(0, \cos^2(\pi/3)\sigma_w^2) = N(0, 0.5^2)$. Figure 4.6 compares the true CDF of $\cos(\psi)w$ with this EKF approximate Gaussian distribution and shows that the true distribution of $\cos(\psi)w$ is not over-bounded by this EKF approximate Gaussian distribution. It is also shown in Figure 4.6 that the true distribution of $\cos(\psi)w$ is over-bounded by a Gaussian distribution with inflated standard deviation (inflation factor $K_w = 1.9$ for this example). Next a rigorous proof will be given.

Theorem 2:

Suppose w is a RV with symmetric distribution and zero mean, ψ is a random variable with arbitrary

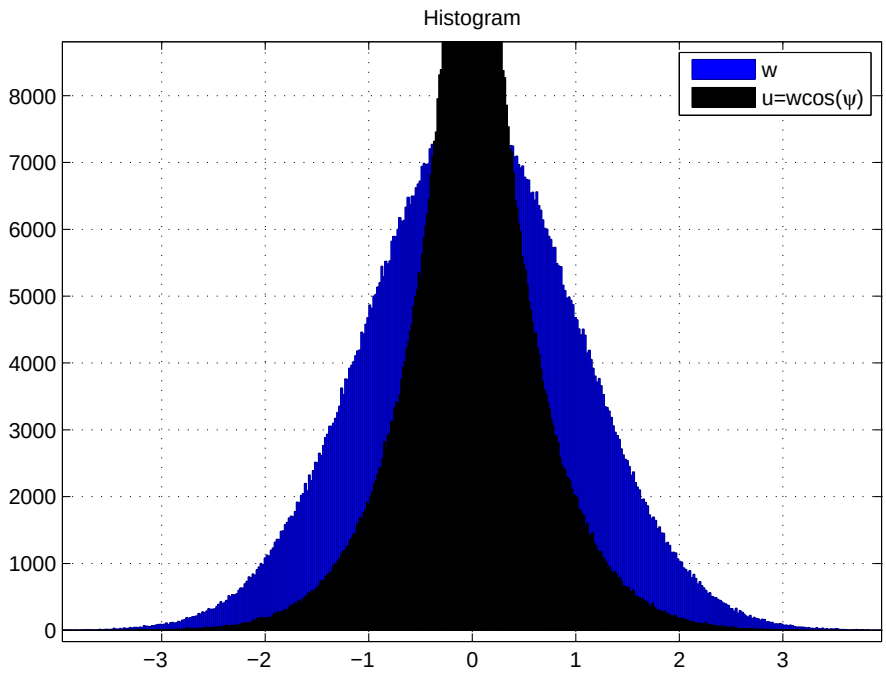

Figure 4.5: Histogram of $w\cos(\psi)$.

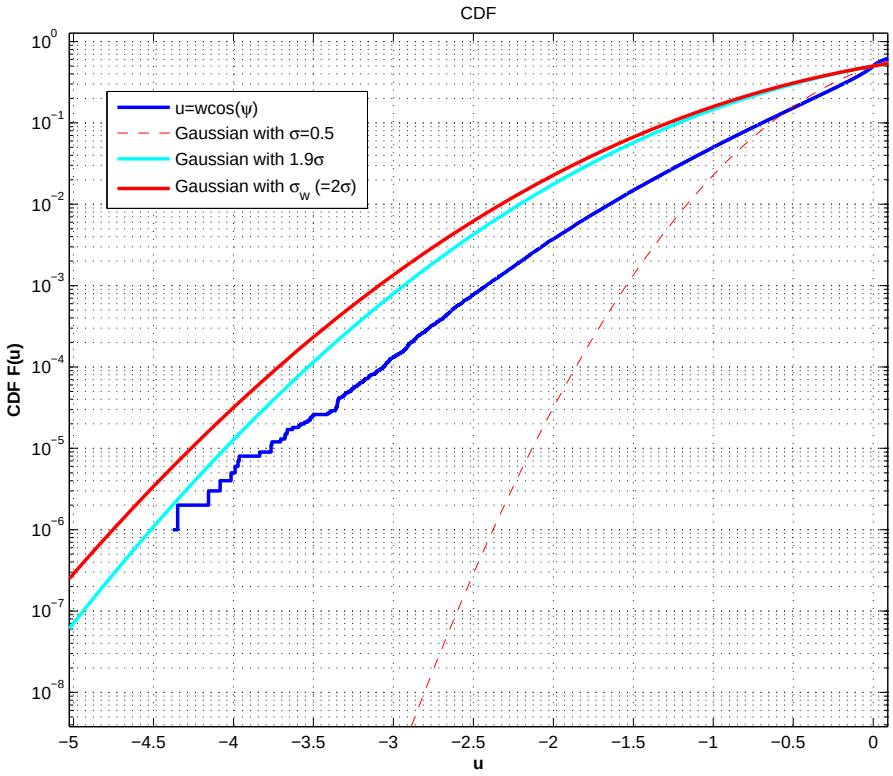

Figure 4.6: CDF over-bounding of $w\cos(\psi)$.

distribution, and w and ψ are independent. Then the RV $u = w\cos(\psi)$ can be over-bounded in CDF sense by the distribution of w. That is, if w can be over-bounded in CDF sense by a Gaussian random variance $w^o \sim N(0, \sigma^2_{w^o})$, then $w\cos(\psi)$ is over-bounded by $w^o \sim N(0, \sigma^2_{w^o})$.

Proof:

We define $c = \cos(\psi)$, so the pdf of c will have finite support [-1,1]. We assume the CDF of c has no jump at point 0 so that $P_r(c = 0) = 0$ where $P_r(c = 0)$ means the probability that $x = 0$. For arbitrary $u_0 > 0$,

$$\begin{aligned} P_r(u > u_0) &= P_r(wc > u_0) \\ &= P_r(w > \frac{u_0}{c}, c > 0) + P_r(w < \frac{u_0}{c}, c < 0) \\ &\leq P_r(w > u_0, c > 0) + P_r(w < -u_0, c < 0) \\ &= P_r(w > u_0)P_r(c > 0) + P_r(w < -u_0)P_r(c < 0) \\ &= P_r(w > u_0)[P_r(c > 0) + P_r(c < 0)] \\ &= P_r(w > u_0) \end{aligned} \tag{4.21}$$

Thus, we have proved that

$$Pr(u > u_0) \leq P_r(w > u_0), \forall u_0 > 0 \tag{4.22}$$

Similarly it can be proved that

$$Pr(u < u_0) \leq P_r(w < u_0), \forall u_0 < 0 \tag{4.23}$$

So u can be over-bounded by w in CDF sense.

If w can be over-bounded in CDF sense by a Gaussian random variance w^o, by definition of CDF over-bounding we have

$$Pr(u > u_0) \leq P_r(w > u_0) \leq P_r(w^o > u_0), \forall u_0 > 0 \tag{4.24}$$

and

$$Pr(u < u_0) \leq P_r(w < u_0) \leq P_r(w^o < u_0), \forall u_0 < 0 \tag{4.25}$$

So $u = wcos(\psi)$ is over-bounded by $w^o \sim N(0, \sigma^2_{w^o})$.

Heading error σ_ψ (deg)	30	20	10	5
Inflating scale K_w	1.9	1.7	1.4	1.15

Table 4.1: Inflating scale dependent on the heading error σ_ψ.

It has to be pointed out that this does not mean that w^o is the tightest bound. This just states that w^o is guaranteed to be one over-bound. It is possible to find an over-bounding distribution with a smaller standard deviation than σ_{w^o}. In general a over-bounding distribution will have the form

$$N(0,(K_w \sin(\hat{\psi})\sigma_{w^o})^2), K_w \in [1, 1/\sin(\hat{\psi})]. \tag{4.26}$$

For the previous example, Table 4.1 shows the inflating scale K_w for different heading error σ_ψ. For this example $K_w \in [1,2]$.

4.3.3 Over-bounding Open-loop INS Velocity Channel

In this section we apply Monte Carlo simulation to find the true distribution propagation for the stochastic model Equations 4.14 to 4.18. The initial heading error (standard deviation) is set to be 15 degree. The true distributions for north velocity at time 1, 2 and 3 seconds are shown in Figures 4.7 as blue lines. The EKF approximated distributions are shown in the same figure as red lines. It can be seen that the true north velocity error CDF is not over-bounded by a EKF predicted Gaussian distribution. With the propagation time increasing, the loss of over-bounding situation is more severe.

Figures **??** shows the over-bounding Gaussian distributions which are obtained by inflating the standard deviation of previous EKF predicted Gaussian distributions. The blue lines are the true CDF from the Monte Carlo simulation, and the red lines are over-bounding Gaussian distributions. Here by trial and error the EKF approximated standard deviation of the process noises in Equations 4.16 and 4.17 are inflated by $K_w = 1.5$ and the EKF approximate standard deviation of $cos(\psi)$ and $sin(\psi)$ are inflated by $K_\psi = 1.6$. It can be seen that the inflated Gaussian distribution can over-bound the true distribution at time 1, 2 and 3 seconds.

It is not uncommon to inflate the process noise to tune the EKF in practice, so we need to point out the difference between that method and the method proposed here. First, we proved that the non-Gaussian process noises terms $\cos(\psi)w$ or $\sin(\psi)w$ can be over-bounded by w, which set a upper

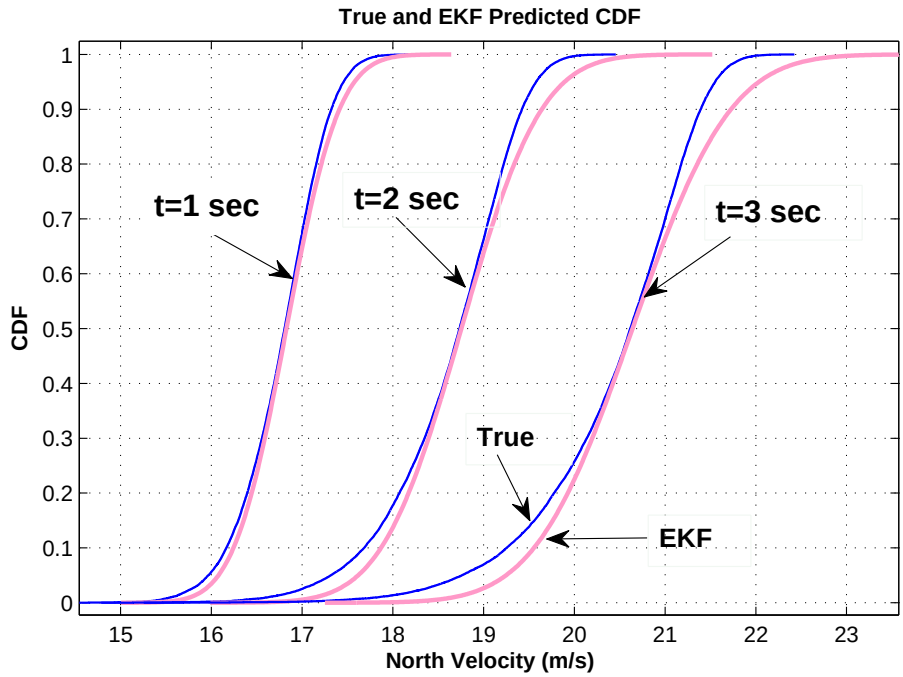

Figure 4.7: Monte Carlo and EKF predicted CDF for north velocity.

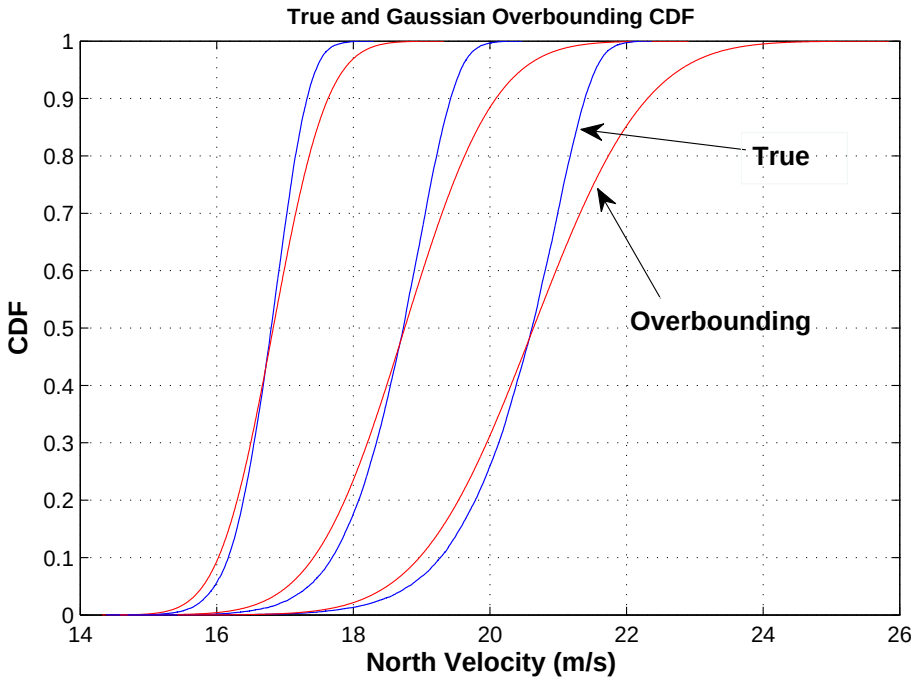

Figure 4.8: Monte Carlo and Gaussian Over-bounding CDF for north velocity.

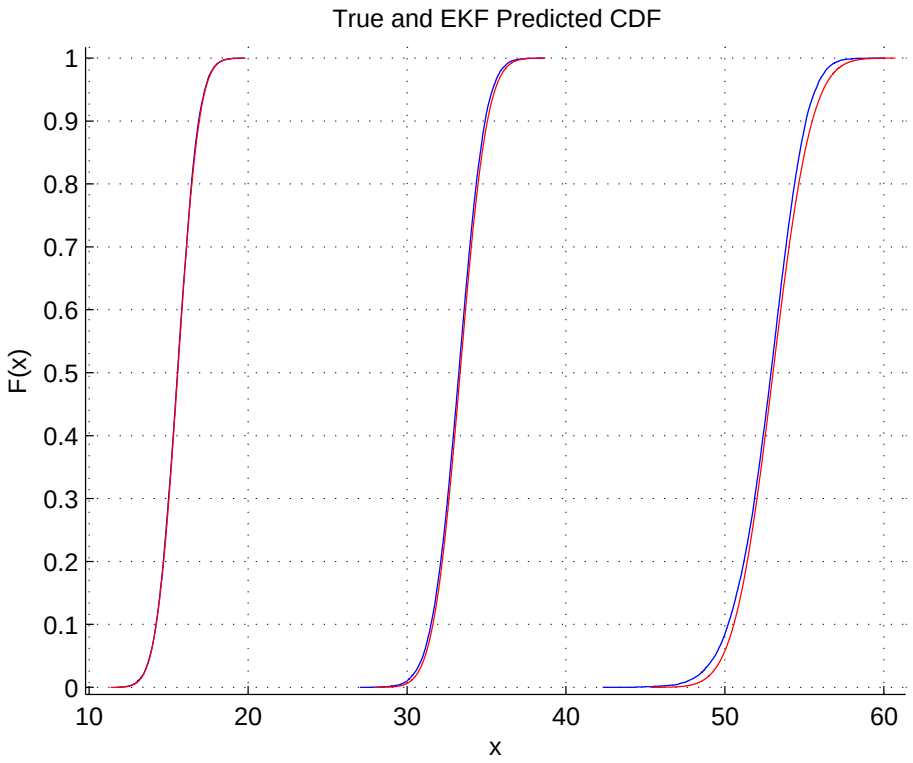

Figure 4.9: Monte Carlo and EKF predicted CDF for north position.

limit needed to inflate the process noises. All other non-Gaussian effects come from the nonlinear transformation and especially nonlinear coordinate transformation. To compensate for these non-Gaussian effects we can inflate $\cos(\psi)$ and $\sin(\psi)$ terms directly. By doing so it is possible to have tight over-bounding than by inflating the process noises alone.

4.4 Over-bounding of INS Position Channel

Figures 4.9 shows the true north position error CDF (blue lines) and the EKF predicted Gaussian distribution (red lines). Compared with north velocity plots, the true north position error CDF and the EKF predicted Gaussian distribution are closer. However, with the propagation time increasing, the loss of the over-bounding situation is clear.

Figures 4.10 show the true north position error CDF (blue lines) and the over-bounding Gaussian distributions (red lines). We need to point out that there is no direct inflation of the EKF

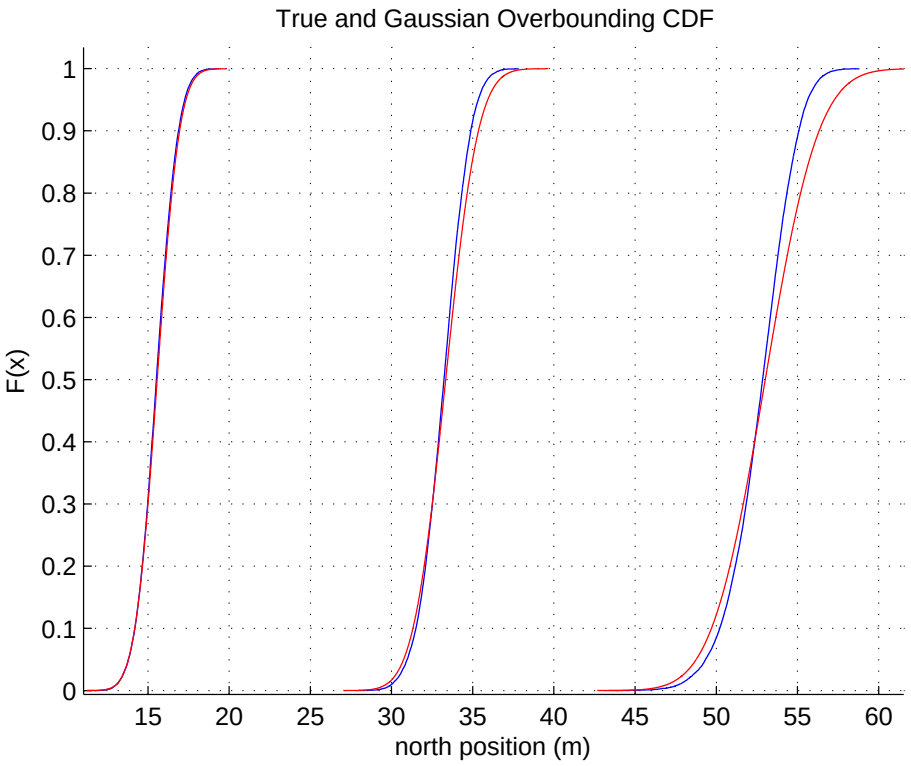

Figure 4.10: Monte Carlo and Gaussian Over-bounding CDF for north position.

predicted position error. The inflation effect of the position state error in Equations 4.14 and 4.15 come from inflated $v_n(k-1)$ and $v_e(k-1)$.

4.5 Over-bounding INS/GNSS Integration Output

4.5.1 INS/GNSS system with GNSS periodic reset

If an INS works alone for a short time with GNSS resetting the initial positions and/or velocities periodically, then the over-bounding of GNSS output error and the over-bounding of INS propagation over-bounding are decoupled. Previous over-bounding methods for finding over-bounds in position domain by over-bounding the errors in pseudorange domain can be applied to GNSS. The methods proposed in this chapter can be applied to INS propagation.

4.5.2 INS/GNSS loose integration with EKF

Here we adopt the naming convention used in [5], where $\hat{\mathbf{x}}_k(-)$ means the estimate of the state vector at time k before the measurement is incorporated, $\hat{\mathbf{x}}_k(+)$ means the estimate of the state vector at time k after the measurement is incorporated and tilde means estimation error. Thus we have

$$\hat{\mathbf{x}}_k(-) = \mathbf{x}_k + \tilde{\mathbf{x}}_k(-) \tag{4.27}$$

$$\hat{\mathbf{x}}_k(+) = \mathbf{x}_k + \tilde{\mathbf{x}}_k(+) \tag{4.28}$$

We first consider the situation that we have a linear measurement model $\mathbf{z}_k = \mathbf{H}_k\mathbf{x}_k + \mathbf{v}_k$. If we assume the estimator takes the prediction-correction form

$$\hat{\mathbf{x}}_k(+) = \hat{\mathbf{x}}_k(-) + \mathbf{K}_k[\mathbf{z}_k - \mathbf{H}_k\hat{\mathbf{x}}_k(-)]. \tag{4.29}$$

Then the estimate error will have the form

$$\tilde{\mathbf{x}}_k(+) = (\mathbf{I} - \mathbf{K}_k\mathbf{H}_k)\tilde{\mathbf{x}}_k(-) + \mathbf{K}_k\mathbf{v}_k. \tag{4.30}$$

So if we can over-bound the predicted error $\tilde{\mathbf{x}}_k(-)$ (which is INS output error in aided INS problem) and the measurement error $\mathbf{v}_k$, it is possible to over-bound the corrected (filtered) error $\tilde{\mathbf{x}}_k(+)$. However, the correlation between these states need to be considered.

To make the problem tractable, we start from a one-dimension (single variable) problem. In this situation, x_k is a random variable, then $\tilde{x}_k(+)$ has a format of

$$\tilde{x}_k(+) = (1 - KH)\tilde{x}_k(-) + Kv_k \tag{4.31}$$

If we assume $\tilde{x}_k(-)$ and v_k are independent, and

$$N(x; 0, P_k^{xx}(-)) \succ p_{\tilde{x}_k(-)}(x) \tag{4.32}$$

$$N(v; 0, R_k) \succ p_v(v) \tag{4.33}$$

then

$$N(x; 0, P_k^{xx}(+)) \succ p_{\tilde{x}_k(+)}(x) \tag{4.34}$$

where

$$P_k^{xx}(+) = (1 - KH)^2 P_k^{xx}(-) + K^2 R_k \tag{4.35}$$

It needs to be pointed out that when updating the covariance, the above equation should be used rather than the simpler one $P_k^{xx}(+) = (1-KH)P_k^{xx}(-)$, because the Kalman gain used here is not necessarily optimal.

If $\mathbf{x}_k$ is a vector other than a single random variable, the distribution of $\tilde{\mathbf{x}}_k(+)$ will be multi-dimensional. Let us look at the marginal pdf of its one element, say, $\mathbf{x}_k(i)$,

$$x_k(i) = \mathbf{a}_1 \tilde{\mathbf{x}}_k(-) + \mathbf{b}_1 \mathbf{v}_k \tag{4.36}$$

where $\mathbf{a}_1$ is the first row of matrix $(\mathbf{I} - \mathbf{K}_k\mathbf{H}_k)$ and $\mathbf{b}_1$ is the first row of matrix $\mathbf{K}_k$. So we are faced with over-bounding a linear combination of correlated input random variables $\tilde{\mathbf{x}}_k(-)$ which may not share pdfs of the same form. Further work is needed to over-bound this.

Chapter 5

Simulation and Experimental Results

In this chapter two examples are given to show how the stochastic inertial sensor error modeling explained in Chapter 3 and a Gaussian over-bounding proposed in Chapter 4 can be used to over-bound the output errors of integrated inertial navigation systems.

5.1 UGV Dead Reckoning System Error Bounding

The purpose of this example is to show the application of inertial sensor error modeling in bounding Unmanned Ground Vehicle (UGV) navigation system output errors. As a case study, let us consider the automotive guidance and control problem discussed in Chapter 1 and depicted again here in Figure 5.1. As shown in the block diagram in Figure 5.1, the navigation state $\mathbf{x}$ is estimated in real time by fusing the outputs y_i (where $i = 1, 2, \ldots, N$) of many sensors. The dynamic model for this problem has three states. These states are the lateral position (x), the heading angle (ψ) and the distance traveled along track (s). Mathematically, this dynamic model is written as:

$$\dot{\mathbf{x}} = \begin{bmatrix} \dot{s} \\ \dot{x} \\ \dot{\psi} \end{bmatrix} = \mathbf{f}(\mathbf{x}) = \begin{bmatrix} V\cos(\psi) \\ V\sin(\psi) \\ r \end{bmatrix}. \tag{5.1}$$

Precisely or conservatively quantifying P_H requires error models for the sensors used in the navigation system. In this case, let us assume that the navigation system only uses two sensors; a Doppler radar for sensing speed and a rate gyro for sensing gyro rate. For simplicity and clarity, we

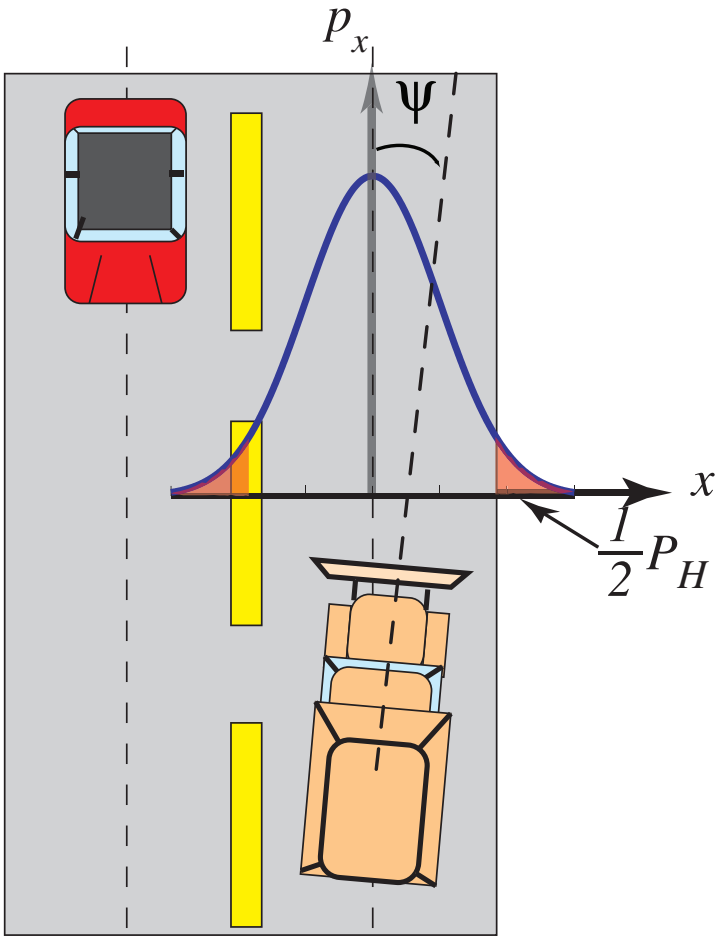

Figure 5.1: An Unmanned Ground Vehicle(Left) In Operation.

assume that the vehicle is heading north and uses an error-free Doppler radar measuring a constant speed of $V = 60$ km/hr, a reasonable speed for an automobile driving on a highway. The output of the rate gyros is r and is integrated to yield heading, ψ. As explained in Chapter 3, the rate gyros measurement r is corrupted by output errors. Here we assume that the constant bias b_0 has already been estimated and removed from the gyro outputs and we are interested in investigating the effect of stochastic residual errors of rate gyro outputs on the error growth of the heading ψ and the positions x and s.

As a benchmark or truth reference of the error growth of the heading and the positions, we perform a Monte Carlo analysis where we generate the heading and position trajectories for a two minute window using data collected from the Crossbow μNav Inertial Measurement Unit (IMU) [2] and the Microbotics MIDG II IMU [1]. The statistics of heading and position (i.e. standard deviation) of these two-minute runs represent the *true* error of the navigation system. We regard this *true* error as benchmark and will compare it later with the model predicted error from covariance analysis to investigate how well the error models are.

In Figure 5.2 the blue lines represent the two-minute heading error growth trajectories generated from two-minute windows of MIDG data. Each blue line represents a specific trajectory (one realization) of many possibilities. Although each trajectory seems to have some arbitrary trend (some may have an upward trend while some may have a downward trend) the *ensemble* of trajectories can be described only in a statistical way and not deterministic. That is, you cannot tell precisely which trajectory the heading error will take *in advance* but you know the behavior of the trajectories will have some known statistical characteristics. The red lines in Figure 5.2 show the standard deviation growth with time.

From the ensemble of trajectories (blue lines) and standard deviation of the trajectories (red lines) in Figure 5.2, we may observe that the behavior of the heading error looks similar to a random walk. This is equivalent to say that the error on the gyro output is white noise [41]. We are interested in investigating whether this is a good model and compare it with the model proposed in Chapter 3.

In Figure 5.3 the blue lines represent the two-minute position error growth trajectories and the red lines represent the standard deviation of position error as a function of time. The position error growth looks smoother than the heading error growth. This is because integration has the effect of a low-pass filter to smooth out the noise. While the heading error is an integral of gyro output noises

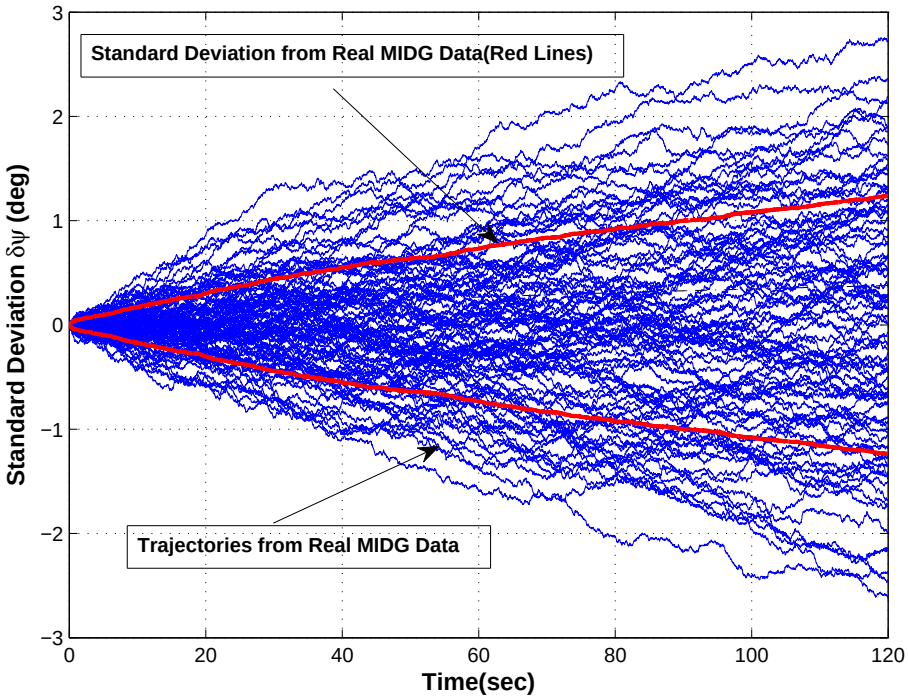

Figure 5.2: Heading Error Growth Using Actual MIDG Data.

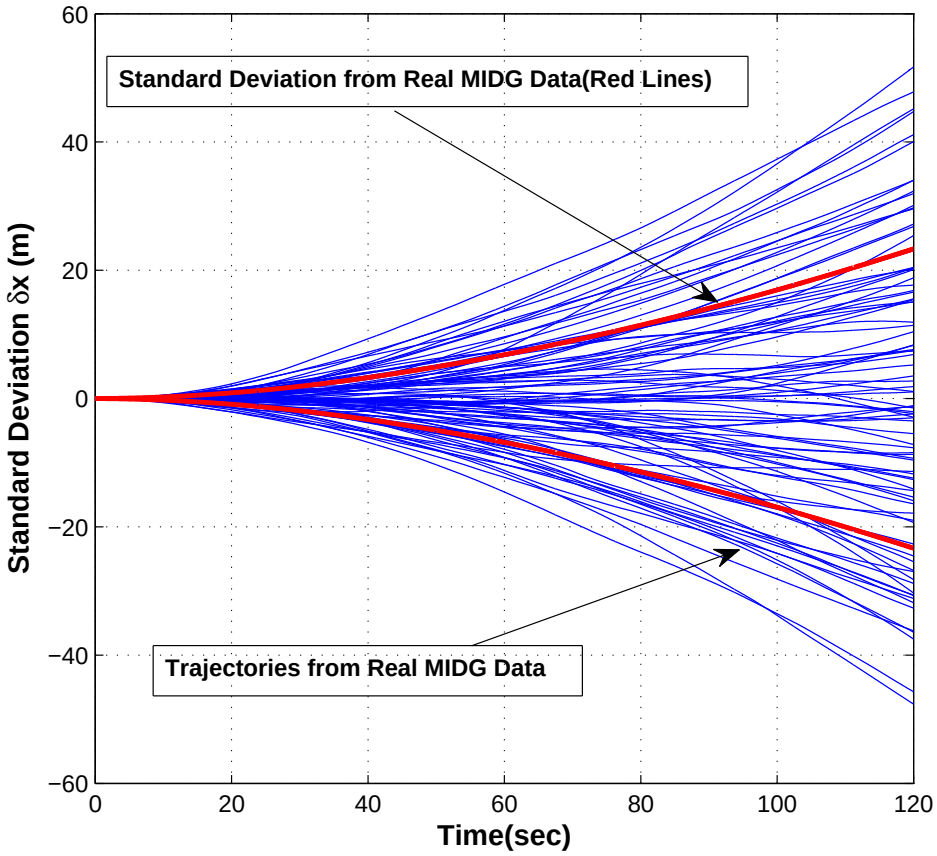

Figure 5.3: Heading Error Growth Using Actual MIDG Data.

the position error is an integral of heading error and so is double integral of gyro output error.

Next we examine how well we can predict the error bounds using the error models developed earlier in a covariance analysis. To perform a covariance analysis, we must linearize the nonlinear model given by Equation 5.1 and augment the state vector with the gyro bias, b_1, as follows:

$$\delta\mathbf{x} = \begin{bmatrix} \delta s \\ \delta x \\ \delta\psi \\ b_1 \end{bmatrix} \tag{5.2}$$

The equation that governs the propagation of the state errors in time is then given by:

$$\dot{\delta\mathbf{x}} = \mathbf{F}\delta\mathbf{x} + \mathbf{G}\mathbf{w} \tag{5.3}$$

where,

$$\mathbf{F} = = \begin{bmatrix} 0 & 0 & -\sin(\psi)V & 0 \\ 0 & 0 & \cos(\psi) & 0 \\ 0 & 0 & 0 & 1 \\ 0 & 0 & 0 & -\frac{1}{\tau} \end{bmatrix} \tag{5.4}$$

$$\mathbf{G} = \begin{bmatrix} 0 & 0 \\ 0 & 0 \\ 1 & 0 \\ 0 & 1 \end{bmatrix} \tag{5.5}$$

$$\mathbf{w} = \begin{bmatrix} b_w \\ w_{b_1} \end{bmatrix}. \tag{5.6}$$

Denoting the discrete equivalent of $\mathbf{F}$ as Φ, the covariance propagation for the navigation state errors will be governed by:

$$\mathbf{P}_k = \mathcal{E}\{\delta\mathbf{z}_k \delta\mathbf{z}_k^T\} \tag{5.7}$$

$$= \Phi_{k-1}\mathbf{P}_{k-1}\Phi_{k-1} + \Gamma_{k-1} \tag{5.8}$$

where Γ_{k-1} is the discrete equivalent of $\mathbf{G}\mathbf{Q}_w\mathbf{G}^T$ and $\mathbf{Q}_w$ is the power spectral density matrix of $\mathbf{w}$.

In what follows we perform a covariance analysis to compare the fidelity of the error estimates using the following two models: (1) A model consisting of white noise b_w only as proposed in [42] and (2) A model consisting of white noise b_w and correlated noise b_1 as developed in Chapter 3. We use data collected from the Crossbow μNav IMU [2] and the Microbotics MIDG II IMU [1]. The procedure to estimate the error model's parameters is discussed in Chapter 3. In Figure 5.4 the black line represents a model comprising three first-order Gauss Markov models with correlation times 10 seconds, 100 seconds and 500 seconds. While this approximated model is close to the data generated correlation function plot, it may be too complex to use in practical applications. So an over-bounding model is shown as red line in Figure 5.4 which has a correlation time of 280

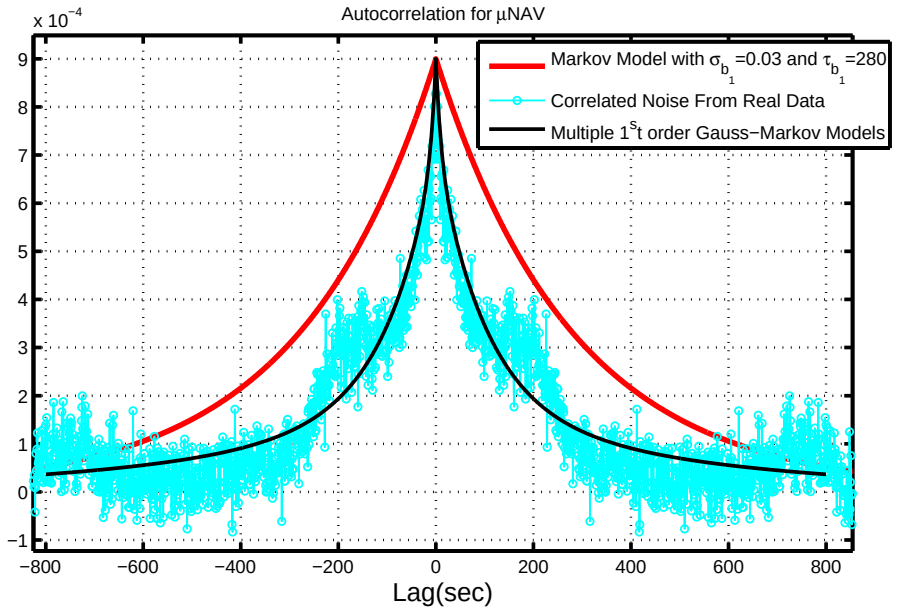

Figure 5.4: μNAV Over-bounding Procedure.

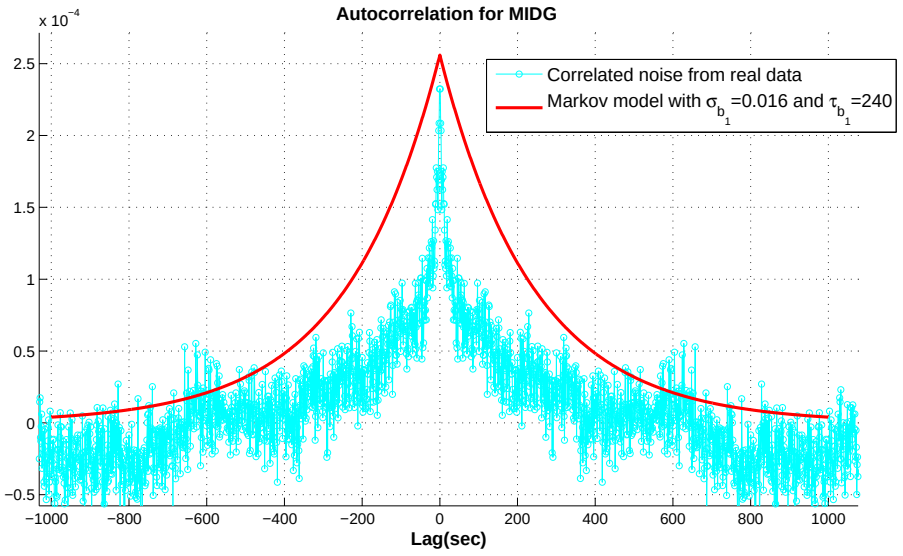

Figure 5.5: MIDG Over-bounding Procedure.

Models	b_w	$b_1(t)$	
	σ_{b_w}	τ_{b_1}	σ_{b_1}
μNAV 1	0.478 deg/sec	-	-
μNAV 2	0.478 deg/sec	280 sec	0.03 deg/sec
MIDG 1	0.244 deg/sec	-	-
MIDG 2	0.244 deg/sec	240 sec	0.016 deg/sec

Table 5.1: Parameters for Rate Gyro Output Error Models.

seconds. This can be regarded as a tradeoff between short-time correlated and long-time correlated processes which are inherent in the inertial sensor error process.

The autocorrelation over-bounding procedure for MIDG IMU data is shown in Figure 5.5. The over-bounding model, as a tradeoff, is a single Gaussian Markov process which has a correlation time of 240 seconds. The similarities between model parameters of μNav and MIDG may be due to that they belong to the same class of consumer grade IMUs. The resulting error models are summarized in Table 5.1.

The results of covariance analysis for the heading error and position error together with benchmark *true* error growth are shown in Figures 5.6 and 5.7. In Figure 5.6 the dashed black line is the white noise model (b_w) with PSD Q_w. The heading error is the result of the integration of white noise. The standard deviation of heading error σ_ψ as a function of time can be calculated as follows [41]:

$$\sigma_\psi^w = \sqrt{Q_w}\sqrt{t} \tag{5.9}$$

Clearly the white noise model with the original estimated PSD Q_w can not over-bound the true error growth. So a natural idea will be to inflate Q_w to over-bound the true error growth. This situation is shown in Figure 5.6. The dotted black line and solid black lines in Figure 5.6 show the results of inflating Q_w by a factor of 4 and 9, respectively. It can be seen that by inflating the PSD Q_w, the simple white noise model over-bounds the true heading error at the beginning. However, the ability to over-bound is lost after some time. This implies that the heading error grows with a rate faster than a square root function of time and the gyro error model should include other components

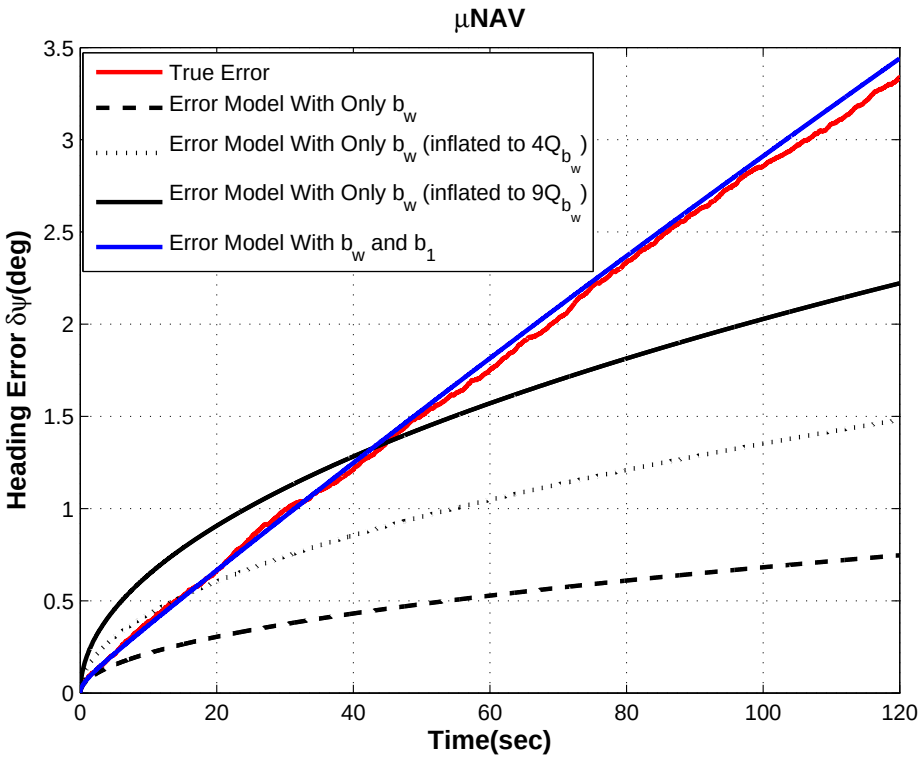

Figure 5.6: Navigation Simulation And Actual μNAV Data Comparison. Heading Errors.

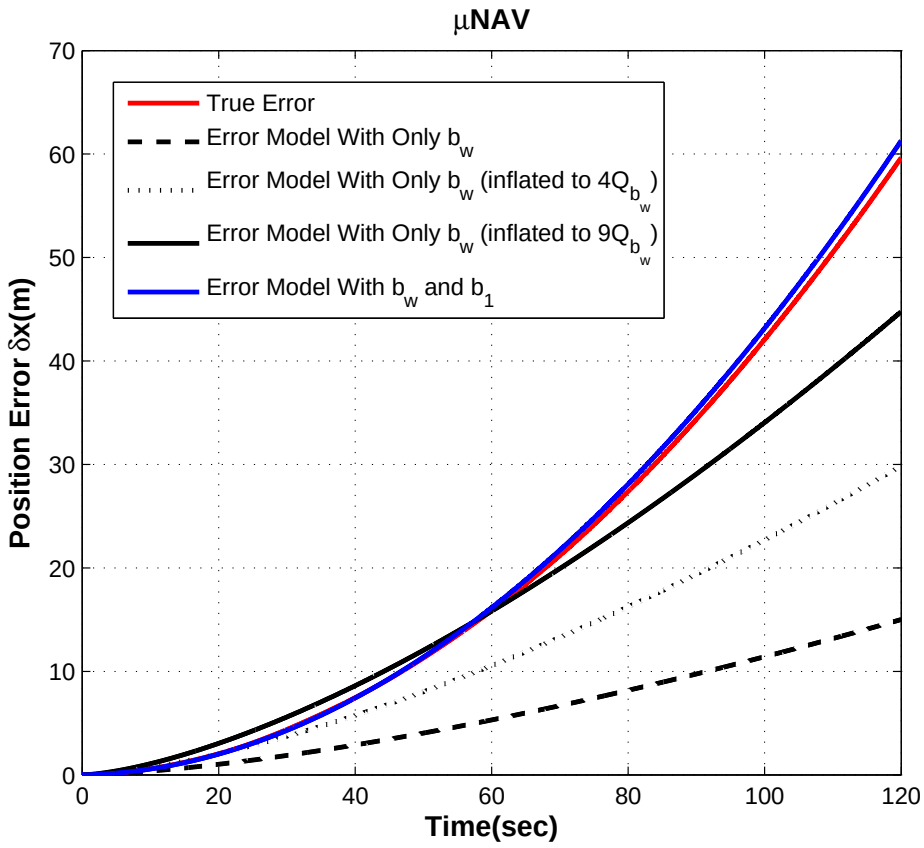

Figure 5.7: Navigation Simulation And Actual μNAV Data Comparison. Position (Cross Track) Errors.

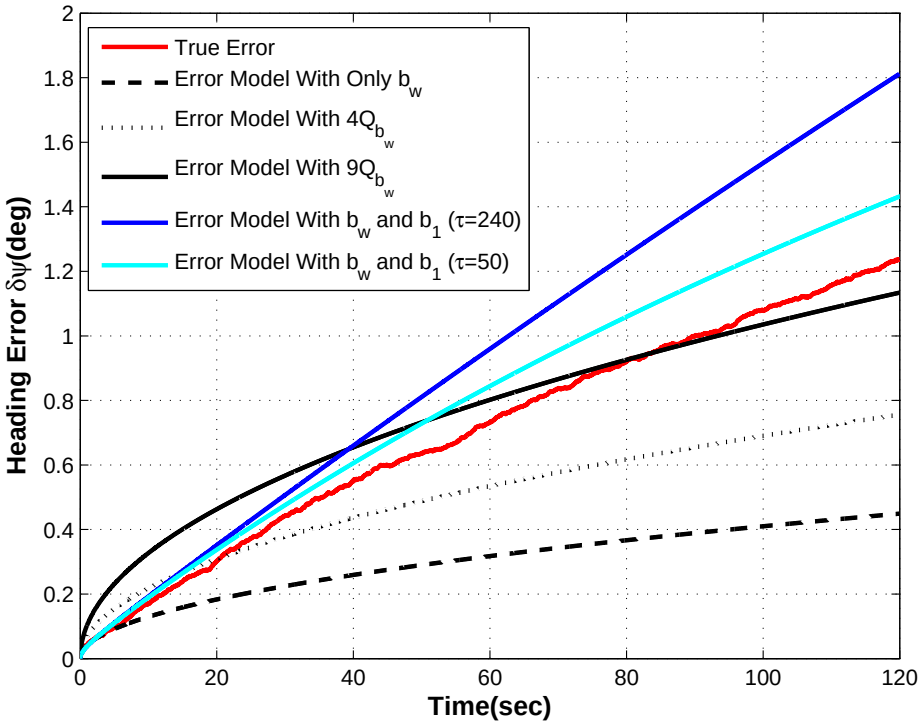

Figure 5.8: Navigation Simulation And Actual MIDG Data Comparison. Heading Errors.

besides the white noise if we are interested in over-bounding. In our model we propose using a 1^{st} order Gauss-Markov model with time constant τ_{b_1} and standard deviation σ_{b_1}. The standard deviation of heading error σ_ψ due to this 1^{st} order Gauss-Markov process is as follows [6]:

$$\sigma_\psi^{b_1} = \sqrt{2}\sigma_{b_1}\tau_{b_1}\sqrt{\frac{t}{\tau_{b_1}} + e^{-\frac{t}{\tau_{b_1}}} - 1} \tag{5.10}$$

If both the white noise b_w and correlated noise b_1 are included in the model whose parameters are shown in Table 5.1, the standard deviation of heading error σ_ψ due to both b_w and b_1 is as follows [6]:

$$\sigma_\psi^{total} = \sqrt{2}\sigma_{b_1}\tau_{b_1}\sqrt{\frac{t}{\tau_{b_1}} + e^{-\frac{t}{\tau_{b_1}}} - 1} + \sqrt{Q_w}\sqrt{t} \tag{5.11}$$

The result is shown as a blue line in Figure 5.6. It can be seen that this error model with both b_w and b_1 capture the behavior of the heading error growth quite well in a two-minute time period.

The results of covariance analysis for the heading error and position error for MIDG are shown

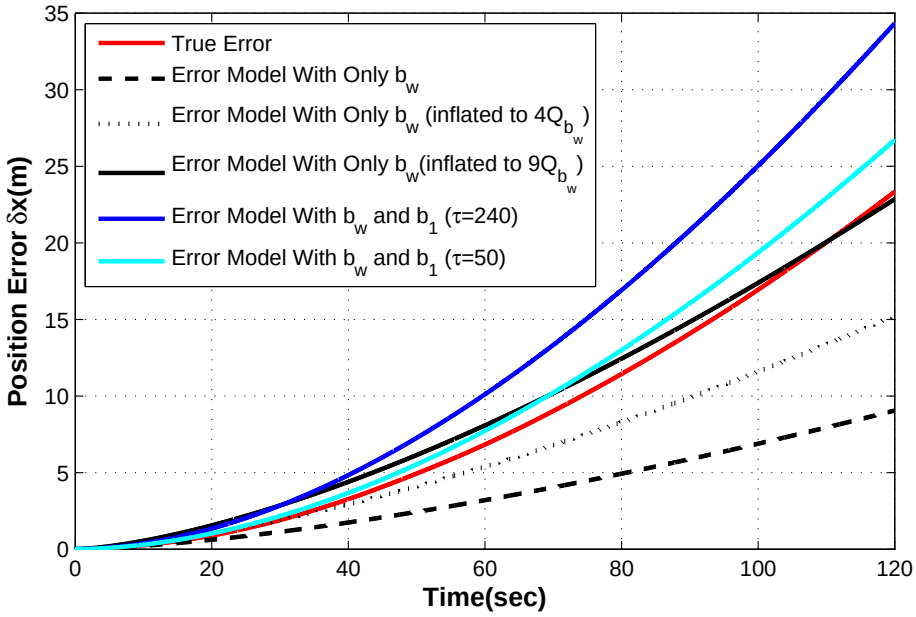

Figure 5.9: Navigation Simulation And Actual MIDG Data Comparison. Position (Cross Track) Errors.

in Figures 5.8 and 5.9. While over-bounding are obtained this time the over-bounding model with b_w and b_1 look too conservative. That is, the bounds are not the tightest bounds one can get. For example, if the b_1 time constant τ is decreased from 240 seconds to 50 seconds a tighter over-bound model results. This may be due to the fact that we are too conservative when estimating the b_1 parameters using an autocorrelation function.

In summary, we conclude that although the simple wide band noise model can bound the error in the first few seconds, it loses its bounding ability afterwards. If we add a first order Gauss-Markov model and tune parameters to account for the correlated part, we can bound the estimation error tightly in any time span we are interested. In turn, this means we can have an an conservative and accurate evaluation of the integrity risk P_H as shown in Equation 1.1.

5.2 Over-bounding EKF

The purpose of this example is to show the application of over-bounding in context of the Kalman Filtering. As case study let us consider a two-dimensional vehicle navigation problem. Similar to previous example, let us assume that the navigation system only uses two sensors- a Doppler radar for sensing speed and a rate gyro for sensing heading rate. However, in this example we assume that the speed sensor is not error-free but corrupted by noise. In the previous section it has been shown that by including correlated noise in the gyro error model we can over-bound the heading error growth. Since in this section we are interested in the effect of nonlinear coordinates transformations on the over-bounding of navigation state error growth, we will focus on the heading and positions and not include the gyro sensor bias model in the analysis. Here we assume the heading error has been over-bounded using methods explained in the previous section and look into the effect of the heading error on the error propagation of position. The dynamic model for this problem has three states. These states are the north position (x), the east position (y) and the heading angle (ψ). Mathematically, this dynamic model is written as:

$$\dot{\mathbf{x}} = \begin{bmatrix} \dot{x} \\ \dot{y} \\ \dot{\psi} \end{bmatrix} = \mathbf{f}(\mathbf{x},\mathbf{u}) + \mathbf{g}(\mathbf{x})\mathbf{w} = \begin{bmatrix} V\cos(\psi) \\ V\sin(\psi) \\ r \end{bmatrix} + \begin{bmatrix} \cos(\psi) & 0 \\ \sin(\psi) & 0 \\ 0 & 1 \end{bmatrix} \begin{bmatrix} w_v \\ w_v \end{bmatrix}. \tag{5.12}$$

where V is speed sensor measurement corrupted with noise w_v and r is gyro sensor measurement corrupted with noise w_r. Further in this example we assume that we have measurement of the positions x and y (e.g. using GPS) which are corrupted by noises $\mathbf{v}$.

$$\mathbf{z} = \begin{bmatrix} x \\ y \end{bmatrix} = \mathbf{H}\mathbf{x} + \mathbf{v} = \begin{bmatrix} 1 & 0 \\ 0 & 1 \end{bmatrix} \begin{bmatrix} x \\ y \end{bmatrix} + \begin{bmatrix} v_x \\ v_y \end{bmatrix}. \tag{5.13}$$

where σ_{v_x} and σ_{v_y} are both 0.5 m.

For simplicity and clarity, we assume that the vehicle is heading north (truth) with a constant speed of 108 km/hr (30 m/sec). This is the speed of typical highway driving in the United States. The navigator initial heading error is 5.73^o (0.1 rad) East of North. The initial position coordinates are at $(0,0)$. Monte Carlo simulation is performed by drawing 10^6 samples to establish benchmark error distributions. The EKF approximated error distributions are constructed using the mean and covariance solution from the EKF filter. The over-bounding EKF error distributions are constructed

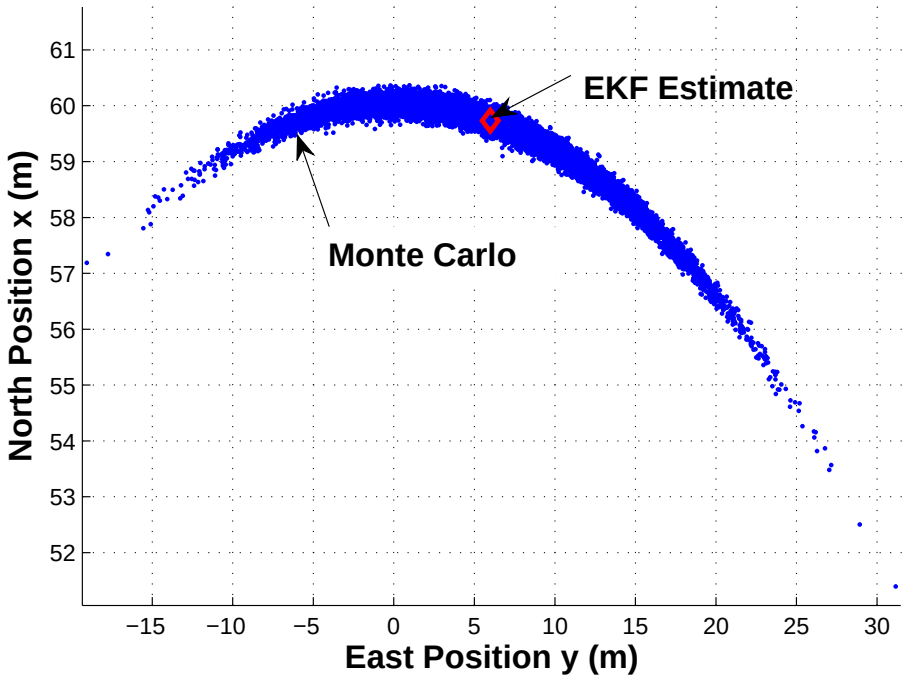

Figure 5.10: True and EKF predicted position distributions at $t = 2$ second.

using the mean and covariance solution from the EKF filter where the nonlinear state transformations are over-bounded using the method proposed in Chapter 4. Both the EKF approximated error distributions and over-bounding EKF over-bounding distributions will be compared with the benchmark distributions.

For clarity and simplicity, only the two dimension position error covariances are considered. Thus, while the covariance matrix should be a 3×3 matrix, we will deal with the 2×2 sub-matrix of position covariance.

5.2.1 EKF Time Propagation Over-Bounding

Figure 5.10 shows the Monte Carlo simulated position distributions at $t = 2$ second. The blue points in Figure 5.10 are Monte Carlo propagated positions at $t = 2$ second by drawing 10^6 random samples at $t = 0$ second and then update those samples recursively through Equation 5.12 with a sampling frequency of 10 Hz. The EKF predicted mean is also plotted in Figure 5.10 and the value

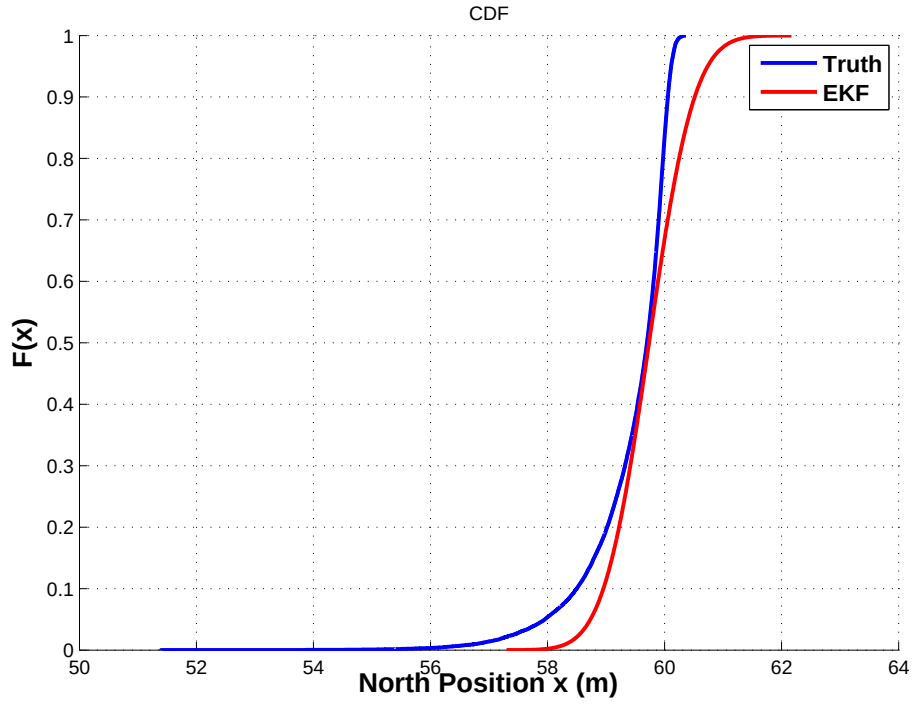

Figure 5.11: True and EKF predicted north position CDF at $t = 2$ second.

is as follows:

$$\hat{\mathbf{x}}^{-} = \begin{bmatrix} 59.73 \\ 5.99 \end{bmatrix} \tag{5.14}$$

where the $'-'$ superscript indicates the time update predicted value before a measurement available (i.e., a priori estimate).

To have a complete EKF approximated error distribution we also need the information of the EKF prediction covariance matrix which is shown as follows:

$$\mathbf{P}^{-}_{EKF} = \begin{bmatrix} 0.37 & -3.58 \\ -3.58 & 35.70 \end{bmatrix} \tag{5.15}$$

To see how well the EKF predicted error probability density function (pdf) behaves compared with the benchmark error pdf, Figure 5.11 shows both the true error pdf and the EKF predicted one for the north position. In Figure 5.11 the blue line is the benchmark truth error distribution and the red line is the EKF predicted error distribution. Figure 5.11 shows this EKF predicted distribution can

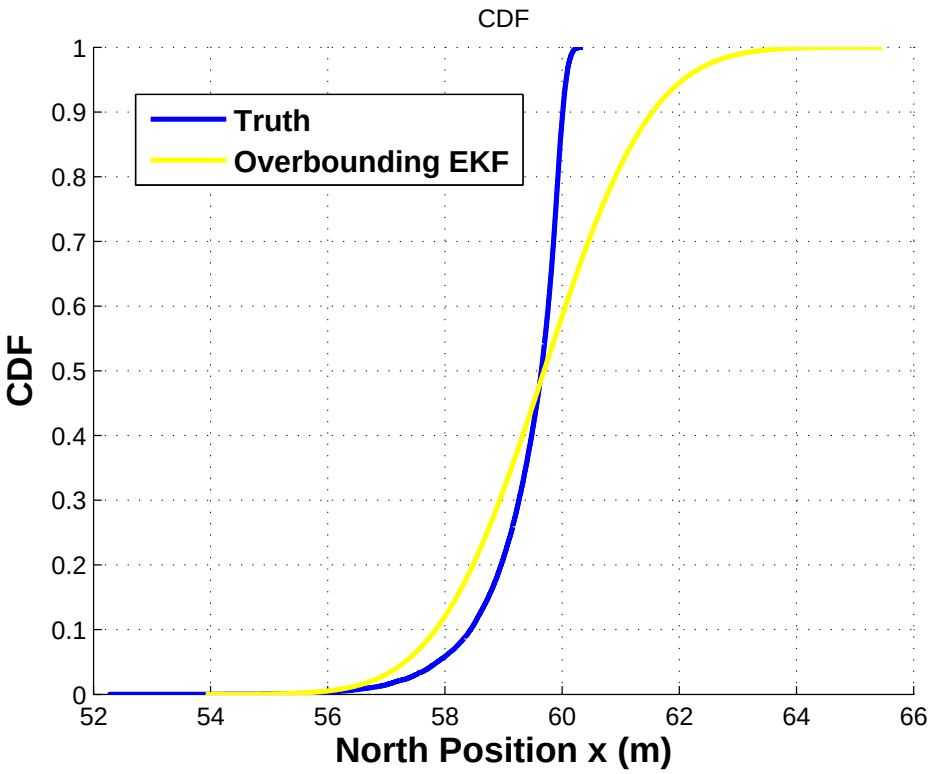

Figure 5.12: True and over-bounded EKF predicted north position CDF at $t = 2$ second.

not over-bound the north position true distribution. The left tail of the true distribution is heavier than the EKF predicted distribution. This is due to the nonlinear coordinates transformations.

We can use the method proposed in Chapter 4 to inflate the state propagate covariance matrix directly to account for nonlinear coordinates transformations. It can be regarded as a more systematic and smarter way to inflate the noise and tune the EKF filter. Figure 5.12 shows that this can over-bound the north position true CDF. The over-bounded EKF predicted covariance matrix is as follows:

$$\tilde{\mathbf{P}}^{-}_{EKF} = \begin{bmatrix} 2.08 & -5.25 \\ -5.25 & 51.32 \end{bmatrix} \tag{5.16}$$

where $\tilde{\mathbf{P}}$ represents the covariance matrix of the over-bounding EKF. It can be seen that both the diagonal elements (variances of north position and east position) and non-diagonal elements (the covariance between north position and east position) have been inflated to account for the non-Gaussian distribution.

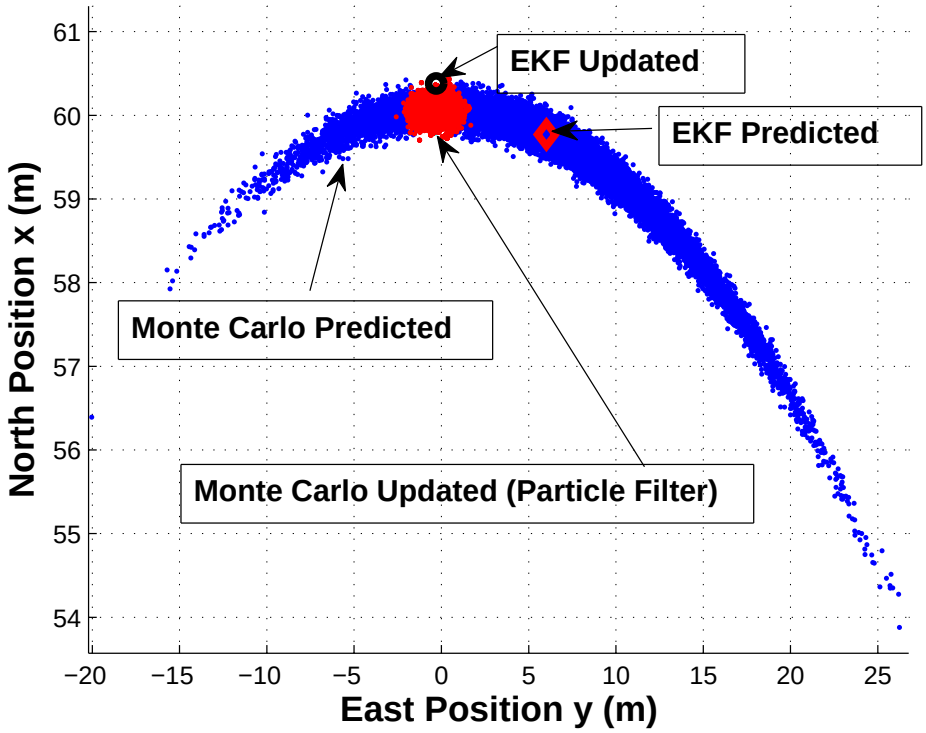

Figure 5.13: True and EKF updated position distributions at $t = 2$ second.

5.2.2 EKF Measurement Update Over-Bounding

Suppose at $t = 2$ seconds we have a measurement z. The Monte Carlo results (Particle Filter) and the EKF results are shown in Figure 5.13. The EKF updated covariance matrix is:

$$\mathbf{P}_{EKF}^{+} = \begin{bmatrix} 0.014 & -0.024 \\ -0.024 & 0.246 \end{bmatrix} \tag{5.17}$$

where the $'+'$ superscript represents the solution after the measurement has been used. The CDF over-bounding is shown in Figure 5.14. The EKF estimate has an obvious bias and the EKF estimated CDF can not over-bound the true CDF. It can be seen that although the EKF has a bias in its estimate it *thinks* its estimated is working quite well compared with the truth. The Over-bounding EKF overcomes this problem by inflating the state error covariance matrix. The CDF over-bounding of the over-bounded EKF is shown in Figure 5.15. The covariance matrix of the over-bounded EKF

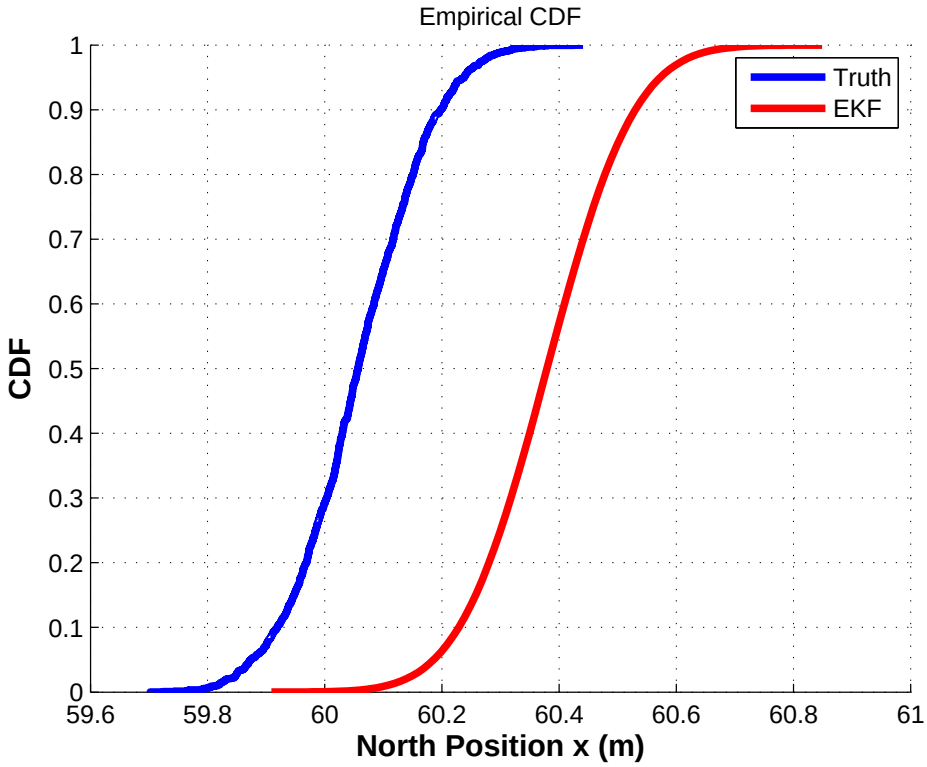

Figure 5.14: True and EKF updated position distributions at $t = 2$ second.

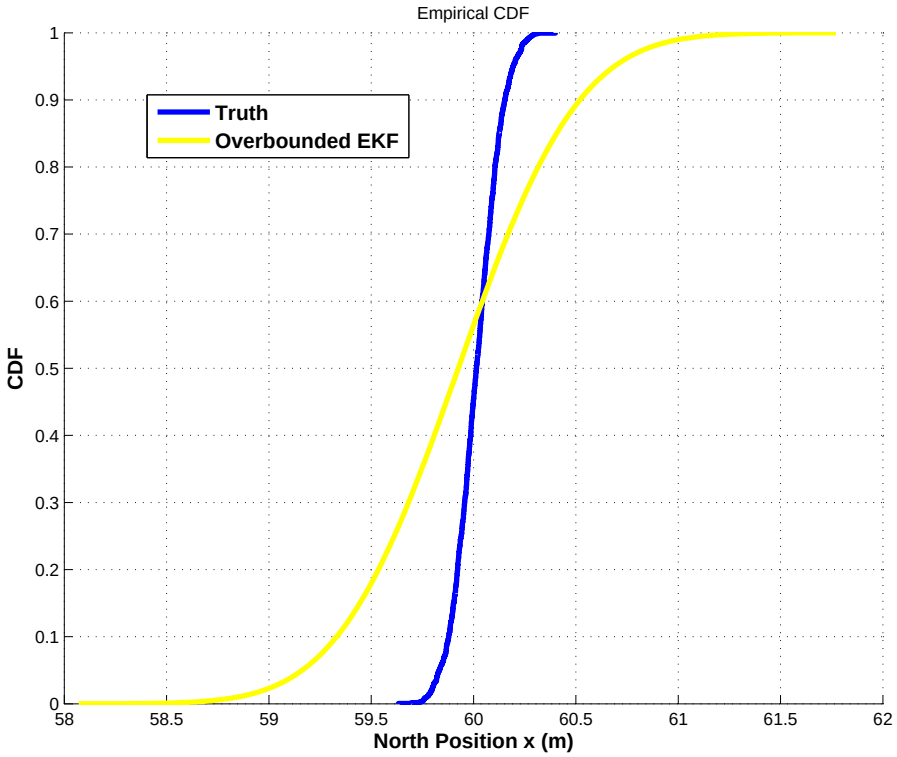

Figure 5.15: True and over-bounded EKF updated position distributions at 2*nd* second.

is as follows:

$$\tilde{\mathbf{P}}^{+}_{EKF} = \begin{bmatrix} 0.215 & -0.0035 \\ -0.0035 & 0.248 \end{bmatrix} \tag{5.18}$$

It can be seen that the north position variance is inflated a lot (from 0.014 to 0.215) to account for the bias.

5.3 Conclusion

Before closing this chapter, it is important to highlight what were the key points the preceding examples where intended to illuminate. The key point can be summarized by the following sentence: For the two-dimensional, integrated INS/GNSS problem which uses an Extended Kalman Filter as the sensor fusion algorithm and coriolis terms are too small so that they can be ignored, over-bounding of output errors can be achieved by simply inflating the EKF estimated covariances. Of

course this assume a special fusion architecture between INS and GNSS. The overbouding works as long as the integration is loose [3] and there is no feedback or estimation of IMU errors . This architecture is what is sometimes called the feed forward formulation of INS/GNSS integration. It is exclusively used when the integration between INS and GNSS is using a high quality (navigation grade or better) INS. Extending this to the case where feedback is present (as would be the case when low quality/cost IMUs are used) is clearly an area that will require further exploration. Another open issue that was dealt with in somewhat of an ad hoc way in this chapter was this: By how much does one have to inflate the covariances to achieve pre-defined levels of integrity? Future work should focus on developing a systematic way for inflating the EKF covariances.

Chapter 6

Conclusion

This thesis has shown how to over-bound and model a time-varying and higher-order underlying process using a lower-order, stationary time-domain model. The model used for over-bounding is a conservative approximation of the actual noise process. For low-cost inertial sensors, this thesis developed and validated unified mathematical models for over-bound the behavior of the post calibration residual errors of inertial sensors. These error models are amenable for use in risk or integrity analysis of vehicle navigation and guidance systems. Two over-bounding methods were proposed: Auto-Correlation Function (ACF) over-bounding and Allan Variance over-bounding. It was found that the white noise model will underestimate the INS error after several seconds and the correlated model should be included. It was also found that the modeling of stochastic process with a very long correlation time (several thousand seconds) is not necessary if INS is depended on solely only for a short time (less than several minutes). So for the applications where INS is depended on solely for several seconds to several minutes (e.g. INS coasting when GPS signals get lost temporarily), it is convenient and conservative to use the proposed unified mathematical models including the white noise model and a simple time domain correlated model to over-bound the true process.

The mathematical models of the INS are a set of nonlinear stochastic differential equations with stochastic inertial sensor measurements as input and stochastic initial conditions. Considering the discretized stochastic difference equations, the nonlinearities of the system come from two parts which need to be handled in the over-bounding: the nonlinear transformation of the sensor errors, and the nonlinear transformation of the previous navigation states. This thesis presented an analysis

of over-bounding of nonlinear transformations of random variables which occur in INS systems. It is shown that the INS system output errors can be over-bounded by Gaussian distributions with an inflated variance from EKF predicted ones. This is an extension of previous over-bounding methods which apply only to linear systems. When applied to INS, it is shown that the velocity channels and position channels solution can be over-bounded by Gaussian distributions.

In INS error over-bounding presented in this thesis, only the marginal distribution of each navigation state (e.g. north velocity or east position) is over-bounded. Whether over-bounding all marginal pdfs can guarantee the over-bounding of whole pdf is still an open question. What is more, since over-bounding the whole pdf other than marginal pdf can pick some favorable directions as principle axis of the over-bounding pdf, it is possible to find a tighter over-bounding distribution. The over-bounding of multi-dimensional pdf is not well defined yet and can be a direction of future research.

Bibliography

[1] "Midg ii specifications," Tech. Rep., 2005.

[2] "Specification sheet for the μnav navigation servo control board,document no. 6020-0083-02, rev. b." Tech. Rep., 2006.

[3] P. D. Groves, *Principles of GNSS, Inertial and Multisensor Integrated Navigation Systems*. Artech House, Boston, MA, 2008.

[4] J. A. Farrell and M. Barth, *The Global Positioning System and Inertial Navigation*. McGraw-Hill, New York, NY, 1999.

[5] A. Gelb, *Applied Optimal Estimation*. The MIT Press,Cambridge, Massachusetts., 1974.

[6] G. Brown and P. Y. C. Hwang, *Introduction to Random Signals and Applied Kalman Filtering, 2^{nd} Edition*. John Wiley, New York, 1992.

[7] B. DeCleene, "Defining pseudorange integrity- overbounding," in *Proceedings of the ION-GPS*, Salt lake City, UT, 2000.

[8] J. Rife, S. Pullen, B. Pervan, and P. Enge, "Paired overbounding and application to gps augmentation," in *Procceedings of the IEEE PLANS 2004*, Monterey, CA, May 2004.

[9] J. Rife, T. Water, and J. Blanch, "Overbounding sbas and gbas error distributions with excess-mass functions," in *Proceedings of the International Symposium on GNSS/GPS*, Sydney, Australia, 2004.

[10] J. H. Rife and D. Gebre-Egziabher, "Symmetric overbounding of correlated errors," *Navigation*, vol. 54, pp. 109–124, 2007.

[11] O. Bilenne, "Integrity-directed sequential state estimation: Assessing high reliability requirements via safe confidence intervals," *Information Fusion*, vol. 8, pp. 40–55, 2007.

[12] P. B. Ober, "Sbas integrity concept: towards sbas validation," European Organisation for the Safety of Air Navigation, Tech. Rep., 2001.

[13] J.Cosmen-Schortmann, M. Azaola-Saenz, M. A. Martinez-Olague, and M. Toledo-Lopez, "Integrity in urban and road environments and its use in liability critical applications," in *IEEE PLANS*, Monteray,CA,USA, 2008.

[14] H. L. Lim, B. Newstrom, C. Shankwitz, and M. Donath, "A conformal augmented heads up display for driving under low visibility conditions," in *Proceedings of the 5th International Symposium on Advanced Vehicle Control*, Ann Arbor, MI, 2000.

[15] L.Alexander, P. M. Cheng, M. Donath, A. Gorjestani, B. Newstrom, C. Shankwitz, and W. T. Jr., "Dgps-based lane assist system for transit buses," in *Proceedings of the 2004 IEEE ITS Conference (ITSC 2004)*, Washington, DC, 2004.

[16] A. Gorjestani, L. Alexander, B. Newstrom, P. Cheng, M. Sergi, C.Shankwitz, and M. Donath, "Driver assistive systems for snowplows," Minnesota Departmetn of Transportation (MnDOT) Report No. 2003-13, Tech. Rep., 2003.

[17] R. E. Weibel and R. J. Hansman, "An integrated approach to evaluating risk mitigation measures for uav operational concepts in the nas," in *AIAAs 4th Infotech@Aerospace Conference*, Arlington, VA, 26 - 29 September 2005.

[18] Z. Xing and D. Gebre-Egziabher, "Modeling and bounding low cost inertial sensor errors," in *Proceedings of IEEE/ION PLANs 2008*, Monterey, CA, May 6 - 8, 2008, pp. 1122–1132.

[19] J. Rife, S. Pullen, B. Pervan, and P. Enge, "Core overbounding and its implications for laas integrity," in *Proceedings of the Institute of Navigation's ION-GNSS*, 2004, pp. 2810–2821.

[20] A. Papoulis and S. U. Pillai, *Probability, Random Variables and Stochastic Processes, 4th Edition*. McGraw-Hill Inc., 2003.

[21] "Draft standard specifications format guide and test procedure for coriolis vibratory gyros," Tech. Rep.

[22] J. A. Rios and E. White, “Low cost solid state gps/ins package,” Tech. Rep.

[23] A. E. Bryson, *Applied Linear Optimal Control: Examples and Algorithms*. Cambridge University Press, 2002.

[24] p. y. p. R. F. Stengel), title=Optimal Control and Estimation.

[25] L. Ljung, *Sytem Identification: Theory for the User*. Prentice Hall, Englewood Cliffs, New Jersey, 1987.

[26] J. N. Juang, *Applied System Identification*. Prentice Hall, Englewood Cliffs, New Jersey, 1994.

[27] D. W. Allan, “Statistics of atomic frequency standards,” in *Proceedings of the IEEE*, vol. 54, no. 2, 1966, pp. 221–230.

[28] M. M. Tehrani, “Ring laser gyro data analysis with cluster sampling technique,” *Proceedings of SPIE*, no. 2, pp. 207–220.

[29] L. C. Ng and D. J. Pines, “Characterization of ring laser gyro performance using the allan-variance method,” *AIAA Journal of Guidance Control and Navigation*, no. 1, pp. 211–213, 1984.

[30] N. El-Sheimy, H. Hou, and X. Niu, “Analysis and modeling of inertial sensors using allan variance,” *IEEE Transactions on Instrumentation and Measurement*, vol. 57, no. 1, 2008.

[31] A. M. Sabatini, “A wavelet-based bootstrap method applied to inertial sensor stochastic error modelling using the allan variance,” *Institute of Physics Publishing, Measurement Science and Technology*, vol. 17, pp. 2980–2988, 2006.

[32] X. N. nad Sameh Nassar and N. El-Sheimy, “An accurate land-vehicle mems imu/gps navigation system using 3d auxilliary velocity updates,” *Navigation*, vol. 54, no. 3, 2007.

[33] H. Kim, J. G. Lee, and C. G. Park, “Performance improment of gps/ins integrated system using allan variance analysis,” in *The 2004 Internation Symposium on GPSS/GPS*.

[34] Y. Yi, “On improving the accuracy and reliability of gps/ins-based direct sensor georeferencing,” Ph.D. dissertation, Ohio State University, 2007.

[35] G. W. Pulford, “A proof of the spherically symmetric overbounding theorem for linear systems,” *Navigation*, vol. 55, no. 4, pp. 283–292, 2008.

[36] J. H. Rife and D. Gebre-Egziabher, “Symmetric overbounding of correlated errors,” in *Proceedings of ION-GNSS 2006, Ft. Worth, TX*, 2006.

[37] D. Bevly, D. Gebre-Egziabher, and B. W. Parkinson, “Parametric error equations for dead reckoning navigators used in ground vehicle guidance and control,” *Navigation*, vol. 53, no. 2, pp. 135–148.

[38] M. Petovello and G. Lachapelle, “Comparison of vector-based software receiver implementations with application to ultra-tight gps/ins integration,” in *Proceedings of the ION-GNSS 2006 Conference*.

[39] G. Gao and G. Lachapelle, “Ins-assisted high sensitivity gps receivers for degraded signal navigation,” in *Proceedings of the ION-GNSS 2006 Conference*.

[40] D. Gebre-Egziabher, R. C. Hayward, and J. D. Powell, “Design of multi-sensor attitude determination systems,” *IEEE Journal of Aerospace Electronic Systems*, vol. 40, no. 2, pp. 627 – 643, 2004.

[41] F. B. Hanson, *Applied Stochastic Processes and Control for Jump-Diffusions*. Society for Industrial and Applied Mathmatics, 2007.

[42] D. Jung and L. E. J., “Design and development of a low-cost test-bed for undergraduate education in uavs,” in *Proceeding of the European Control Conference, Seville,Spain*, December 12-15,2005, pp. 2739–2744.